論文 / 著書情報
Article / Book Information

題目(和文)	
Title(English)	Numerical and Experimental Evaluation of Dynamic PT Tendon Fracture Mechanics
著者(和文)	イオアニス ゴルフィノポロス
Author(English)	Ioannis Gkolfinopoulos
出典(和文)	学位:博士(学術), 学位授与機関:東京工業大学, 報告番号:甲第12599号, 授与年月日:2023年9月22日, 学位の種別:課程博士, 審査員:千々和 伸浩,岩波 光保,佐々木 栄一,河野 進,丸山 泰蔵
Citation(English)	Degree:Doctor (Academic), Conferring organization: Tokyo Institute of Technology, Report number:甲第12599号, Conferred date:2023/9/22, Degree Type:Course doctor, Examiner:,,,,
学位種別(和文)	博士論文
Type(English)	Doctoral Thesis

Numerical and Experimental Evaluation of Dynamic PT Tendon Fracture Mechanics

A thesis submitted in partial fulfilment of the requirements for the degree of Doctor of Philosophy

Ioannis Gkolfinopoulos

Department of Civil Engineering

Tokyo Institute of Technology

Tokyo, Japan

July 2023

Abstract

Prestressed concrete is a versatile construction material that enables the realization of many modern buildings and civil structures by placing the tensile stressed areas of the concrete under compression and is commonly used in structures which require long spans. This compensates for the low tensile strength of concrete through targeted imposed internal stresses, creating internal force variables that counteract external loads and constraint stresses. This work focuses on a particular type of tensioned concrete technique, pre-tensioning, where the prestressing tendons are tensioned prior to casting the concrete and no anchorage device is used, as the prestressing forces are transferred solely through bonding. Pre-tensioning is commonly used in precast elements, including girders, hollow-core planks, crossties, and concrete poles. The combination of pre-tensioning and post-tensioning techniques offer improved structural performance and construction freedom. However, despite its long history, describing the transfer of prestressing force, dimensioning the anchorage zone, and quality monitoring remains challenging. Moreover, failure mechanisms of pre-tensioned concrete members can be complex, and apart from typical RC member failure such as flexural or shear, pretensioned member failure can also include Bond Failure: in which if the adhesion between tendon and concrete is inadequate a decrease in load-carrying capacity along with loss of prestressing can occur. Additionally, Splitting Failure can occur if excessive pre-stressing is applied or poor detailing techniques are applied during construction which limit the load bearing capacity of surrounding concrete and can cause cracking along the length of the pre-tensioned member. This work aims to address these challenges by summarizing the current state of pre-tensioning and post-tensioning anchorage, presenting experimental and numerical investigations into individual material parameters and overall bond performance.

Initially, an extensive literature review is performed to identify the basic characteristics surrounding bond behavior of smooth plain bars and ribbed bars or strands in concrete or concrete-like materials such as grouting mortar. The bond between reinforcing bars and concrete in reinforced concrete structures consists of adhesion, friction, and mechanical anchorage. Adhesion occurs due to concrete hardening and depends on the surface conditions of the steel and properties of the cement paste, but it has minor importance as it fails at small displacements. Friction is based on forces in the contact zone, induced by external loads and

concrete characteristics, and it provides additional bond. Mechanical anchorage, dominant in ribbed bars or strands, involves the interlock between steel ribs and surrounding concrete, restricting relative displacement. The degree of mechanical anchorage depends on the deformation behavior and shear capacity of the bonding joint. In pre-tensioning, adhesion, friction, and the Poisson effect play crucial roles in transferring prestress, while the flexural bond length experiences reduced lateral pressure. Design models like Eurocode 2 and Model Code 2010, ACI, AASHTO, Japan road association provide formulas to calculate bond stress, transmission length, and flexural bond length based on concrete and tendon properties.

In the next step, material properties for prestressing tendons commonly used in Japanese infrastructure were obtained through extensive experimental program. Johnson-Cook (JC) constitutive model parameters were proposed to be used in commercial FEA software and good accuracy was achieved when replicating the experimental program in numerical simulations. The JC damage model was rigorously tested by replicating the experimental tests and considering various factors such as stress-strain data and its accuracy was confirmed through Digital Image Correlation (DIC) analysis. The model demonstrated superior performance in predicting the experimental data with minimal effort compared to other analytical models. However, accurate calibration of model parameters requires extensive numerical data from multiple experimental cases. Although there were minor discrepancies between the FE simulation and experimental results, the model accurately predicted the effects of strain concentration and geometrical deformation, including necking. Based on the research findings, the proposed procedure can be applied to accurately predict the fracture behavior of the tested material for analyzing post-tensioned concrete members.

Finally, an experimental investigation was conducted to analyze the bond performance and degradation of plain smooth bars embedded in normal and ultra-high strength grouting mortar. The experiments involved static pullout rates, as well as dynamic rates. The aim was to determine material parameters for use in FE modeling and propose an analytical bond constitutive model. The proposed model demonstrated good agreement with experimental results and was further verified using material data from other researchers, showing its applicability for different material strengths, smooth bar diameters, and pullout rates. Successful replication of experimental results in FEM simulations required accurate definition of material parameters and interaction parameters between the grouting mortar and smooth bar.

The proposed model accurately simulated bond degradation, as well as the effects of bar deformation and their impact on frictional stress and strain distribution at various pullout stages.

By utilizing the findings of this research, researchers can simulate the development and degradation of bond in brittle materials like concrete or grouting mortar when interacting with stiffer materials such as steel. This can be achieved by considering fundamental material parameters like cohesion, friction, confinement stress, and debonding rates, without the need for extensive experimental procedures.

Acknowledgements

I would like to express my deepest gratitude to my research advisor, Associate Professor Nobuhiro Chijiwa for giving me the opportunity to joining his laboratory in Tokyo Institute of Technology and for his constant support and guidance towards the completion of my graduate study.

I would like to express my gratitude towards Professor Iwanami Mitsuyasu and Assistant professor Nakayama Kazuhide for their insight, feedback, supplementary guidance and assistance with life and university matters. I would like to also express my gratitude towards our laboratory secretary, Hayashi Yoko for her continuous support regarding financial and organizational matters in the joined laboratory environment.

I also like to express my indebt to Ministry of Education, Culture, Sports, Science, and Technology (MEXT), Japan for granting me Monbukagakusho scholarship. The financial support given to me made the completion of this study possible, especially during difficult times like this with the COVID-19 pandemic still being prevalent and affecting our daily lives to an unimaginable degree.

I am thankful to all the laboratory colleagues, present and former, whom during my study period have given me companionship, insight, and guidance which lead to the completion of this work. A special acknowledgement to Jinsei, Kuwatsuru, Hikaru and Yoshii who also given me friendship and moral support, along with their technical support and sharing knowledge.

This thesis is dedicated to my parents, Athanasia and Christos Gkolfinopoulos, my Brother Alkis who I really respect and deeply love. Without them I would not be what I am today and would not be able to fulfill this degree.

Finally, all of my friends back in Greece for their support, wishes and psychological support during this journey, along with a person whom even though I only spent an afternoon with, gave me the insight strength and final push I needed to complete my degree. Without them I would not be able to write this dissertation. Wherever you may be I truly wish for your happiness, overcome your difficulties, and find what they are looking for in this life. Thank you for taking a chance with me.

Table of Contents

List of Figures

List of Tables

List of Symbols

Chapter 2

α_1	Coefficient that considers the type of release (sudden or gradual)
α_2	Coefficient that is based on the type of tendon (strand or wire)
a_{ct}	Coefficient that includes the long-term effects on the concrete tensile strength and unfavorable effects resulting from the way the load is applied
A_p	cross-sectional area of the tendon
a_{p1}	Coefficient that considers the type of release (sudden or gradual release)
a_{p2}	Coefficient that considers the action effect to be verified (anchorage length or transverse stress)
a_{p3}	Coefficient that considers the influence of the bond situation (strand and indented or crimped wires)
b_{cct}	Coefficient that depends on the age of the concrete
f_{bpt}	Constant bond stress in the transmission length
$f_{ctb}(t)$	design value for the concrete tensile strength at the time of release
f_{ctm}	Tensile strength of concrete (mean value)
f_{pd}	Design strength of tendon
γ_c	Partial safety factor for concrete
η_1	Value that it is based on the bond conditions
$\eta_{\rho 1}$	Coefficient that considers the type of tendon and the bond situation at release
$\eta_{\varrho 2}$	Coefficient that considers the type of tendon and the bond condition at the anchorage
l_{pbd}	Total anchorage length
l_{pbt}	Anchorage length
l_{ds}	Flexural bond length
l_{pd}	Flexural bond length
l_{pt}	Transmission length
ϕ	Nominal diameter of tendon
σ_{pm0}	Tendon stress just after release of the prestressing
t_m	Mean bond stress

Chapter 3

JC related symbols

A	Yield stress
α	Specimen's minimum cross section radius
B	Strain hardening constant
C	Coefficient of strain rate
D	Damage law
$D_1 - D_5$	Damage parameters
ε_0	Reference strain rate
ε_f	Fracture strain
ε_p	Accumulated plastic strain
ε^*	Strain rate
η^*	Stress triaxiality
m	Thermal softening coefficient
n	Strain hardening coefficient
R	Radius of notch for uniaxial tensile tests
σ	Von mises stress
σ_D	Stress considering damage law
σ_{eq}	Equivalent stress
σ_m	Mean stress
T^*	Homologous temperature
T_m	Melting temperature
T_{ref}	Reference temperature

Chapter 4

a	plain bar to grout cohesive parameters
b	proposed bond model power parameter
C	bond degradation parameter
C^d	dynamic bond degradation parameter
D_f	compressive strength variation
δ_r	interference radius
E_b	young modulus of bar
E_m	young modulus of mortar
F_{ck}	EC2 concrete cylindrical compressive strength
F_{cm}	EC2 concrete compressive strength
F_{cu}	experimentally recorded compressive strength
F_t	experimentally recorded tensile strength
k	degraded bond stiffness
k_0	initial bond stiffness
r	embedded bar diameter
S	slip
S_f	slip at complete bond degradation
S_0	slip at peak bond stress
t_t	residual bond shear stress
t_u	shear bond stress
t_{rd}	dynamic residual stress
ν_b	Poisson ratio bar
ν_m	Poisson ratio mortar

Appendix

β	Material parameter according to the work of Hsu et al., correlated to the shape of the stress-strain diagram of uniaxial concrete compression test softening behavior
D	Diameter of cylindrical specimen for split-tensile experimental procedure
E_{60}	stiffness corresponding to 0.6 f_{cm}
E_{80}	stiffness corresponding to 0.8 f_{cm}
ε_{cm}	strain corresponding to peak uniaxial compressive stress of concrete
ε_f	uniaxial compressive strain of concrete at complete crushing
ε_t	strain corresponding to peak tensile stress
f_{cm}	peak uniaxial compressive stress of concrete
f_{ct}	tensile stress obtained through split-tensile experimental procedure
f_t	peak tensile stress
η	normalized concrete stress during uniaxial compression
L	Length of cylindrical specimen for split-tensile experimental procedure
P	Vertical load applied through the testing machine
σ_c	compressive stress prediction model according to the work of Le Mihn et al.
σ_f	uniaxial compressive stress of concrete at complete crushing
σ_t	tensile stress prediction model
x	normalized concrete strain during uniaxial compression
ζ	numerical fitting parameter according to the work of Le Mihn et al.

Abbreviations

AASHTO	American association of state highway and transportation officials
ACI	American concrete institute
CEN	European committee for standardization
CMOS	complementary metal oxide semiconductor
CZM	cohesive zone modeling
DIC	digital image correlation
EC2	Eurocode 2
FE	finite element
FEM	finite element modeling
FPS	frames per seconds
JC	Johnson Cook
LRFD	load and resistance factor design
MC10	Model code 2010
NS	normal strength
PC	precast concrete
RC	reinforced concrete
RILEM	International Union of Laboratories and Experts in Construction Materials, Systems and Structures
UHS	Ultra−high strength

Chapter 1

Introduction

1.1. Motivation

Prestressed concrete is a versatile construction material without which many modern buildings and civil structures would not be realizable. The basic principle of prestressed concrete is to place the tensile stressed areas of the concrete cross-section under compression and thus compensate for the low tensile strength of the concrete. This is done by targeted impressed internal stresses; the anchor forces and deviation forces of the prestressing process create internal force variables in the system, which counteract external loads and constraint stresses. Instead of increasing the amount of reinforcement, which is customary in reinforced concrete structures, specific stress states are generated to compensate for the frequent moment forces in girders. Essentially, longitudinal compressive stresses, which may have a favorable effect on the construction material concrete, remain.

Depending on the chosen system and method of construction, various methods can be employed to achieve the prestressing and are separated into external prestressing and internal. The prior solution typically consists of post-tensioned and unbonded systems whereas the later solution involved bonded or unbonded post-tensioning and pre-tensioning. The focus of this work is exclusively on the pre-tensioned members. In contrast to post-tensioning, with pre-tensioning, the prestressing tendons are tensioned in a prestressing bed prior to the concrete being cast. After the concrete is cast and hardened, the pre-tensioning is released and transferred from the tendon into the concrete. Here, no anchorage device is used; solely, a bond transfers the prestressing forces. For this reason, the design must consider not only the moment and shear carrying capacity of the pre-tensioned component, but also the bond anchorage must be guaranteed to prevent a premature fracture. To investigate the bond fracture between tendon bars and surrounding mortar, it was deemed necessary to make pretensioning using smooth bars the focus of this research since in case of using deformed tensioning bars of strands, the

effects of mechanical interlocking become dominant and the influence of adhesion and friction at the interface becomes of secondary importance.(Kurihara et al., 2022)

Today, pre-tensioning is a common fabrication technique for precast elements. More than 80% of the global prestressing steel production is used in prefabricated concrete elements. Common applications include girders with spans up to 75 m, hollow-core planks, crossties, and concrete poles made of spun concrete. As the tendons of pre-tensioned concrete elements typically form straight lines between the anchorages, harping points can be used to achieve a more favorable profile of the pre-tensioned tendons. Furthermore, the combination of pre-tensioning and post-tensioning is an interesting application. For instance, pre-tensioned single-span girders can be joined by post-tensioning to a continuous beam, which improves the structural effect. Pre-tensioning anchorage can also be used in innovative applications such as butterfly web structures and concrete anchorages made of ultra-high-performance concrete.

Although pre-tensioning anchorage has been successfully used for over 75 years, it is still not possible to describe the transfer of the prestressing force, the related dimensioning of this zone, and the quality monitoring in a simple and realistic manner. To achieve this goal initially the state of the art on pre-tensioning and post-tensioning anchorage is summarized in Chapter 2. Furthermore, in this work in order to provide a deeper understanding of the mechanics involving transferring of prestressing force extensive experimental and finite element modeling (FEM) scheme is presented in Chapter 3 which was aimed at obtaining material parameters of precast concrete (PC) tendons commonly used in Japanese infrastructure. In Chapter 4 bond performance and degradation was investigated from an experimental and numerical aspect for smooth bars embedded in grouting mortar.

1.2. Thesis scope and objectives

In this research two separate analytical models are proposed:

- The first one is used to evaluate the dynamic fracture mechanics of PC tendons. Parameters for combined Johnson-Cook flow stress-strain and damage model are proposed to be used in both analytical and numerical setting, accounting for dynamic strain rate effects as well as the effect of different triaxialities on stress concentration.

- For the second analytical constitutive bond model, a methodology is proposed for PC-Tendons embedded into concrete-like materials that accounts for dynamic loading rate effects, embedment material strength, bar diameter. The proposed model consists of shear stress-slip prediction for both bond development and degradation.

The finding of this research work are limited to:

- Pretensioned members using tendons grouted along their whole length.
- The PC-tendon must be directly bonded to the surround material without the introduction or additional sheathing or if it introduced then perfect bond between the sheath and surround material is assumed.

1.3. Thesis outline

Chapter 1 presents the main motivation of this study, problem statement and brief introduction of steps taken to approach solving the stated problems along with the objectives and scope of this work.

Chapter 2 outlines the state of the art on pre-tensioning anchorage. Thus, the bond mechanisms for pre-tensioning anchorage are examined, the current design models as well as the most common testing setups are presented, and the compilation of constitutive laws is explained. Additionally, notable experimental effort that was performed in order to investigate the bond in both pretensioned and post-tensioned application in past few decades is presented.

Chapter 3 investigates the calculation of Johnson-Cook model and damage parameters of high-strength steel material through quasistatic and dynamic uniaxial tests. Finite element analysis was used to replicate of the experimental procedure and though dynamic image correlation analysis the numerical results accuracy was verified. In this investigation it was found that JC model can accurately replicate deformation and stress concentration under different strain rate and triaxiality conditions and thus be used for fracture analysis of prestressed concrete members.

Chapter 4 focuses on proposing a bond stress-slip constitutive model for smooth bars embedded in grouting mortar or concrete-like brittle materials based on analytical approach which presents the effects of material cohesion and the influence of relative friction between steel and concrete. The constitutive model also accounts for pullout rate effects, embedded bar size diameter, as well as the influence of lateral pressure. Required material parameters were obtained through extensive experimental work and the accuracy and applicability of the proposed model was confirmed though FEM analysis as well as comparison with other researcher's work available in literature.

Chapter 5 summarized the results from this thesis, conclusions are listed and some recommendations for further studies are shown in this section.

Chapter 2

State of the art

2.1. Bond mechanisms

2.1.1. Bond of reinforcing bars

In reinforced concrete structures, the bonding resistance between steel and concrete comprises three components: adhesion, friction, and mechanical anchorage. These components work together based on loading and surface conditions, either simultaneously or successively. Adhesion and capillary forces occur in the contact zone between concrete and steel, and this bond is formed due to the concrete hardening. The quality of adhesion depends on the surface conditions of the steel and the properties of the hardened cement paste. However, adhesion is of minor importance as it fails even at small relative displacements, and friction comes into effect as an additional bond mechanism.

Friction is based on forces in the contact zone and requires force components acting perpendicularly to the contact surface. External loads, swelling or shrinkage of the concrete induce lateral pressure, and factors such as roughness of the steel surface and the concrete composition determine the amount of friction. Jamming of detached cement grains and irregularities in the steel cross-section can further increase the lateral pressure. Furthermore, it is correlated with the displacement between the concrete and prestressing tendon.

In ribbed bars, mechanical anchorage or shearing bond is the dominant bond mechanism, where the ribs of the steel bars form a mechanical interlock between the steel surface and surrounding concrete, allowing improved anchorage of the bar in the concrete and restricting the relative displacement of the elements. To activate mechanical anchorage, relative displacement between steel and concrete and internal cracking in the concrete are required. The mechanical interlock can occur through special design or natural roughness of the steel surface and forces are transferred from the inclined rib flanks to the surrounding concrete (Figure 1).

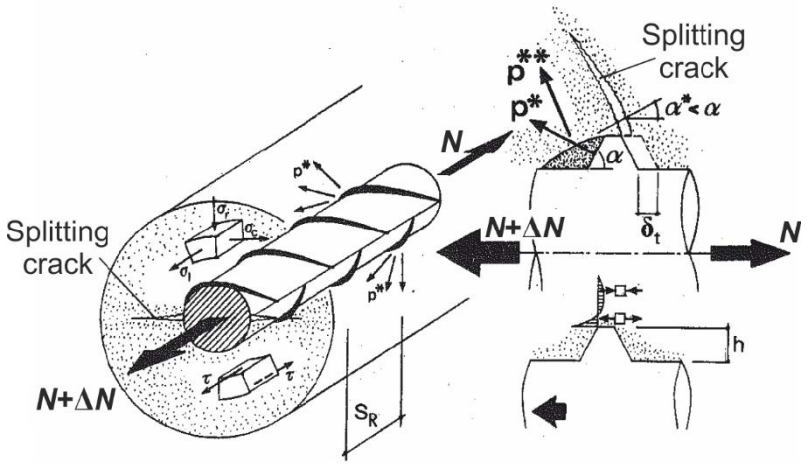

Figure 1 Schematic view of the load transfer via mechanical anchorage

The mechanical anchorage degree is significantly influenced by the deformation behavior and shear capacity of the concrete mortar in the bonding joint. Shearing off the concrete corbels between the ribs requires substantial forces thus the load carrying capacity and failure mode are determined by the stress state that develops in the mortar corbel (Figure 2).

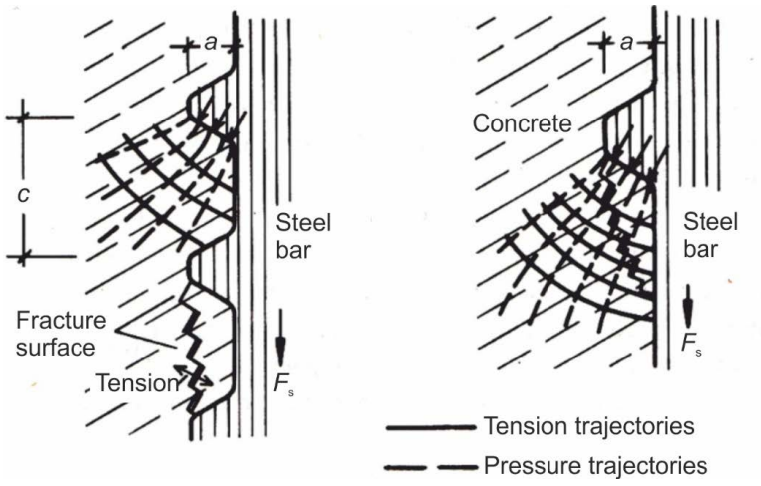

Figure 2 Stress trajectories and fracture path with small (left) and large (right) rib spacing.

High-pressure local stresses load the ribs, creating a circular tensile stress condition in the concrete. If the spatial tensile stresses exceed the tensile strength of the concrete, longitudinal cracks form. The likelihood of longitudinal cracking increases with the bond strength since the forces must be transferred within a shorter transmission length. A minimum concrete cover must be ensured to prevent sudden longitudinal cracks. (Martin & Noakowski, 1981)

2.1.2. Bond in pre-tensioning

When characterizing bond behavior in pre-tensioning anchorage, it's crucial to differentiate between two situations: transferring prestress in the transmission length and anchoring the tendon tensile force due to external loads in the flexural bond length. These two situations can also be referred to as "push-in" and "pull-out" situations, respectively. In the push-in situation, the tendon shortens in the longitudinal direction and expands in the transverse direction due to the release of the prestressing, which occurs in the transmission length. On the other hand, in the pull-out situation, which occurs in the flexural bond length, the tendons are pulled and contracted due to an increasing tendon stress in the bending crack. Additionally, it's important to differentiate between strands and indented wires as bond mechanisms in pre-tensioning (Den Uijl, 1992).

The bonding mechanisms of pre-stressing strands differ from those of conventional ribbed bars that rely mainly on shear forces between the concrete and ribs. In pre-tensioning, adhesion and friction establish the bond for strands. Lateral stresses between the tendon and concrete are required to generate frictional forces. During the "push-in" stage of the transmission zone, the tendon tries to return to its unstressed state when the prestressing is released in the prestressing bed. However, the hardened concrete resists this expansion, resulting in lateral pressure. This phenomenon, commonly known as the Poisson effect or wedge action, governs the strength of the bond for the strands (Figure 3).

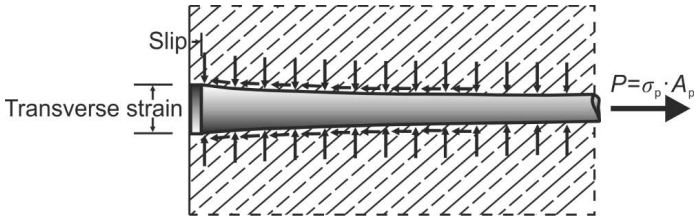

Figure 3 The Poisson effect

The radial stresses also lead to tensile stresses in the surrounding concrete. If these stresses exceed the tensile strength, longitudinal cracks arise in the anchorage zone, and the Poisson effect disappears. For this reason, a sufficient concrete quality and concrete cover must be maintained, and lateral reinforcement may need to be applied accordingly(Ruhnau & Kupfer, 1977).

The model by Nitch (Nitsch & Hegger, 2001) describes the bond forces in transmission length. According to that model the bond strength of tendons in pre-tensioning can be divided into three parts:

- A constant part caused by basic friction, also called the rigid-plastic bond behavior.
- A stress-dependent part, which is based on the Poisson effect and increases with the degree of prestressing.
- A slip-dependent part, which is independent of prestressing. For strands, this effect can be explained by the "lack of fit" resulting from the geometry of the strands, which is not completely uniform. For indented wires, the influence of the mechanical locking by the profiling is crucial.

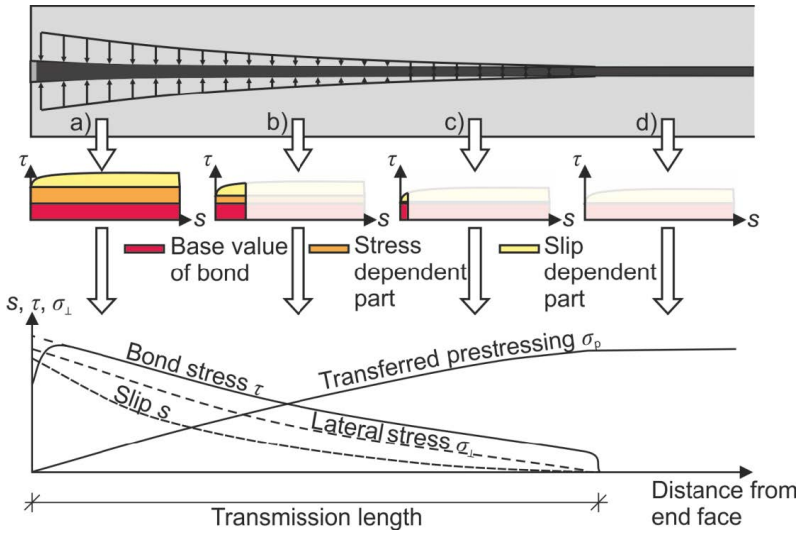

Figure 4 Transfer of prestressing

The aforementioned model explains the transfer of prestress in pre-tensioning, as shown in Figure 4. The figure demonstrates the variations in bond stress, tendon slip, lateral pressure, and transferred prestressing force along the transmission length. As the prestressing force of the tendon decreases, both the lateral pressure and slip decrease along the transmission length, which must be transferred to the concrete. Near the end face of the concrete girder (Figure 4a), the high lateral pressure between the steel and concrete is required to transfer almost the full prestressing force, activating all three bond components. As the transmission length progresses, the prestressing of the concrete increases, and the stress that must be transferred decreases (Figure 4b). At the end of the transmission length (Figure 4c), the bond primarily relies on the base value, and the lateral stresses and slip are small. Beyond the transmission length (Figure 4d), neither bond nor lateral stresses nor slip occur due to prestressing.

The pre-tensioning anchorage requires consideration not only of the bond behavior in the transmission length but also in the flexural bond length, which corresponds to the "pull-out" loading applications. The same bond mechanisms apply in both lengths, but the additional tensile force in the tendon causes a decrease in the cross-sectional area of the prestressing steel. This leads to a reversal of the Poisson effect, reducing the lateral pressure and resulting in a significantly lower bond stress in the flexural bond length.

A qualitative schematic in Figure 5 illustrates the bond stress, tendon slip, and tendon tension that must be transferred throughout the anchoring area, including both the transmission length (l_{pt}) and the flexural bond length ($l_{\Delta\sigma}$) for anchoring the tendon tension at the ultimate limit state. It is unclear whether the bond strength in the flexural bond length is at its maximum adjacent to the crack or if it decreases towards the crack (Figure 5, left). This is because the slip-dependent part of the bond strength increases when the tendon is pulled, while the "negative" Poisson effect causes a significant reduction in the bond strength within the flexural bond length.

The combination of the transmission length and the flexural bond length can compromise the secure anchorage of prestressed tendons in concrete, potentially leading to anchorage failure (Janney, 1954). This can result from an increase in flexural tensile force that must be anchored due to bending cracks being too close to the end of the element, causing a loss of equilibrium between the tendon and concrete forces. Fortunately, in practice, anchorage failure is rare in pre-tensioned components. Bond failure, which usually precedes a flexural failure, tends to be gradual and ductile, but it may also lead to a sudden shear failure. Therefore, careful planning of the anchorage area and including adequate safety margins in the design are crucial.

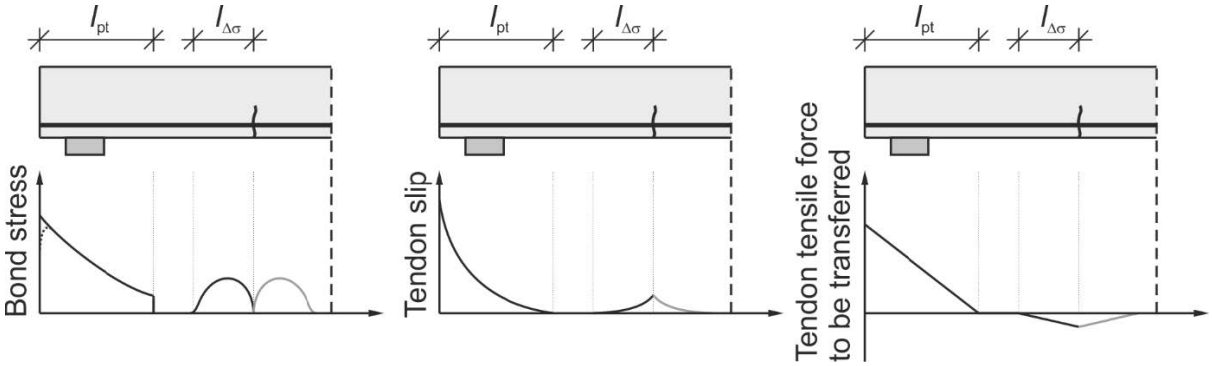

Figure 5 Qualitative progression of bond stress (left), tendon slip (center) and tendon tensile force that is transferred to the anchorage area of pre-tensioned elements (right).

2.2. Engineering design concepts

2.2.1. Eurocode 2

The anchorage length design models currently in use rely on an idealized bilinear relationship between steel stress and distance from the free end of the strand (Figure 6), assuming a constant bond stress in both the transmission length and flexural bond length. While this does not reflect actual bond mechanisms, it has been shown by (Marti-Vargas et al., 2007) that the simplification is acceptable and doesn't deviate significantly from actual measurements.

Design concepts can be divided into two groups: those based on a mechanical model, where the transferable tendon force per prestressing steel surface area is used to calculate force equilibrium for both the transmission length and flexural bond length, and those that rely on empirically determined factors. The former group includes Eurocode 2 (CEN, 2004) (EC2) and Model Code 2010 ("Fib Model Code for Concrete Structures 2010," 2013) (MC10), while the latter includes ACI 318 (American Concrete Institute ACI, n.d.) (ACI), AASHTO (AASHTO, 2015), Japan Road Association (Japan Road Association, 1981) and many models based on them, which are generally non-unit conforming. Design formulas also differ in the factors they consider, for instance, while the influence of concrete strength on bond strength has been affirmed by various test series, ACI 318 and AASHTO do not take it into account.

Eurocode 2 calculates first the constant bond stress f_{bpt} in the transmission length and therefore the design value for the concrete tensile strength $f_{ctb}(t)$ at the time of release must be determined:

$$f_{ctb}(t) = \alpha_{ct} \cdot 0.7 \cdot [\beta_{cc}(t)]^{\alpha} \cdot f_{ctm}/\gamma_c \quad (1)$$

where
- α_{ct} — Coefficient that includes the long-term effects on the concrete tensile strength and unfavorable effects resulting from the way the load is applied
- $[\beta_{cc}(t)]^{\alpha}$ — Coefficient that depends on the age of the concrete
- f_{ctm} — Tensile strength of concrete (mean value)
- γ_c — Partial safety factor for concrete

The constant bond stress (f_{bpt}) for the transmission length is calculated with the design value of the concrete tensile strength $f_{ctb}(t)$ at the time of release:

$$\boldsymbol{f_{bpt} = \eta_{\rho 1} \cdot \eta_1 \cdot f_{ctb}(t)} \quad (2)$$

where
- $\eta_{\rho 1}$ — Coefficient that considers the type of tendon and the bond situation at release

η_1 Value that it is based on the bond conditions

The value of transmission length l_{pt} is given by:

$$\boldsymbol{l_{pt} = \alpha_1 \cdot \alpha_2 \cdot \phi \cdot \sigma_{pm0} / f_{bpt}} \quad (3)$$

where α_1 Coefficient that considers the type of release (sudden or gradual)

α_2 Coefficient that is based on the type of tendon (strand or wire)

ϕ Nominal diameter of tendon

σ_{pm0} Tendon stress just after release of the prestressing

Depending on the design situation (anchorage or transverse stress), the design value of the transmission length should be taken as the less favorable of two values, in order to involve the variations of the bond strength:

l_{pt1} $0.8 \cdot l_{pt}$ (for transverse stress)

l_{pt2} $1.2 \cdot l_{pt}$ (for anchorage) (4)

As long as the anchorage length remains uncracked, and the concrete tensile stress is less than $f_{ctk,0.05}$ no anchorage check in the ultimate limit state is necessary. If the concrete tensile stress exceeds $f_{ctk,0.05}$, flexural cracking occurs. Hence, the additional tendon stress requires a flexural bond length to anchor adequately in the concrete. In this case, the value of the constant bond stress (f_{bpd}) in the flexural bond length, which is assessed to be approximately half of the value in the transmission length, is calculated as follows:

$$\boldsymbol{f_{bpd} = \eta_{\rho 2} \cdot \eta_1 \cdot f_{ctd}} \quad (5)$$

where $\eta_{\rho 2}$ Coefficient that considers the type of tendon and the bond condition at the anchorage

η_1 Value that it is based on the bond conditions

f_{ctd} Design value of concrete tensile strength (Equation 2-1)

The total anchorage length l_{bpd} for anchoring a tendon with stress σ_{pd} is the sum of the transmission length and the flexural bond length. The flexural bond length is determined with the difference between the maximal tendon stress σ_{pd} and the tendon stress after all losses $\sigma_{pm\infty}$. Thus, the anchorage length is:

$$\boldsymbol{l_{bpd} = l_{pt2} + \alpha_2 \cdot \phi \cdot \left(\sigma_{pd} - \sigma_{pm\,\infty}\right)/f_{bpd}} \quad (6)$$

where l_{pt2} Upper design value for the transmission length (Equation 2-4)

α_2 Coefficient that considers the type of tendon (strand or wire)

f_{bpd} Constant bond stress in flexural bond length

2.2.2. Model Code 2010

In *Model Code 2010* (*MC10*), the value of the bond strength for prestressing tendons (f_{bpd}) is determined as in *EC2* by the concrete tensile strength (f_{ctd}). However, *MC10* uses only one term for the bond strength to determine both the transmission length and the flexural bond length. A distinction must be made in both cases only in the concrete tensile strength, which is dependent on the age of concrete:

$$\boldsymbol{f_{bpd} = \eta_{\rho 1} \cdot \eta_{\rho 2} \cdot f_{ctd}} \quad (7)$$

where $\eta_{\rho 1}$ Coefficient that considers the type of prestressing tendon

$\eta_{\rho 2}$ Coefficient that considers the position of the tendon

f_{ctd} Lower design value for the concrete tensile strength

The development of the concrete tensile strength with time is the same as in *EC2*, with the factor $\beta_{cc}(t)$ (Eq. (1)). The main difference between the design concepts of MC10 and EC2 is the basic anchorage length l_{bp} which can be considered as the length required to anchor a non-pre-tensioned tendon. This value is used in MC10 to determine the transmission length and the flexural bond length.

$$\boldsymbol{l_{bp} = \frac{A_p}{\phi \pi} \frac{f_{pd}}{f_{bpd}}} \quad (8)$$

where A_p Cross-sectional area of the tendon

f_{pd} Design strength of the tendon

The transmission length l_{pt} is calculated from the basic anchorage length l_{bp} and the quotient of the steel stress just after release σ_{pm0} and the design tendon strength f_{pd}.

$$\boldsymbol{l_{pt} = \alpha_{p1} \cdot \alpha_{p2} \cdot \alpha_{p3} \cdot \left(\sigma_{pm0}/f_{pd}\right) \cdot l_{bp}} \quad (9)$$

where α_{p1} Coefficient that considers the type of release (sudden or gradual release)

α_{p2} Coefficient that considers the action effect to be verified (anchorage length or transverse stress)

α_{p3}	Coefficient that considers the influence of the bond situation (strand and indented or crimped wires)

The coefficient α_{p2} defines an upper bound and a lower bound value for the transmission length. The ratio of the upper and the lower bound level is 2.0 in MC10, since several investigations indicate values in the range of 1.5-1.9. The parameter $\alpha_{p3} = 0.5$ for strands indicates that the bond strength in the transmission length is twice the value of the basic anchorage length. For indented and crimped wires, the ratio between the bond stresses in the transmission length and the flexural bond length is smaller ($\alpha_{p3} = 0.7$) because it is assumed that the ratio for strands is higher as they are smoother. As in *EC2* the design anchorage length in *MC10* is calculated by adding the flexural bond length (resulting from the additional tendon stress due to external loading) to the transmission length. Therefore, a ratio value for Equation 8 is calculated:

2.2.3. ACI 318

The ACI 318 (ACI) utilizes a bilinear bond stress curve for the anchorage design of prestressing tendons. In comparison to MC10 and EC2, ACI has a simpler design process. The equations below are adjusted to metric units. The original equations are noted in curly brackets. The transmission length is calculated directly from the strand diameter ϕ and the tendon stress $\sigma_{pm}\infty$, without taking into account either the bond stress or the concrete strength. The tendon stress used is the stress immediately after the release of prestressing, subtracted by all stress losses. However, some experts argue that the use of the tendon stress immediately after release σ_{mp0} is more suitable since the transmission length is established at the release of prestress.(Mitchell et al., 1993; Shahawy et al., 1992; Zia & Mostafa, 1977)

$$\boldsymbol{l_{pt} = \frac{\sigma_{pm}\infty}{21}\phi \; ; \; l_{pt} = 50 \cdot \phi} \tag{10}$$

The flexural bond length is calculated with the product of the additional tendon force and the strands diameter. Thus, the formula for the anchorage length becomes:

$$\boldsymbol{l_{pd} = l_{pt}\frac{1}{6.9} \cdot (\sigma_{pd} - \sigma_{pm}\infty) \cdot \phi} \tag{11}$$

It becomes apparent that the bond strength in ACI is three times higher in the transmission length than in the flexural bond length. The formula for the anchorage length of strands has

been used in ACI since 1963. It is based on the results of Hanson and Kaar et al.(Hanson & Kaar, 1959). Regulations for the tendon spacing are also provided by ACI.

2.2.4. AASHTO

In the AASHTO LRFD bridge design specifications the formula for the transmission length depends only on the strand's diameter:

$$\boldsymbol{l_{pt} = 60 \cdot \phi} \tag{12}$$

The formula for the anchorage length is:

$$\boldsymbol{l_{bpd} = 0.145 \cdot k \cdot \left(\sigma_{pd} - \frac{2}{3}\sigma_{pm\infty}\right) \cdot \phi} \tag{13}$$

Where k is a factor used to incorporate the depth of pre-tensioned members.

Although AASHTO also uses a bilinear model to describe the anchorage length, the formula does not allow a comparison of the bond stresses of transmission length and flexural bond length. The formulas of AASHTO have the same origin as the formulas of ACI. The modification with factor κ is based on the results of Buckner and Lane et al.(Buckner, 1995; Lane & Rekenthaler, 1998). ASHTO also regulates the minimum spacing of prestressing tendons.

2.2.5. Japan road association: Specifications for highway bridges

In the case of pretensioned members, prestressing steel is bonded with the concrete through an anchor-type action. Although specific requirements or equations are not given to calculate the anchorage length it is taken for $\phi \leq 15.2mm$ as:

$$\boldsymbol{l_{pt} = 65 \cdot \phi} \tag{14}$$

2.2.6. Pullout setup for pre-tensioning anchorage investigation

In Chapter 4 of this work an experimental pullout procedure is used to obtain shear bond-stress slip curves between grouting mortar and smooth bars. The procedure followed a modified version of the RILEM pullout test RC6 (Logan, 1997). Modification details and experimental investigation details are presented in Chapter 4. According to the original specifications the

specimen of the pull-out test is a concrete cube with feed size of ten times the reinforcing rod diameter ($15 - 20\phi$) or minimal size of 200 mm. The reinforcing bar is positioned in the center of the specimen. To ensure a defined bonded length of 5ϕ, the bond between the reinforcing bar and the concrete is interrupted on one side of the specimen by a plastic pipe (Figure 6). In some cases, shorter bond lengths are also used. The reason for the short embedment length is the nonuniform distribution of the bond stresses along the embedment length, which increases with the bonded length. Hence, the embedment length shall be as short as possible to obtain the presumed constant bond stress-slip relation.

The pullout tests is performed in a stress-controlled manner and maintains a constant loading rate. During the testing procedure the pull-out force and the slip of the reinforcing bar are measured continuously. For the analysis of the tests, bond stress-slip diagrams are plotted. Therefore, the mean bond stress τ_m is calculated as follows:

$$\boldsymbol{\tau_m = \frac{P_b}{\pi \cdot \phi \cdot l_b}} \tag{15}$$

where P_b Pull-out force
l_b Bond length
ϕ Nominal reinforcing bar diameter

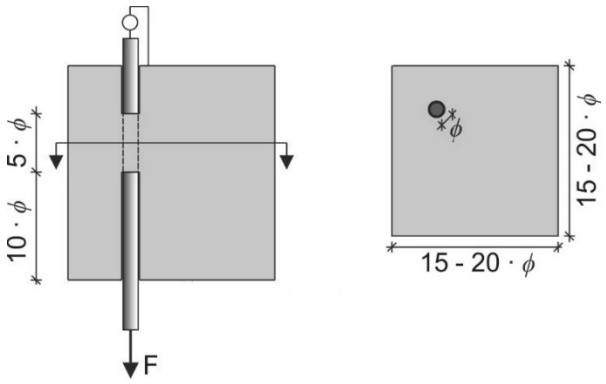

Figure 6 RILEM pullout experiment arrangement

Chapter 3

Determination of Johnson-Cook Material and Failure Model Constants for Tendon Steel

3.1. Theoretical and experimental background of high strength steel tendons

A thorough understanding of the damage and deformation caused in high-strength steel tendons is crucial for accurately assessing the condition of tensioned concrete members. It is essential for the tendons to remain elastic or well within their serviceability limits during regular operation. However, there have been reports of damage to tensioned members of bridge girders due to corrosion, as documented by several researchers (Abdelatif et al., 2013; Coronelli et al., 2009; Jeon & Shim, 2020; Pape & Melcher, 2013; Tamakoshi et al., 2012; Trejo et al., 2009). Unfortunately, the potential failure of tendons caused by corrosion is not adequately addressed in typical design practices for prestressed members, and this oversight can lead to bridge collapses, considering that such members are commonly used in bridges. Presently, manual inspections are necessary to identify corrosion along the length of tendons. Corrosion of tendons in these applications generally occurs due to two main reasons. Firstly, cracks can form in the surrounding concrete or due to exposure to chloride-contaminated water. Secondly, tendon rupture can occur at inadequately grouted positions in the sheathing due to water ingress from anchoring points. Once corrosion has taken place in a tendon, it can result in a significant reduction in the cross-sectional area of the member (Jeon et al., 2020), leading to unfavorable stress concentration conditions. Moreover, in cases of severe corrosion, the remaining cross-sectional area may be insufficient to bear the service loads, such as dead loads, potentially causing yielding or fracture (Figure 7). In the latter scenario, depending on the condition of the surrounding tendons, complete failure could occur if the capacity of the remaining tendons is exceeded during fracture and dynamic loading. Consequently, it is crucial to investigate the fracture performance of high-strength tendons under high strain rates and stress concentration conditions to accurately assess the remaining capacity of a tensioned member.

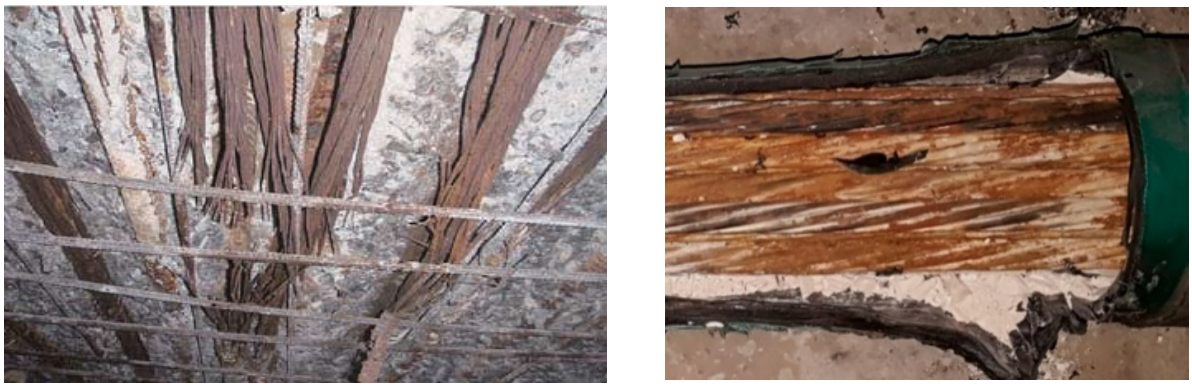

(a) (b)

Figure 7. Deteriorated strands in bridges due to corrosion (a) complete failure(Tamakoshi et al., 2012)]; (b) severe deterioration (Jeon et al., 2020).

Once the state of corrosion in a tensioned member is verified, risk assessment analysis can be performed and thus the remaining capacity can be simulated with the aid of finite element (FE) tools. One of the most common tools used by researchers (Banerjee et al., 2015; Khataei et al., 2010; Murugesan & Jung, 2019; Wuertemberger & Palazotto, 2016) to evaluate the performance and characteristics of metals under coupled stress and high strain-rate conditions is the Johnson-Cook (JC) material and damage model and it is currently one of the most widely incorporated models in commercial FE software packages due to its ability to predict material behavior with accuracy, speed and couples a flow stress model with strain rates, elevated temperatures as well as stress concentration conditions.

In an attempt to propose a modification to the conventional Johnson-Cook (JC) constitutive model, a group of researchers led by K. Xu (K. Xu et al., 2003) conducted an experimental investigation on seven high-strength steels. The steel materials used in their study were BH300, HSLA350, 440W, HSS590, TRIP590, DP600, and DP800. Uniaxial tensile tests were performed on these materials, with strain rates varying from $0.005s^{-1}$ to $1000s^{-1}$. The tests were conducted at normal environmental temperatures, as the research primarily focused on material softening related to heat was not the main objective. The obtained results were utilized to calibrate the material parameters of both the traditional JC constitutive model and the proposed modification. Additionally, experimental data was employed to evaluate the differences between the proposed model, the traditional JC model, and the actual experimental results. The research findings indicated that within the strain ranges of 2% to 15% and tensile strengths of 450MPa to 850MPa, the proposed model exhibited an average error of 2%, which is considered acceptable.

K. Vedantam et al. (Vedantam et al., 2006) investigated the mechanical response of two types of steel, Mild and DP590 in tension at room temperature using quasi-static and split Hopkinson bar techniques at strain rates ranging from $0.001s^{-1}$ to $1800s^{-1}$, and the resulting data were used to calculate JC model parameters. It was found that for increasing strain rates, fracture strain as well as ultimate stress values increased in a similar manner approaching ultimate stress values of 1000MPa. Finally, JC detailed material parameters were presented.

The literature investigation conducted in this study clearly highlights the necessity for accurate modeling of fracture behavior in high-strength steels, which requires proper material characterization and model calibration. Obtaining the required data for finite element (FE) modeling is a costly and time-consuming process, involving experimental efforts under both high strain rates and stress concentration conditions to account for damage initiation and progression parameters accurately. For the commonly used high tensile strength tendon materials found in Japanese infrastructure, readily available model constants are lacking. Therefore, this work focuses on studying the overall behavior, including plastic deformation and fracture characteristics, of medium-carbon high strength steel used in tensioned members. Extensive experimental analysis is conducted under quasi-static and medium strain-rate loading conditions, with specific attention given to stress concentration through the use of tensile testing on notched specimens. By analyzing the experimental data, failure parameters and material constants for the Johnson-Cook (JC) model at room temperature are calculated. Additionally, damage growth parameters are introduced and proposed to accurately model necking and fracture of tensile specimens subjected to uniaxial loading conditions. The identified constants are evaluated through numerical modeling of dog-bone type tensile specimens under similar strain rates as the experimental setup. The strain propagation during various strain-rate and stress concentration conditions is verified using digital image correlation (DIC). Overall, this study aims to bridge the gap in available model constants and provide a comprehensive understanding of the mechanical behavior of medium-carbon high strength steel, considering plastic deformation, fracture characteristics, and stress concentration effects under different loading conditions.

3.2. Tensile testing materials and experimental procedure

In this research the SBPR 930/1080 Type B No. 1 medium carbon high strength steel was investigated, and its chemical composition is presented in Table 1 (in wt %). The material used for the manufacturing of the specimens was supplied by a local company according to JIS G 3109, in 450mm x 32mm cylindrical pieces out of which the dog-bone type specimens were manufactured using a manual lathe. Geometrical details can be seen in Figure 8, for cylindrical specimens used throughout this research for both quasi-static and dynamic tensile tests with smooth as well as rounded notched gauge lengths. The round notch is characterized by its circular shape which is formed as a rounded concave depression onto the otherwise uniform cylindrical shape of the gauge length. For the tensile tests MTS 244.11 servo-hydraulic actuator (Figure 9) was used. Acceleration, velocity, displacement, and excitation frequency characteristics are represented in Figure 10. Despite the dynamic characteristics of the experimental procedure, experimental parameters were well within the capability envelope of the utilized actuator. The actuator was mounted on a loading frame using ball-joints for both fixed and extendable part of the piston to allow for increased mobility and flexibility under various testing conditions and requirements. For this research, both specimens and actuator were positioned and fixed in a vertical orientation to ensure an inline application of pulling force (Figure 11).

Table 1 Chemical composition of SBPR 930/1080 Type B No 1 medium carbon steel (in wt%).

C	Si	Mn	P	S	Cu
0.60~0.65	0.12~0.32	0.30~0.60	≤ 0.030	≤ 0.035	≤ 0.30

Furthermore, to ensure constant pulling rate, the loading end of the specimens were constructed in such a way as to allow for initial retraction of the actuator's piston without exerting force onto the specimen. Once the required velocity is achieved, and after that stage, contact between the top of the specimen and the mounting fixture (plate) at the movable end of the actuator is initiated transferring the resulting load onto the specimen body. As can be seen in Table 2, for dynamic loading cases three specimens were tested for each required strain rate and the resulting force-displacement data were converted into true stress-strain data using standard equations for uniaxial tensile tests. To further aid the calibration of the initial part of

flow stress-strain curves, 2mm strain gauges were attached using adhesive onto the specimens and strain data were captured for values up to 20000μm before the adhesive failure resulting in detachment of the strain gauges positioned in the middle of the respective gauge lengths.

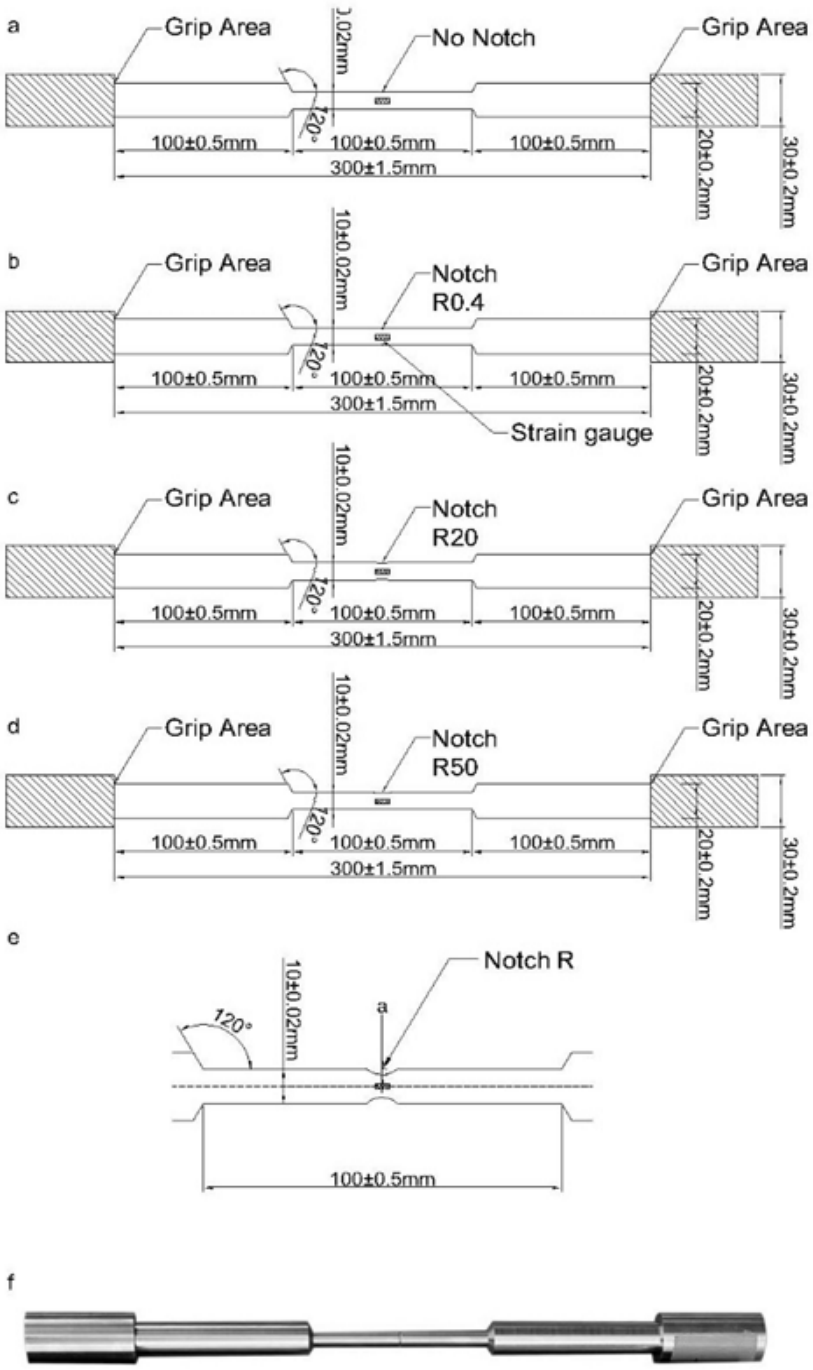

Figure 8 Geometrical details of specimens for tensile tests at (a) smooth-type quasi-static and dynamic strain rates, (b) notched R0.4 type (c) notched R20 type, (d) notched R50 type and (e) detailed representation of notched region (f) typical manufactured specimen.

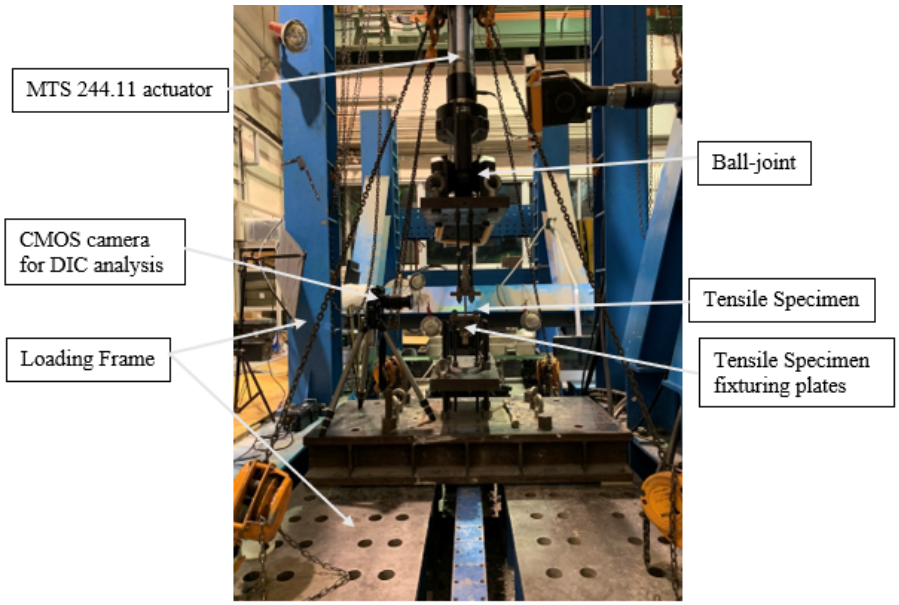

Figure 9 Experimental setup.

Table 2 Manufactured specimen specifications and testing parameters(C - static, D - dynamic _strain rate_notch radius.

Specimen nomenclature	Testing speed (mm/s)	Strain rate during tensile test (s^{-1})	Specimen type	Radius R (mm)	Minimum radius a (mm)	η^*
C1_0.001_NR	0.1	0.001	Smooth	-	-	0.333
C2_0.001_NR	0.1	0.001	Smooth	-	-	0.333
C3_0.001_NR	0.1	0.001	Smooth	-	-	0.033
D1_0.5NR	50	0.5	Smooth	-	-	0.333
D2_0.5NR	50	0.5	Smooth	-	-	0.333
D3_0.5NR	50	0.5	Smooth	-	-	0.033
D1_1NR	100	1	Smooth	-	-	0.333
D2_1NR	100	1	Smooth	-	-	0.333
D3_1NR	100	1	Smooth	-	-	0.033
D1_2NR	200	2	Smooth	-	-	0.333
D2_2NR	200	2	Smooth	-	-	0.333
D3_2NR	200	2	Smooth	-	-	0.033
C4_0.001R20	0.1	0.001	Notched	20	4.5	0.484
C5_0.001R20	0.1	0.001	Notched	20	4.48	0.484
C6_0.001R50	0.1	0.001	Notched	50	4.5	0.395
C7_0.001R50	0.1	0.001	Notched	50	4.48	0.394
C8_0.001R0.4	0.1	0.001	Notched	0.4	4	2.867
C9_0.001R0.4	0.1	0.001	Notched	0.4	3.98	2.961

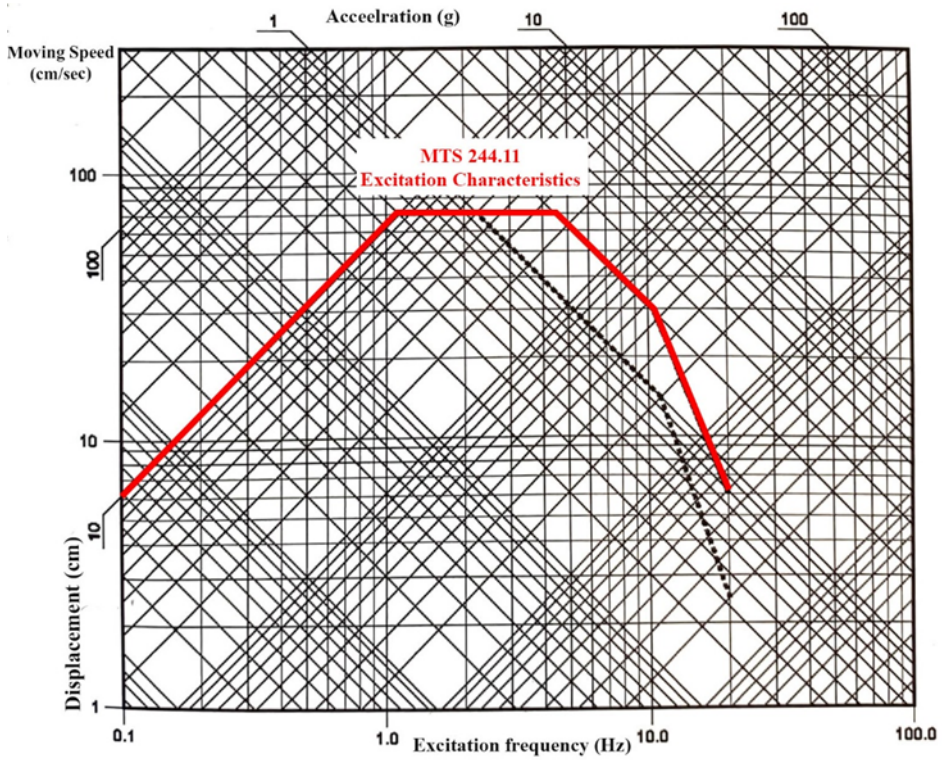

Figure 10 Servo-hydraulic MTS 244.11 technical specifications.

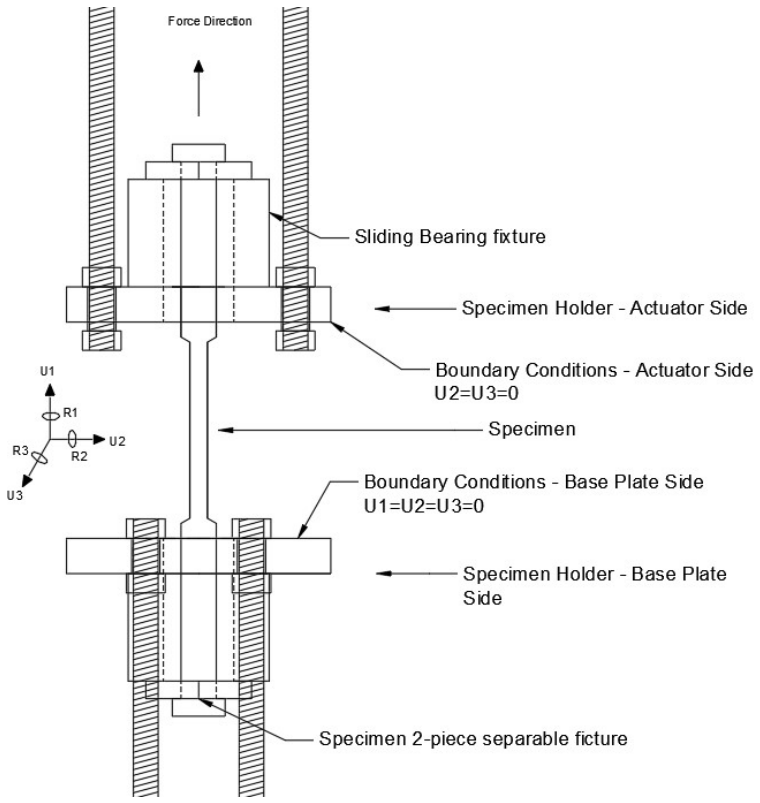

Figure 11 Detailed specimen fixture mechanism.

The flow stress-strain data obtained from smooth specimens (without notches) (Figure 12a) reveals some interesting trends. It can be observed that for the same strain rate, similar stress-strain curves are obtained. At a quasi-static strain rate of $0.001s^{-1}$, the material exhibits the most ductile behavior, with an average fracture strain of 0.127. However, at a strain rate of $0.5s^{-1}$, the material demonstrates a more brittle behavior, fracturing at an average strain of 0.092. On the other hand, specimens tested at a strain rate of $1s^{-1}$ exhibit increased ductility, with an average fracture strain of 0.099, along with the highest ultimate stress values overall. In contrast, specimens subjected to a strain rate of $2s^{-1}$ display the most brittle behavior among all the cases, without showing any significant increase in ultimate stress compared to the slowest dynamic case. Figure 13 presents the engineering stress-strain and converted true stress-strain data for quasi-static testing of notched specimens listed in Table 2. Similar to the variation in strain rate data, good agreement is observed between similar cases when changing the notch size and radius. Smooth specimens demonstrate the highest ductility, and as the minimum specimen radius and notch radius decrease, there is a progressive reduction in both ultimate stress and failure strain. Notably, the C7_0.001R0.4 and C8_0.001R0.4 cases exhibit a significant reduction in both ultimate stress and failure strain, indicating a considerably brittle fracture behavior compared to the smooth specimens.

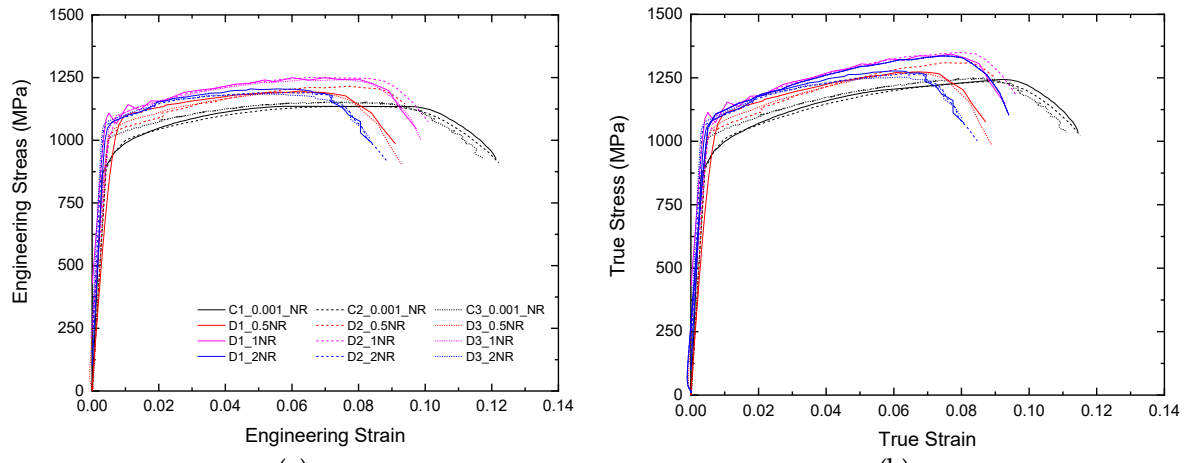

(a) (b)

Figure 12 Engineering stress-strain (a) and true stress-strain (b) curves for uniaxial tensile tests under different strain rates.

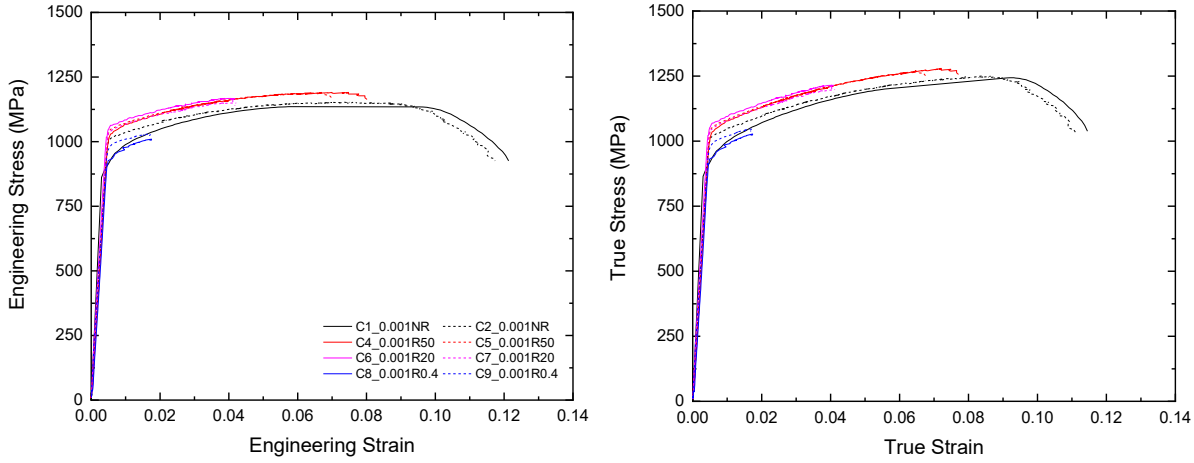

(a) (b)

Figure 13 Engineering stress-strain (a) and true stress strain (b) curves for uniaxial tests with different notch sizes.

3.3. Johnson-Cook Model

In literature applicability and accuracy of Johnson-Cook (JC) model in analyzing and predicting stress-strain behavior, particularly for ductile materials such as steel or aluminum alloys has been extensively researched. These investigations have focused on various scenarios involving large deformations, high strain rates, and elevated temperatures, with specific emphasis on metal forming or impact performance (Akbari et al., 2015; He et al., 2013; Maheshwari, 2013; Samantaray et al., 2009). The JC stress model, represented by Eq. (16), has been widely utilized in these studies.

$$\sigma = \left(A + B\varepsilon^{n}\right)\left(1 + C\ln\dot{\varepsilon}^{*}\right)\left(1 - T^{*^{m}}\right) \tag{16}$$

in which σ represents vonMises or equivalent stress, A yield stress of tested material under reference conditions (strain rate – temperature), B strain hardening constant, n strain hardening coefficient, C is a coefficient of strain rate resulting in post-yield strengthening of the material $\dot{\varepsilon}^{*}$ is the dimensionless strain rate and T^{*} homologous temperature, m is a thermal softening coefficient. It can be observed that the JC model can be separated into three factors based on static stress condition, influence of strain rate and finally influence of temperature when looking at the three parentheses from left to right. In Eq. (16), the $\dot{\varepsilon}^{*}$ parameter as well as T^{*} can be defined in Eq. (17).

$$\dot{\varepsilon}^* = \frac{\dot{\varepsilon}_p}{\dot{\varepsilon}_0} \quad \text{(a)} \qquad T^* = \frac{T - T_{ref}}{T_m - T_{ref}} \quad \text{(b)} \tag{17}$$

$\dot{\varepsilon}_p$ is the accumulated plastic strain and $\dot{\varepsilon}_0$ is the reference strain rate which in this work was taken as $0.001 s^{-1}$. T_m is defined as the melting temperature of the material and T_{ref} reference temperature. For the scope of this research, performance of the high strength medium carbon steel material was investigated under quasi-static and medium dynamic strain rates as well as varying stress concentration conditions, but the temperature factor was not considered since the primary failure factor of tensioned members is usually due to corrosion as mentioned in previous sections.

3.3.1. Determination of material constants A, B, n

For $\dot{\varepsilon}_p = \dot{\varepsilon}_0$ and $T = T_{ref}$ Eq. 15 the second and third parentheses are omitted since the effects of strain rate strengthening and thermal softening are neglected. Modifying the remaining terms by taking the natural logarithm on both sides and using the averaged true stress-strain data from C1_0.001_NR; C2_0.001_NR and C3_0.001NR cases and linearly plotting the $\ln(\sigma - A)$ term with $n \ln \varepsilon$ of Eq.(18), a linear regression model was used to fit the data points as can be seen in Fig. 14.

$$\ln(\sigma - A) = n \ln \varepsilon + \ln B \tag{18}$$

The A parameter was also calculated under reference strain conditions using the 0.2% offset method. For the linear fitting presented in Fig 14, R^2 factor of more than 97% was achieved resulting in a good accuracy of the regression model. As a result of the latter, material constants B and n were calculated from the slope and intercept of the curve as 1295 and 0.5376 respectively with the A parameter being estimated as 933 MPa.

3.3.2. Determination of Material Constant C

For the purpose of this work and while not considering thermal softening effects, the Eq. 15 can be modified as:

$$\frac{\sigma}{\left(A + B\varepsilon^n\right)} = \left(1 + C \ln \dot{\varepsilon}^*\right) \tag{19}$$

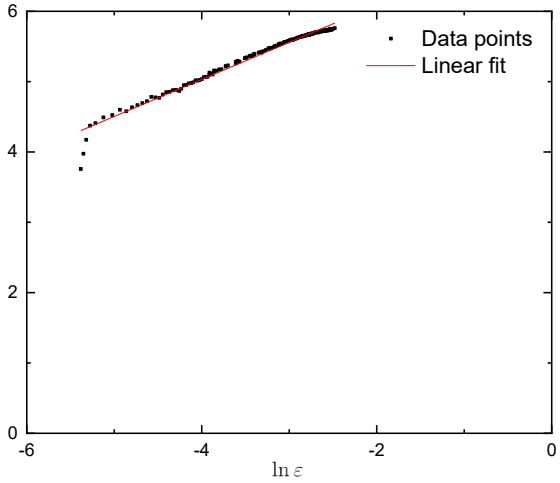

Figure 14 ln(σ-A) and lnε relationship under reference conditions.

To obtain C parameter, stress-strain data at four different strain rates ($0.001s^{-1}$, $0.5s^{-1}$, $1s^{-1}$, $2s^{-1}$) were used to plot Figure 15 while utilizing A, B, n constants that were calculated in the previous section and substituted in Eq.(19). Afterwards first-order linear fitting was performed using a vertical axis intercept value of 1 since Eq. (16) is in the form of $y = a + bx$. Similar to Figure 14, from the slope of the linear regression fit, the C parameter was calculated as 0.0221.

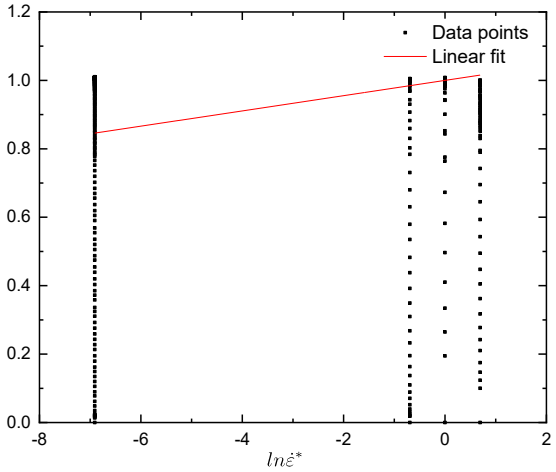

Figure 15 Relationship between $\frac{\sigma}{(A+B\varepsilon^n}$ and $ln\dot{\varepsilon}^*$ for four different strain rates ($0.001s^{-1}$, $0.5s^{-1}$, $1s^{-1}$, $2s^{-1}$).

The material constants that were calculated from the aforementioned constitutive equations for the JC model are summarized in Table 3.

Table 3 Johnson-Cook material model parameters for SBPR 930/1080 Type B No. 1.

A (MPa)	B (MPa)	C	n
933	1295	0.0221	0.5376

3.3.3. Johnson-Cook Damage Model parameters

Substituting the material constants from Table 3 into Eq. (16) the following relationships can be formed according to the JC model for stress, strain and strain deformation rate as can be seen in Eq. (20). When comparing experimental data with analytical prediction from Eq. (20), good accuracy can be observed until the onset of damage and necking of the tensile specimen (Figure 16).

$$\sigma_y = \left(933 + 1295\varepsilon^{0.5376}\right)\left(1 + 0.0221\ln\left(\frac{\dot{\varepsilon}^*}{0.001}\right)\right)(MPa) \tag{20}$$

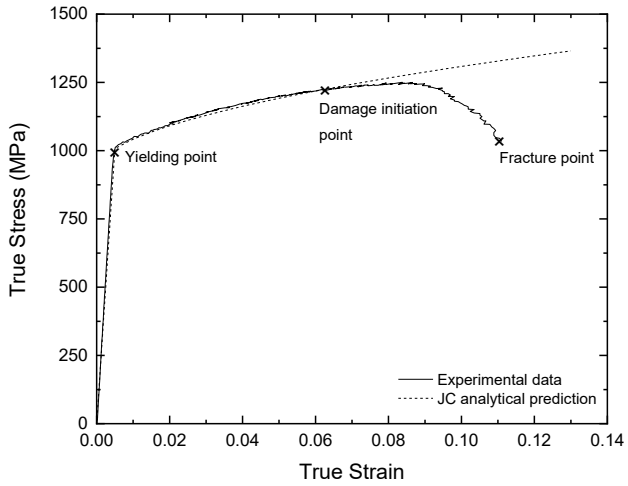

Figure 16 Comparison of true stress-strain curve between experimental data and JC analytical prediction.

To accurately simulate damage that occurs in the material model with regards to the JC damage parameter setting, it is important to define at which point damage is calculated. In this study, after careful consideration (Appendix A) the authors decided to use the Damage Initiation point of Figure 16. With that JC damage model is used to relate fracture strain with stress triaxiality ratio, strain rate as well as temperature (Banerjee et al., 2015; Johnson & Cook, 1985; Wang & Shi, 2013) and it is expressed in Eq. (21).

$$\varepsilon_f = \left(D_1 + D_2 e^{D_3\left(\frac{\sigma_m}{\sigma_{eq}}\right)}\right)\left(1 + D_4\ln\left(\dot{\varepsilon}_p^{\,*}\right)\right)\left(1 + D_5 T^*\right) \tag{21}$$

D_1 to D_5 represent damage constants for the JC model, σ_m is the mean stress and σ_{eq} is the equivalent stress. As damage occurs in an element governed by JC damage model, it is accumulated based on a damage law and can be represented by Eq. (22)(Murugesan et al.,

2017). When damage occurs, during high levels of deformation, material strength is reduced (Banerjee et al., 2015) and the resulting relation for stress during this damage evolution step is presented in Eq. (23).

$$D = \sum \left(\frac{\Delta \varepsilon}{\varepsilon_f} \right) \tag{22}$$

where $\Delta\varepsilon$ is the equivalent plastic strain increment and ε_f is the equivalent strain to fracture under certain stress, strain rate and temperature conditions.

$$\sigma_D = (1 - D)\sigma_{eq} \tag{23}$$

In Eq.(23), σ_D is the resulting stress after damage in an element has been initiated and D is a damage parameter with the following conditions $(0 \le D \le 1)$. In Eq. (21), $\frac{\sigma_m}{\sigma_{eq}}$ can be also defined as stress triaxiality ratio η^* (Y. Bai & Wierzbicki, 2008; Bao, 2005), and along with equivalent stress can be obtained from undamaged material while considering plastic deformation up until the onset of necking. According to the work of Bridgman(Bridgman, 1952), stress triaxiality values can be estimated from uniaxial tests of round specimens according to the analytical model which is presented in Eq. (24). In the model, η^* is the stress triaxiality state value, R represents the radius of notch that the specimen is manufactured according to and α represents the minimum cross section's radius. Triaxialities calculated according to Bridgman's model for different notched specimens can be seen in Table 2.

$$\eta^* = \frac{1}{3} + \ln\left(1 + \frac{\alpha}{2R}\right) \tag{24}$$

Neglecting the effects of strain rate and temperature, Eq. (21) can be simplified representing fracture strain in terms of the aforementioned D_1 to D_3 damage parameters and stress triaxiality ratio effects. When plotting the fracture strain – stress triaxiality ratio (Figure 17), using experimental tension data (Bao & Wierzbicki, 2004) with $0.001s^{-1}$ strain rate for smooth and notched specimens from Figure 13b and Table 2, in the form of $y = A + B \cdot \exp(R0 \cdot x)$; D_1 to D_3 damage parameters can be calculated from the exponential coefficients of the equation similar in principal to the derivation of Eq. (20). Afterwards the D_4 strain-rate dependent parameter was calculated by rewriting Eq. (21) complete with the previously calculated D_1 to D_3 damage parameters according to Eq. (25). In detail, when

plotting $\frac{\varepsilon_f}{D_1 + D_2 \cdot e^{D_3 \eta^*}}$ against $1 + D_4 \cdot \ln \dot{\varepsilon}^*$ (Figure 17) and using a linear regression fitting equation intercepting the vertical axis at a value of 1.0, from the slope of the resulting equation the final JC damage parameter D_4 was calculated.

$$\frac{\varepsilon_f}{D_1 + D_2 \cdot e^{D_3 \eta^*}} = 1 + D_4 \cdot \ln \dot{\varepsilon}^* \tag{25}$$

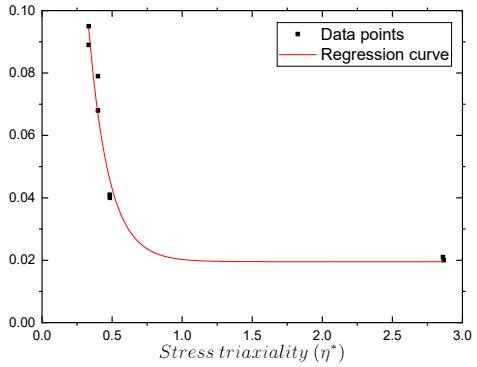

Figure 17 Fracture strain and stress triaxiality relationship from uniaxial tensile test data.

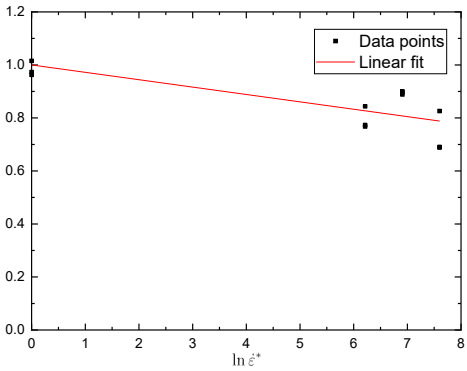

Figure 18 Relationship between $\frac{\varepsilon_f}{D_1 + D_2 \cdot e^{D_3 \eta^*}}$ and $\ln \dot{\varepsilon}^*$.

The calculated JC damage model parameters can be seen summarized in Table 4 and can be used in FE software to simulate yield and fracture of high strength tendons in prestressed concrete applications.

Table 4 Johnson-Cook damage model parameters for SBPR 930/1080 Type B No. 1.

D1	D2	D3	D4	D5
0.0165	0.6622	-6.4791	-0.0279	0

3.4. Numerical simulation

The purpose of the numerical modeling was to verify the reproducibility of the experimental results in the commercially available finite element software Abaqus (Dassault Systemes Simulia, 2021a) as part of a broader research work aimed at modeling the dynamic fracture behavior of prestressed concrete members. To accurately reproduce the dynamic fracture effects of high tensile strength tendons, non-linear dynamic analysis was used throughout the simulation process of uniaxial tensile tests. Full-scale, three-dimensional models were created, accurately reproducing the geometrical properties of the constructed specimens shown in Figure 8.

3.4.1. Numerical simulation of singular finite elements

Initially, to verify the accuracy of the analytical model in FE simulations, a single 8-noded cubical-shaped C3D8R element, measuring $1mm^3$ was modeled and suitable boundary conditions were applied to simulate biaxial symmetry in the two-axis perpendicular to the loading direction. To maintain a stress triaxiality ratio η^* of 0.333 throughout the tensile test, the bottom 4-nodes were restrained in the direction of applied force, as well as 4-nodes on each of the two faces perpendicular to the loading axis had their movement in the 2-orthgonal axis respectively restrained as can be seen in Figure 19a. The top 4-nodes were free to move in the direction of loading, and to achieve that a velocity-based loading condition was applied.

Similar to experimental procedure, loading speeds of 0.1-200 mm/s were applied to the top 4-nodes simultaneously. To reduce inertia-related effects at the beginning of the simulation, velocity amplitude was smoothly applied to the simulation for the first $1/10^{th}$ of the overall step's duration and then kept constant until the completion of each test (Figure 19b). Duration of the tensile phase of the simulation was adjusted each time according to the required strain rate in order to allow for sufficient simulation time and up until the complete damage being registered at the tested element.

In Abaqus, several ductile material models are available that can accurately capture the deformation of steel materials but in this work the JC flow stress model and correspondingly the JC damage model was utilized using material parameters that were calculated in previous

sections. Along with the data presented in Table 3 and Table 4, for this material, according to the manufacturer's specifications, Young's Modulus $E = 210$ GPa and Poisson's ratio of $\nu = 0.28$, furthermore the density was set as $\rho = 7.85E-09$ tonnes/mm^3.

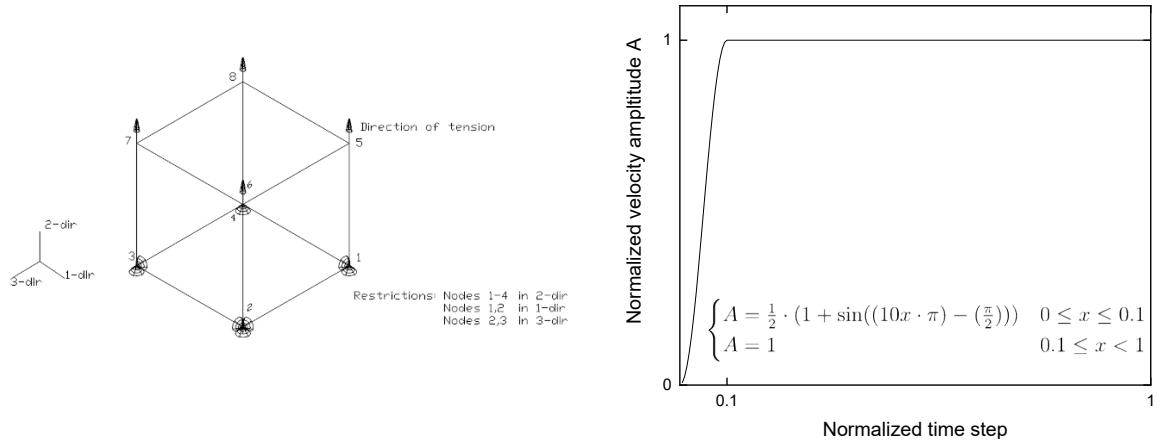

(a) (b)

Figure 19 (a)Singular element's boundary conditions used in FE simulation, (b) Smooth piecewise application of velocity amplitude.

In Figure 20 a comparison between the experimental true stress-strain curves for different strain rates of Table 2 with the results obtained from a singular finite element are presented. Overall good accuracy was achieved between experimental and numerical results with the exception of 1s^{-1} strain rate results in which although the failure strain was similar, the ultimate stress value had a difference of approximately 8%. It is believed that this is due to the non-monotonic nature of failure strain as well as ultimate stress that was observed during the experimental procedure (Figure 12b).

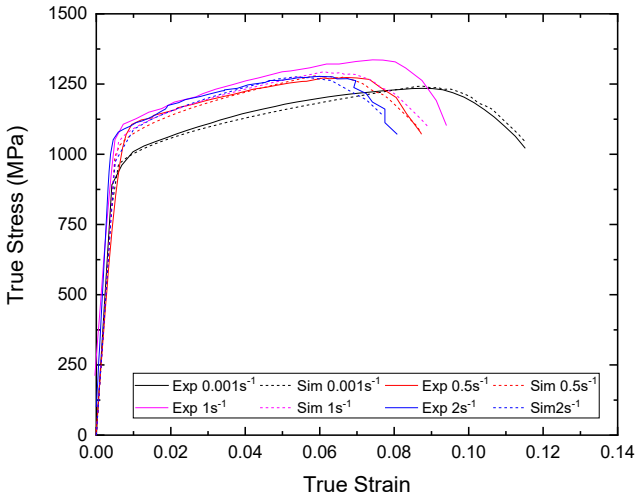

Figure 20 Comparison between experimental (Exp, continuous-lines) and FE simulation (Sim, dotted-lines) results for 0.001s-1 - 2s-1 strain rates.

To accurate model the material softening behavior past the damage initiation point (Dassault Systemes Simulia, 2021b) represented in Figure 21a in which, σ_{y0} is the yield stress and $\bar{\varepsilon}_0^{pl}$ equivalent plastic strain at the damage initiation point, $\bar{\varepsilon}_f^{pl}$ is the equivalent plastic strain at failure when the scalar damage parameter $D=1$ (Eq. (22)), damage and strain are correlated. For modeling of post damage-initiation softening until element failure data, post-peak stress σ_D is calculated based on the difference between experimental and JC analytical prediction (Figure 16). Based on the difference between relevant stress value σ_D and from Eq. (23), sets of $D-\varepsilon$ were calculated. Their respective correlation is presented in Figure 21b showing the correlation between damage parameter and equivalent plastic strain used to model softening behavior of the material in this work under reference conditions.

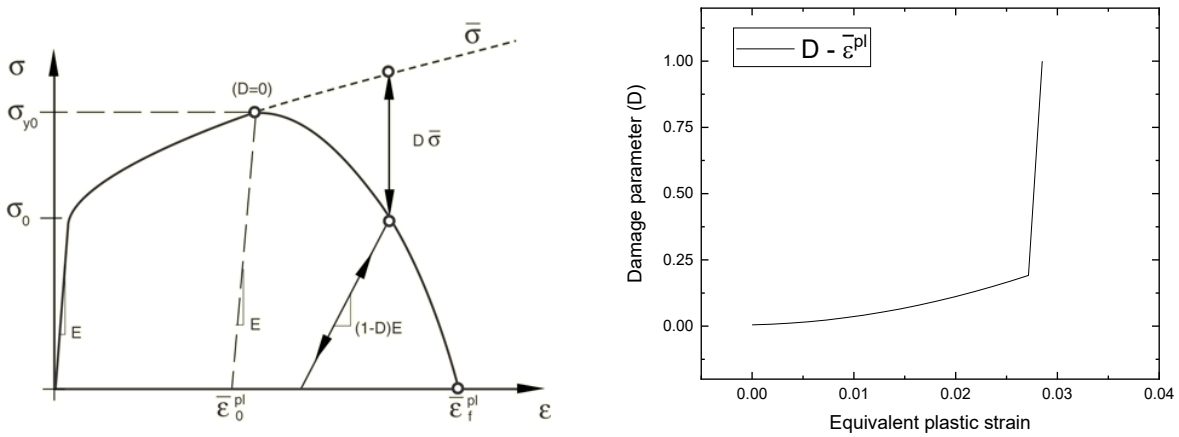

(a) (b)

Figure 21 (a)Stress-strain behavior of a characteristic material undergoing progressive damage (Abaqus Analysis User's Manual 2021) and (b) Correlation between damage parameter and equivalent plastic strain used to model softening behavior of the material in this work under reference conditions.

3.4.2. Numerical simulation of full-scale tensile specimens

To simulate the ductile failure of the dog-bone-shaped tensile specimens, a three-dimensional model was constructed, replicating in detail the geometrical properties of the manufactured tensile specimens. After some initial mesh sensitivity analysis, the maximum size of C3D8R elements was chosen as equal to 3x2x1.6 mm (coarse mesh) and the minimum size at the working length was set as 2x1x1mm (fine mesh) which resulted in a total of 20544 elements (Figure 22). For the material modeling, parameters stated in section 3 were used and

boundary conditions were utilized in accordance with the experimental setup. Similar to the experimental procedure, quasi-static 0.001s^{-1} and 0.5s^{-1} strain rate uniaxial tensile simulations were performed, and the results can be seen in Figure 23. Similar to the experimental process, in the case of numerical simulations, load, displacement were monitored throughout the uniaxial tensile test. Afterwards obtained load-displacement data were transformed into engineering stress-strain and subsequently to true stress-strain. Overall good accuracy is observed between experimental and numerical results for both cases. In particular, for the quasi-static strain rate case, apart from some initial discrepancy in the post-yielding stress capacity (numerical results overestimate the experimental case by 2.6%) the stress-strain curve follows closely the experimental results, a 2.4% difference in ultimate stress is observed. Furthermore, although the fracture strain between the numerical analysis and experimental results is similar, the numerical simulation retains a higher stress-state for larger strain value for decreasing sharply leading to element failure. For the case of 0.5s^{-1} strain rate, after yielding, the numerical model underestimates the experimental results by 2.7% but after that the numerical stress-strain curve follows closely the experimental one. Finally, a 3.6% difference is observed for the failure strain between numerical and experimental results. The above statements can be seen summarized in Table 5.

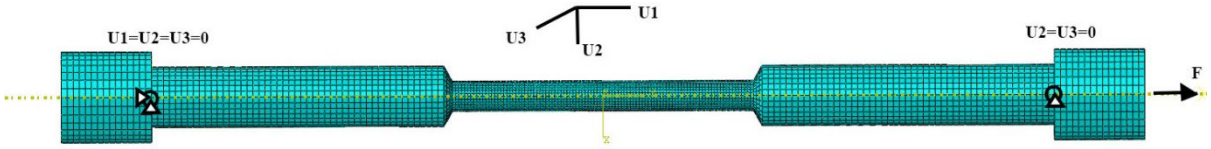

Figure 22 Mesh and boundary conditions used for numerical modeling of smooth tensile specimens.

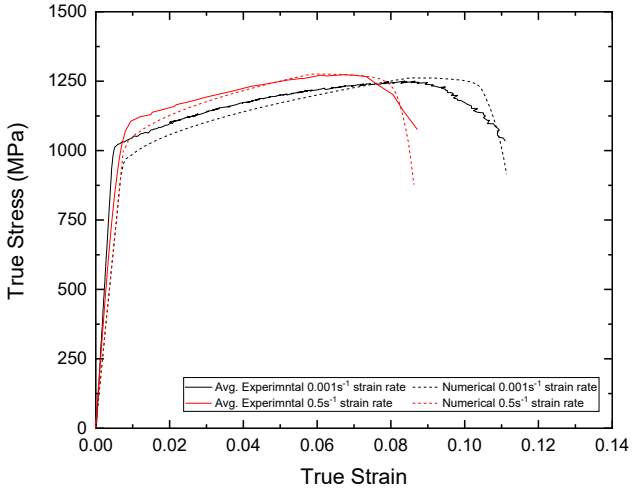

Figure 23 True stress-strain plot comparison for 0.001s-1 and 0.5s-1 strain rates for average experimental and numerical simulation using modified (Table 4) JC damage parameters.

Table 5 Comparison between experimental and numerical post-yield, ultimate stress states as well as fracture strains for 0.001s-1 and 0.5s-1 strain rates.

	Post-yielding stress (MPa)	Ultimate stress (MPa)	Fracture strain
Avg. Experimental 0.001^{s-1} strain rate	997	1231	0.111
Numerical 0.001^{s-1} strain rate	971	1261	0.101
0.001^{s-1} strain rate error (%)	2.67	-2.4	0.1
Avg. Experimental 0.5^{s-1} strain rate	1069	1272	0.087
Numerical 0.5^{s-1} strain rate	1041	1271	0.084
0.5^{s-1} strain rate error	2.69	0.01	3.57

3.5. Numerical model verification for smooth specimens

To validate the accuracy of the Johnson-Cook (JC) flow stress model and the JC damage parameters calculated in the previous sections, Digital Image Correlation (DIC) analysis was performed on specimens subjected to uniaxial tension at different strain rates. The DIC analysis was conducted using commercially available software called "GOM Correlate," which is widely used for material research and compound testing. GOM Correlate utilizes a parametric approach to ensure reliable measurement of strains. Users define initial parameters for strain surface components in the area of interest, and the software generates square-shaped facets across the entire supplied image data. A high-contrast stochastic pattern is applied by the user on the region where strain measurement is required, and the software identifies facets based on the quality of this pattern. Users also adjust the distance between adjacent facets, which directly influences the point density and spatial resolution within the area of interest (GOM GmbH, n.d., 2015a, 2015b). In this study, a full-frame CMOS camera was used to capture image series and videos with a resolution of 1920x1080 pixels for DIC analysis. The captured stochastic pattern (Figure 24) was processed using a facet size of 14 and a distance of 9 to evaluate the corresponding strain fields. To compare the experimental results with the numerical modeling, strains were recorded along the axis of the cylindrical specimens and compared with the strain at the central nodes of the finite element (FE) model. Due to limitations in the camera's video frame rate and pattern-related issues, DIC analysis was successful only for the quasi-static and

0.5^{s-1} experimental cases. For higher strain rates, attempts were made to capture a significant amount of image series using 120 fps video recording, but the available resolution was limited to 1280x720 pixels. This reduced resolution, combined with the brittleness of the coloring used for the stochastic speckle pattern, significantly limited the amount of usable data for DIC analysis. The resulting strain profiles are shown in Figure 25 for the (a) quasi-static tensile case and (b) dynamic case with a strain rate of 0.5^{s-1}. In both figures, the data along the horizontal axis for the FE case has been shifted to align with the portion of the gauge length where necking and fracture occurred. True strain and normalized gauge length data points are used for better visualization of the data. Due to the degradation of the stochastic pattern, strain data could only be captured up to approximately 0.2 for the quasi-static case.

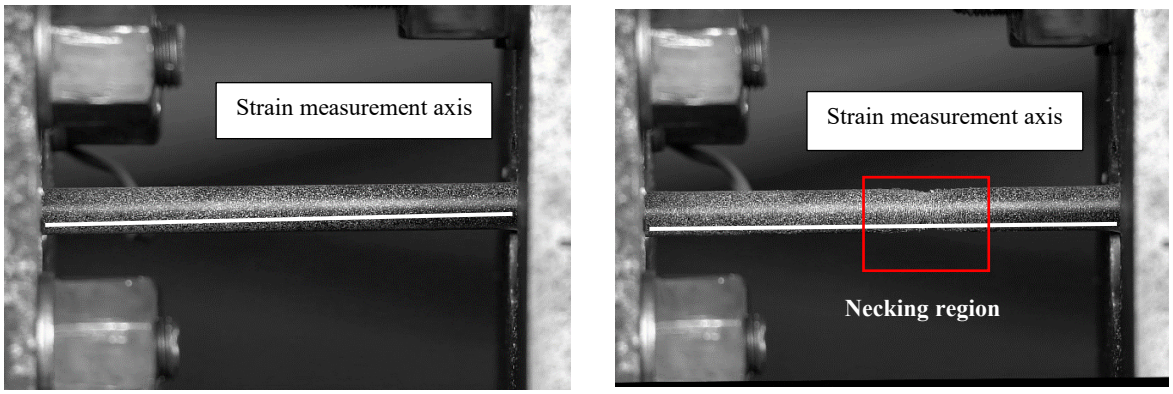

(a) (b)

Figure 24 Stochastic speckle pattern used for DIC analysis during (a) beginning of the tensile test and (b) one frame before rupture.

When comparing the results of FEM analysis with DIC for a strain rate of $0.001s^{-1}$, it was observed that the FEM analysis concentrated the high strain region around the area where necking occurs for 22.6% of the normalized length. In contrast, DIC showed a concentration of 26.5% in that region, resulting in the tensile specimen forming a longer necking region by 3.9%. For the case of a strain rate of $0.5s^{-1}$, even better accuracy was achieved, with the FEM results underestimating the length where necking occurs by 1.6%. Overall, in both cases, there was good agreement between the DIC and FEM results, which further supports the suitability of the proposed JC model and damage parameters for the SBPR 930/1080 Type B No. 1 tendon high strength material.

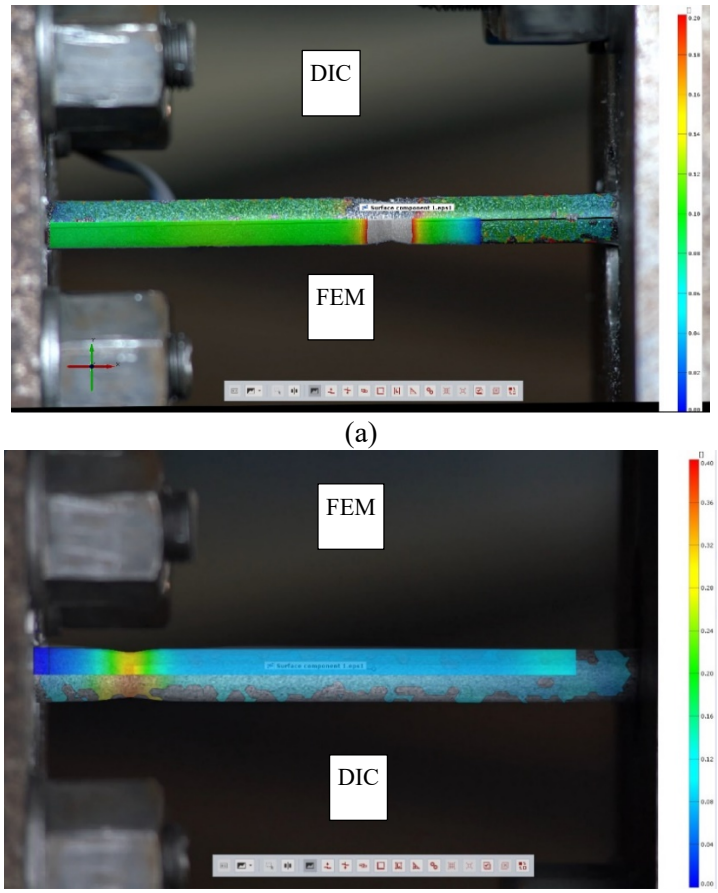

Figure 25 Comparison plots for true strain - normalized gauge length of tensile specimens. between data points obtained from DIC analysis and FE simulation for (a) 0.001s^{-1} and (b) 0.5s^{-1} strain rates.

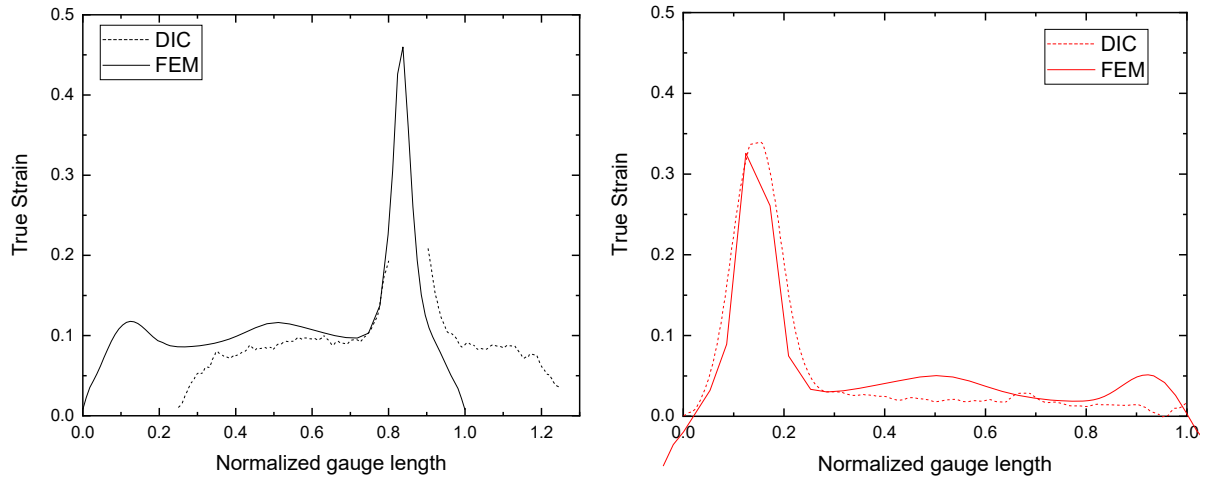

Figure 26 Visual comparison between DIC analysis and FE simulation strain map results for smooth specimens at the last captured frame before rupture for (a) 0.001s^{-1} and (b) 0.5s^{-1} strain rates.

In Figure 26, the strain maps obtained from DIC and FE simulation are superimposed to visualize the results shown in Figure 25 for smooth specimens at the final captured frame before rupture. In each corresponding figure, the strain contours from the FE simulation have been adjusted to match the values obtained from the DIC analysis, and the overlapped FEM image has been adjusted to align the necking region with the DIC image. As a result, for the case of a strain rate of $0.001s^{-1}$, the strain values near the center of the necking region exceed the visualization boundary limits of 0.0-0.2 strain. Consequently, the region with strains higher than these values is represented with a gray color.

.

Chapter 4
Experimental and Numerical Investigation of Bond-Slip Behavior of Round Bars Embedded in Mortar Considering Lateral Stresses and Pullout Rates

4.1. Bond modeling in literature

The effective and reliable utilization of steel-reinforced concrete as a composite material depends on the proper bonding between reinforcing bars and concrete and it is crucial for transferring forces between the bars and the surrounding material. In the past, plain round bars were commonly used in reinforced concrete structures, and extensive studies have been conducted on their bonding properties (Baldwin & Clark, 1995).

One of the pioneering investigations into the bond behavior between concrete and steel was carried out by Abrams in 1913 (Abrams, 1913). Abrams conducted an experimental analysis of the bond behavior of plain round bars using the pullout test. Subsequent researchers focused on both plain reinforcement bars and prestressed concrete properties. They demonstrated that the resistance to adhesion before slipping occurs due to the chemical adhesion mechanism and the micro-interlocking of concrete protrusions formed by the penetration of cement paste into the bar surface indentations. Once these protrusions are crushed at the peak bond stress, bond slip occurs, and friction resistance is initiated by the wedging action of the cement paste at the interface between the concrete and the bar. This gradual decrease in bond stress accompanies an increase in slip between the two materials. It was also found that a small amount of slip is necessary to activate the micro-interlocking mechanism for achieving maximum adhesion resistance (Stroker & Sozen, 1970; Tassios, 1980). Furthermore, it was observed that the bond stress increases as slip increases before reaching its peak value (Comité Euro-International du Béton, 1993; Xiao & Falkner, 2007).

In more recent years, researchers (Verderame, De Carlo, et al., 2009; Verderame, Ricci, et al., 2009) conducted experimental research to investigate the cyclic bond behavior of plain bars. Their findings revealed that the bond capacity significantly deteriorates with an increase in the number of cycles and/or the imposed displacement in each cycle. They also established an analytical relationship between bond stress and slip for plain bars. Additionally, experiments

were conducted on the bond behavior of plain bars embedded in various special concretes, such as recycled aggregate concrete (Xiao & Falkner, 2007), high-performance concrete (De Larrard et al., 1993), and lightweight aggregate concrete (Hossain, 2008; Robins & Standish, 1984). The literature extensively reports the effects of various experimental factors, including bond length, bar size, concrete strength, and loading rate.(Edwards & Yannopoulos, 1979; Feldman & Bartlett, 2005; Mo & Chan, 1996). Feldman and Bartlett also proposed a theoretical model that analytically correlates these parameters with their effect on bond stress distribution (Feldman & Bartlett, 2007).

Previous research on the bond-slip behavior between concrete and plain bars has largely overlooked the influence of lateral confinement or stresses. However, in the case of beam-column joints in simply supported and continuous structures (Taylor & JL, 1976), lateral confinement plays a crucial role in the development of bond strength between concrete and deformed bars (Untrauer & Henry, 1965). This effect has also been studied for steel strands (Laldji & Young, 1988) and fiber-reinforced polymer bars (Malvar, 1995; Malvar et al., 2003). In recent years, several researchers have investigated the effect of lateral pressure on bond development, strength, and behavior specifically for plain round bars (Cairns, 2021; Wu et al., 2014; Xing et al., 2015; F. Xu et al., 2014). Extensive experimental testing, primarily through static uniaxial pull-out tests of plain bars embedded in concrete specimens subjected to varying lateral stresses, has revealed that both peak lateral stresses and slip tend to increase with greater lateral confinement. Conversely, the size of the bar has little influence on bond strength. Additionally, in dynamic testing (with strain rates ranging from $10s^{-4}10$ to $10s^{-1}$, although the results are inconclusive, the trend suggests that the peak bond stress is linearly proportional to the logarithm of the strain rate ratio (Li et al., 2021). Most of the research involving experimental evaluation of bond behavior has been followed by the development of a constitutive model for bond stress-slip behavior, which is calibrated based on the specific research findings. Overall, good agreement has been observed, but the accuracy of each constitutive model varies significantly depending on the similarity of the experimental data used during the calibration process.

When discussing the interaction between an object embedded in a material (strands, fibers, sheets, bars) that resists relative movement, it is common to refer to this interaction from a

constitutive perspective as a bond stress-slip ($\tau - s$) model. In the case of bars embedded in concrete, the bond stress is unevenly developed and distributed along an embedded length that is typically 20 to 30 times the diameter of the bars (Feldman & Bartlett, 2007; Mains, 1951). However, when the embedded length is reduced to up to 5 times the bar diameter, the bond stress can be considered as uniform (Rilem, 1970). This allows researchers to propose localized τ-s models and utilize them in (FEM) applications.

The fib Model Code 2010 (Du Béton, 2013) discusses idealized constitutive models for both deformed and smooth bars subjected to uniaxial pullout forces. Specifically, for smooth plain bars, the peak bond strength is considered to be between $0.15\sqrt{f_{cm}}$ and $0.30\sqrt{f_{cm}}$, depending on the assumed bond conditions, at a slip value of approximately 0.1mm. After reaching the peak, the bond strength remains constant throughout the pullout process. Here, $\sqrt{f_{cm}}$ represents the modified cylindrical compressive strength of concrete. In recent years, the constitutive model initially proposed by Eligehausen et al. (Eligehausen et al., 1982) and later modified by Cosenza et al. (Cosenza et al., 1997) for FRP rebars has been tested for smooth bars by Verderame et al., and it was found to accurately describe the local bond behavior of smooth plain bars. This constitutive model consists of three parts: an ascending branch formulated by a power-type equation, a linear descending branch, and a horizontal part representing residual bond strength. More recently, Cairns (Cairns, 2021) proposed a stress-slip model for constitutive bonding, featuring one ascending and one descending branch. Figure 27 provides a schematic representation of these three modeling approaches.

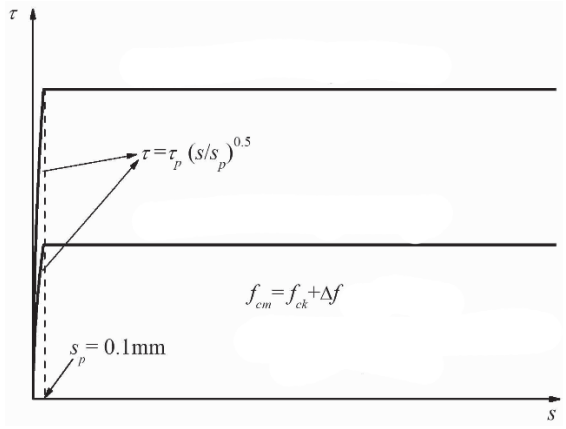

Fib model code

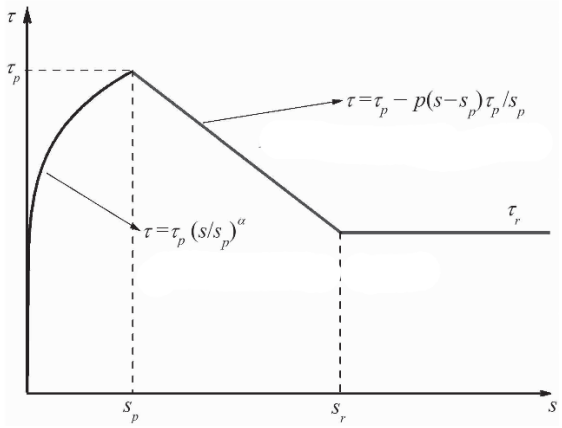

Modified Cosenza model

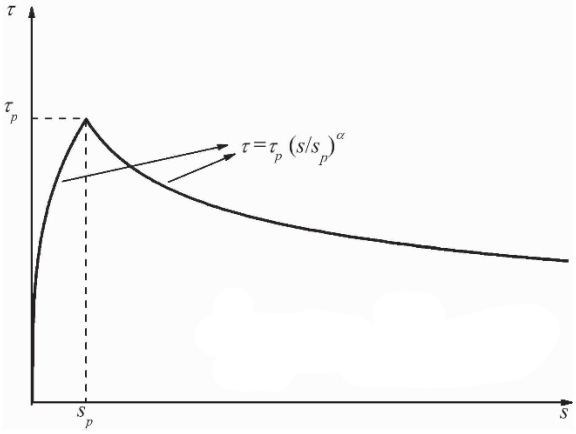

Cairns model

Figure 27 Constitutive bond stress-slip model for smooth bars

In Figure 1, for the left figure the upper model line represents good bonding condition whereas the bottom one represents poor bond conditions. f_{ck} is the concrete cylindrical compressive strength (MPa) and Δf= 8 MPa. In the Cosenza model, α represents the power of the ascending branch and p represents the slope of the descending one. In the Cairns model α represents a power-type parameters which takes positive values for the ascending part and negative for the descending one.

From the performed literature investigation, it was identified that to accurately model the bond behavior of plain smooth bars embedded in grouting mortar during uniaxial pullout it is essential to properly define material parameters and calibrate the model. The data required for model calibration need to be obtained through extensive and time-consuming experimental effort and both static, dynamic and lateral compression conditions to simulate both peak bond

stress, slip and well as remaining bond stress parameters. For normal and high strength mortar commonly used in civil infrastructure such material parameters are not readily available. In this work, to investigate the bond behavior of plain round bars embedded in PC-tendon grouting mortar commonly used in civil infrastructure, subjected to biaxial lateral pressures and pullout rates several experimental tests were performed. Effects on grouting mortar strength and embedded bar diameter were also examined. Based on the results, an analytical model is initially calibrated and proposed. Finally finite element modelling was utilized to replicate pullout procedure and to investigate axial stresses in both the grout material and the bar as well as bond, slip development and interface layer deformation in order to obtain a deeper understanding into the mechanics of bond failure.

4.2. Pullout testing materials and experimental procedure

In this research SS400 medium carbon structural steel was used for the plain bars that were constructed with diameter of 11, 16 and 19mm that were embedded into grouting mortar and their parameters can be seen in Table 6. For the grouting mortar, two different strengths normal (NS) and ultra-high strength (UHS) supplied by the same manufacturing company were used and their properties are presented in Table 7. To perform the uniaxial pullout experiment, 22 cubical specimens were constructed measuring 140x140x140 mm with the plain bars positioned in the center of the geometrical center of the top face of the cube and specimens were casted in such a way as to allow for optimal bonding conditions as well as centering of bar with the grouting mortar specimen. Although the bars penetrate the whole depth of the cube, only five times their respective diameter is allowed to be in contact and thus bond with the grouting mortar in order to maintain uniform bond stress at peak bond stress value. Custom-made strain gauges(Hori, 2014) were also embedded in the grouting mortar at a close proximity to the bar in the middle of embedded region and perpendicular to the pullout direction in order to measure the strain in the specimen and thus the amount of lateral compressive stress applied during the experimental procedure (Figure 28).

Table 6 Mechanical properties and geometric parameters of SS400 plain bars

Type	D11	D16	D19
Nominal diameter D (mm)	11	16	19
Yield strength (MPa)	400	400	400
Elastic modulus (GPa)	210	210	210
Poisson's ratio	0.3	0.3	0.3
Embedment length	55	80	95

For the pullout tests MTS 244.11 servo-hydraulic actuator (Figure 29) was used. Despite the dynamic characteristics of the experimental procedure, experimental parameters were well within the capability envelope of the utilized actuator. The actuator was mounted on a loading frame using ball-joints for both fixed and extendable part of the piston to allow for increased mobility and flexibility under various testing conditions and requirements. For this research, both specimens and actuator were positioned and fixed in a vertical orientation to ensure an inline application of pulling force and to apply the bilateral compressive stress onto the specimen manually operated hydraulic jacks along with restriction bars plates were utilized (Figure 30). To ensure no stress-free relative movement between the extendable part of the actuator the top of the smooth bar was modified in such a way as to create threads were used to attach matching locking nuts in order to ensure direct force transmission. Finally, to ensure no vertical movement of the grout specimen during the pullout, a machined plate were installed and fixed on top of it having a large opening in the middle to allow for the smooth bar to pass through. In order to simplify the experimental procedure and reduce related costs, two hydraulic jacks were positioned in the two orthogonal directions to the pullout axis in such a way as to maintain perpendicular application of force to the other two orthogonal faces of the of the cubical specimen. Restriction plates and rods and suitable size bolts for the applied load were positioned and fixed in the opposite side of the extendable part of the hydraulic jacks in order to provide a fixed boundary condition and allow flow steady and controlled load application.

Table 7 Mechanical properties of used grouting mortar

Type	NS	UHS
Nominal compressive strength (MPa)	70	120
Grouting cement : water	1.7 : 0.3	1.7 : 0.3
Elastic modulus (GPa)	33.2	33.2
Poisson's ratio	0.22	0.22

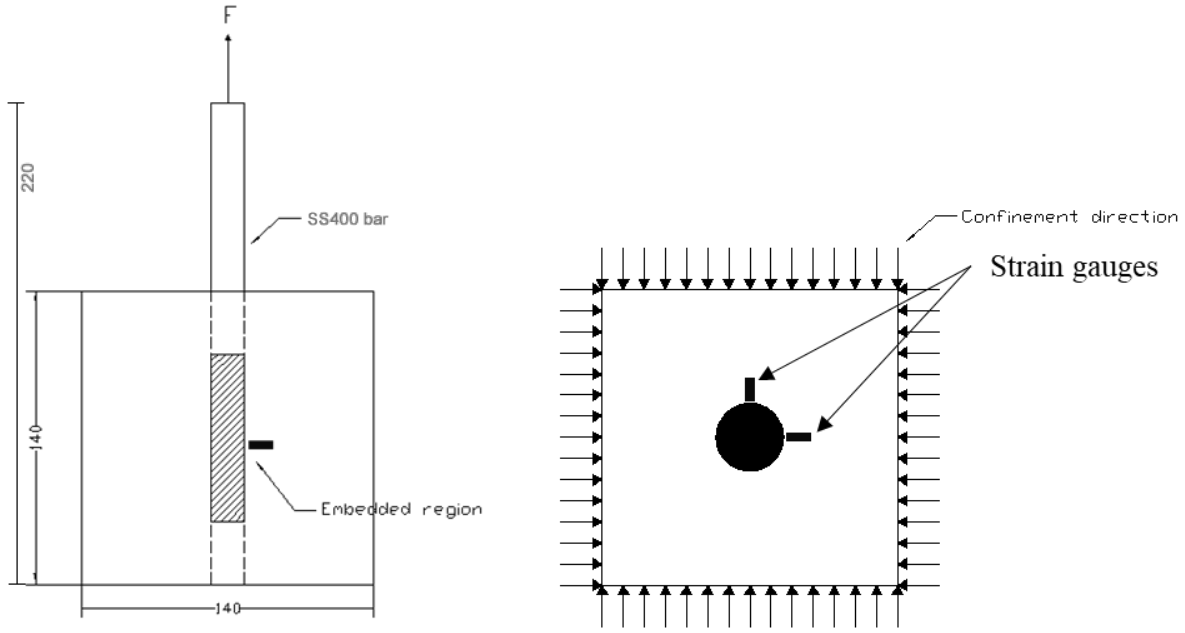

Figure 28 Detailed specimen setup and geometrical characteristics: (left) cross-section view; (right) top view

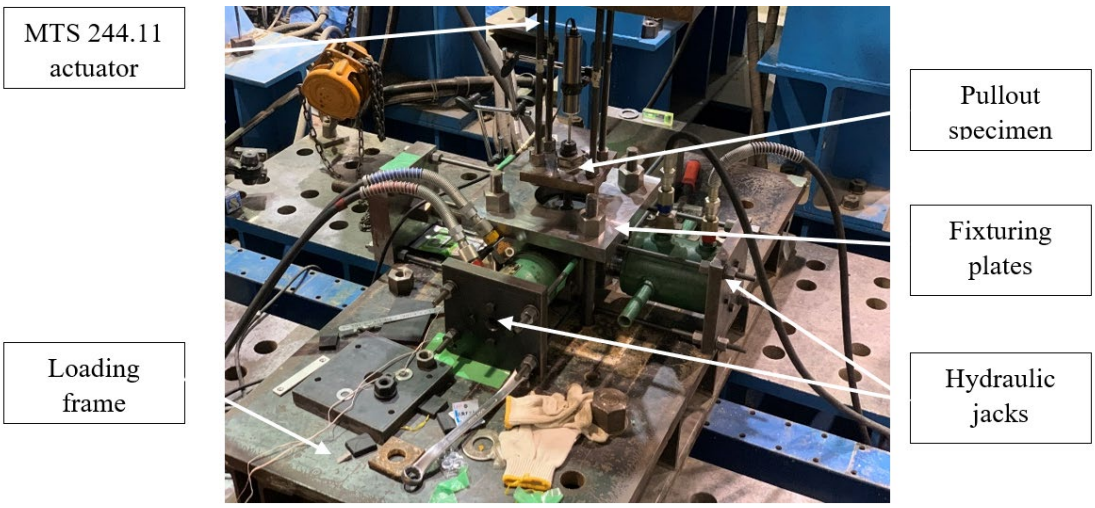

Figure 29 Pullout experimental setup

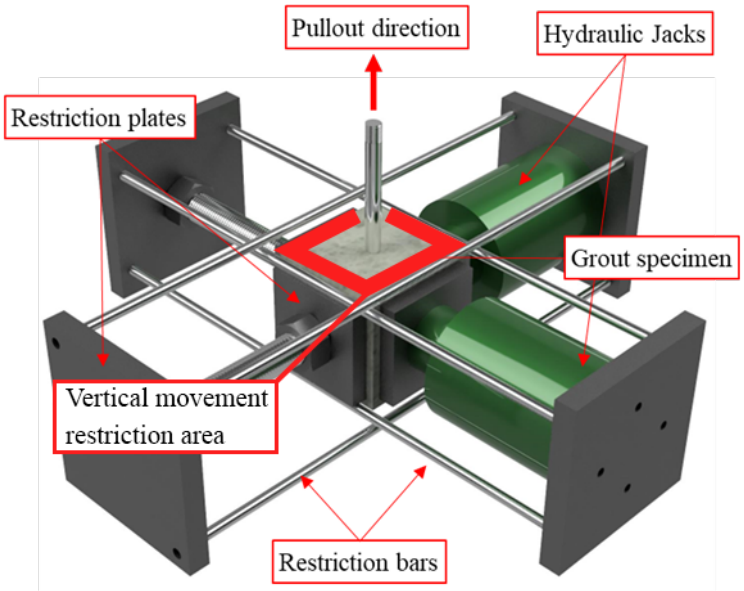

Figure 30 Detailed graphical representation of uniaxial pullout test setup.

As can be seen in Table 8, experimental cases were divided into five categories: in the first four of them NS static; UHS static; NS dynamic; UHS dynamic no lateral compression was applied and for the last category a combination of both NS and UHS with applied lateral pressure(p) is listed. In the table recorded compressive (F_{cu}); tensile stress (F_t) from separate uniaxial compression and split-tensile experimental procedure is also presented for each respective casting batches and are accompanied by their abbreviations respectively. Finally recorded slip values are presented at peak bond stress S_0.

In Figure 31 shear bond stress-slip curves can be seen for the 22 specimens listed in Table 8. All specimens during the uniaxial pullout test failed in a shear manner at the interface between the bar smooth bar and the surrounding mortar. It should be noted that for each recorded stress-slip curve similar behavior was observed. The curves consist of three parts; one ascending up to peak shear bond stress τ_u; one descending up to a minimum value by which the chemical bond between bar and grouting mortar has completely degraded and a residual part as a result of friction at the interface between the two materials τ_r. Figure 31a shows NS grouting mortar stress-slip curves for static pullout rates for bars of varying diameter. It can be seen that although for all cases similar peak bond stress is observed, for the case of NS11CL0, residual shear stress is measurably decreased compared to NS16CL0 and NS19CL0. It is assumed that the reduction in residual bond strength at large slip values may have been due to experimental-related setup misalignment (bar axis – loading direction). In Figures 6b, 6c where

pullout cases with dynamic rates of 0.5 and $1s^{-1}$ are shown, although variation in residual stress is evident at high slip values no clear trend is observed for both bar diameter and pullout rates. Similar observations can be made for the UHS cases of Figure 31 6d; 6e; 6f in which due to higher strength grouting mortar used, both higher peak bond strength as well as residual bond stress are higher than NS cases.

Table 8 Bond Parameters for specimens subjected to Bi-lateral compression.

Specimen	p/F_{cu}	F_{cu}	F_t	S_0
NS11CL0	0	73.06	3.24	0.190
NS16CL0	0	73.06	3.24	0.209
NS19CL0	0	73.06	3.24	0.227
UHS11CL0	0	118.16	5.70	0.261
UHS16CL0	0	118.16	5.70	0.270
UHS19CL0	0	118.16	5.70	0.330
NS11D0.5L0	0	74.45	3.46	0.235
NS16D0.5L0	0	74.45	3.46	0.170
NS19D0.5L0	0	74.45	3.46	0.230
UHS11D0.5L0	0	119.06	5.76	0.308
UHS16D0.5L0	0	119.06	5.76	0.279
UHS19D0.5L0	0	119.06	5.76	0.340
NS11D1L0	0	72.47	3.72	0.180
NS16D1L0	0	72.47	3.72	0.188
NS19D1L0	0	72.47	3.72	0.276
UHS11D1L0	0	118.63	5.88	0.230
UHS16D1L0	0	118.63	5.88	0.220
UHS19D1L0	0	118.63	5.88	0.274
NS16CL17	0.25	73.06	3.24	0.218
NS16CL35	0.50	73.06	3.24	0.235
UHS16CL30	0.25	118.16	5.70	0.281
UHS16CL60	0.50	118.16	5.70	0.362

(NS/UHS)(##)(C/D##)(L##)

NS/UHS	Normal strength grout / High strength grout
##	Bar diameter (mm)
C/D##	Static / Dynamic pullout rate
L##	Lateral confinement

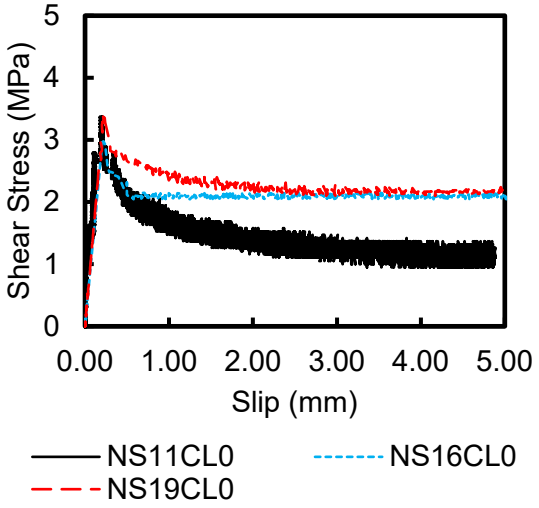

(a) Normal strength grout /D=11~19 mm /Static /Confinement 0

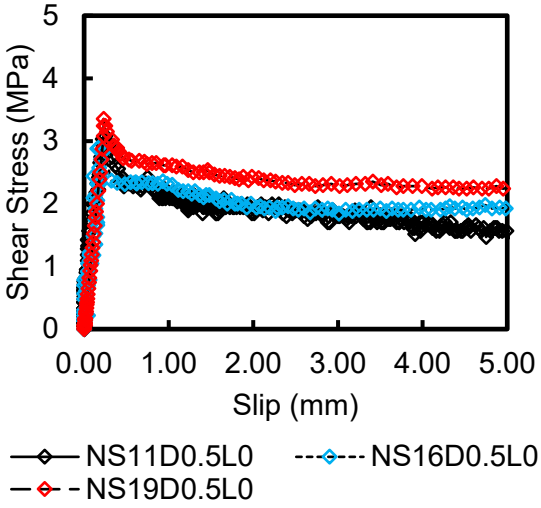

(b) Normal strength grout /D=11~19 mm /Dynamic 0.5 s^{-1} /Confinement 0

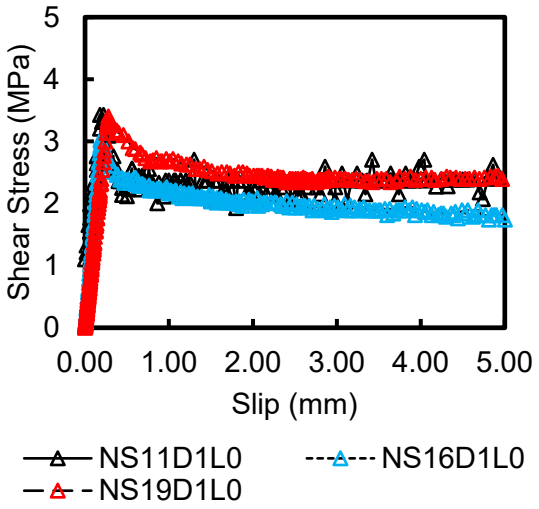

(c) Normal strength grout /D=11~19 mm /Dynamic 1 s^{-1} /Confinement 0

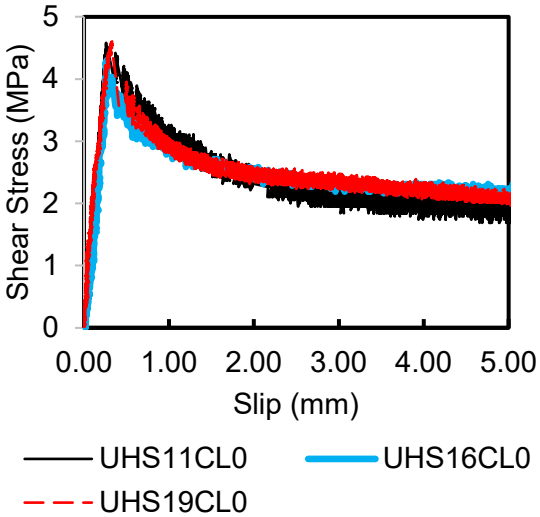

(d) High strength grout /D=11~19 mm /Static /Confinement 0

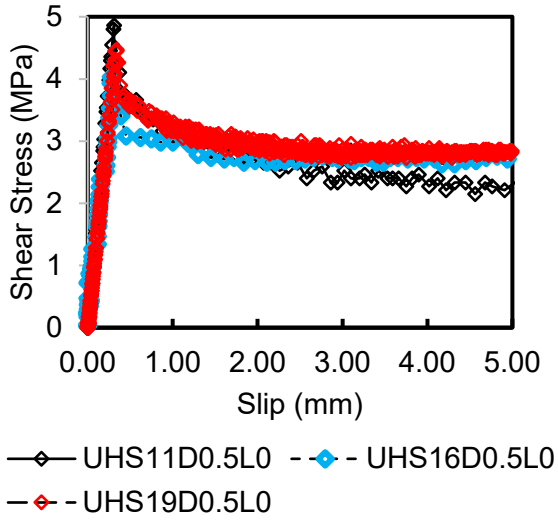

(e) High strength grout /D=11~19 mm / Dynamic 0.5 s^{-1} / Confinement 0

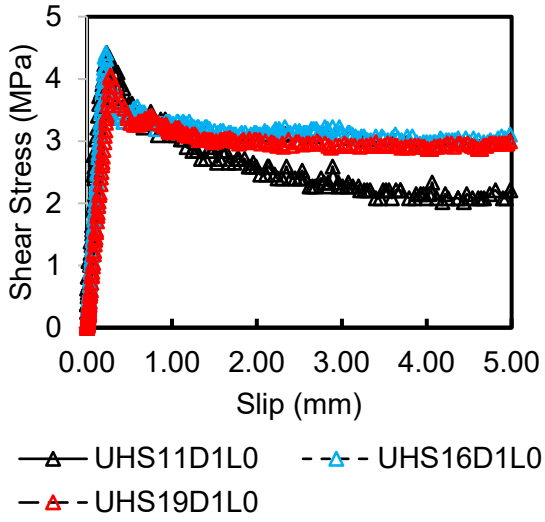

(f) High strength grout /D=11~19 mm /Dynamic 1 s^{-1} / Confinement 0

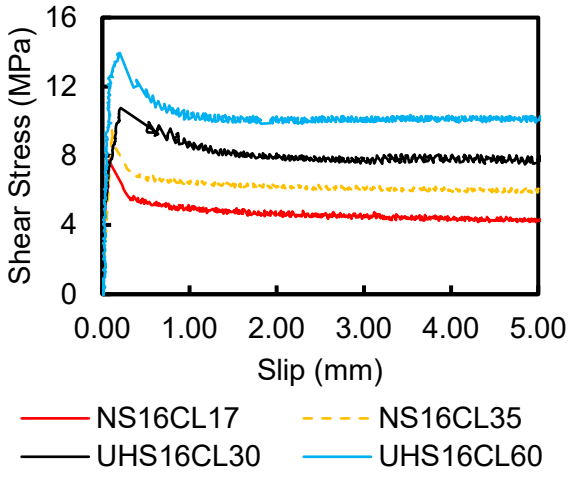

(g) Normal or High strength grout /D=16 mm / Static / Confinement =17~60 MPa

Figure 31 Bond stress-slip corves for NS and UHS specimens under static, dynamic pullout rates and lateral biaxial stresses

In this case UHS11CL0 did not present a reduction in residual bond strength at large slip values, and no significant variability for dynamic pullout rates. In Figure 31g, when lateral stress is applied there is a distinct increase in both maximum as well as residual bond stress proportional to the amount of lateral stress applied to the specimens. In the case of applied lateral biaxial stresses onto the grouting mortar specimens, $0.25F_{cu}$ and $0.50F_{cu}$ were chosen according to the stress application limitation of the manually operated hydraulic jacks and while limiting applied stress to the linear elastic zone of the grouting mortar. Additional analysis of the experimental pullout test results in Figure 32 shows that for both Ns and UHS

cases, no clear correlation can be made between peak bond stress, bar diameter and pullout rate. In case of residual bond stress at large slip values, increasing pullout rate correlates in small degree to higher stress values. In Figure 33 visual inspection of post-shear failure of pullout specimens is presented. After completion of the experimental procedure, specimens were split open into two parts along the bar axis in order to confirm surface finish of bonded region; casting conditions, shear failure along the interface and position of embedded strain gauges after casting. Visual inspection of the specimen's cohesion zone resulted in verifying good casting and as a result good bonding conditions between the plain smooth bar and the surrounding grouting mortar. Furthermore, embedded strain gauges remained perpendicular to the bar axis after casting and to an orthogonal direction to each other.

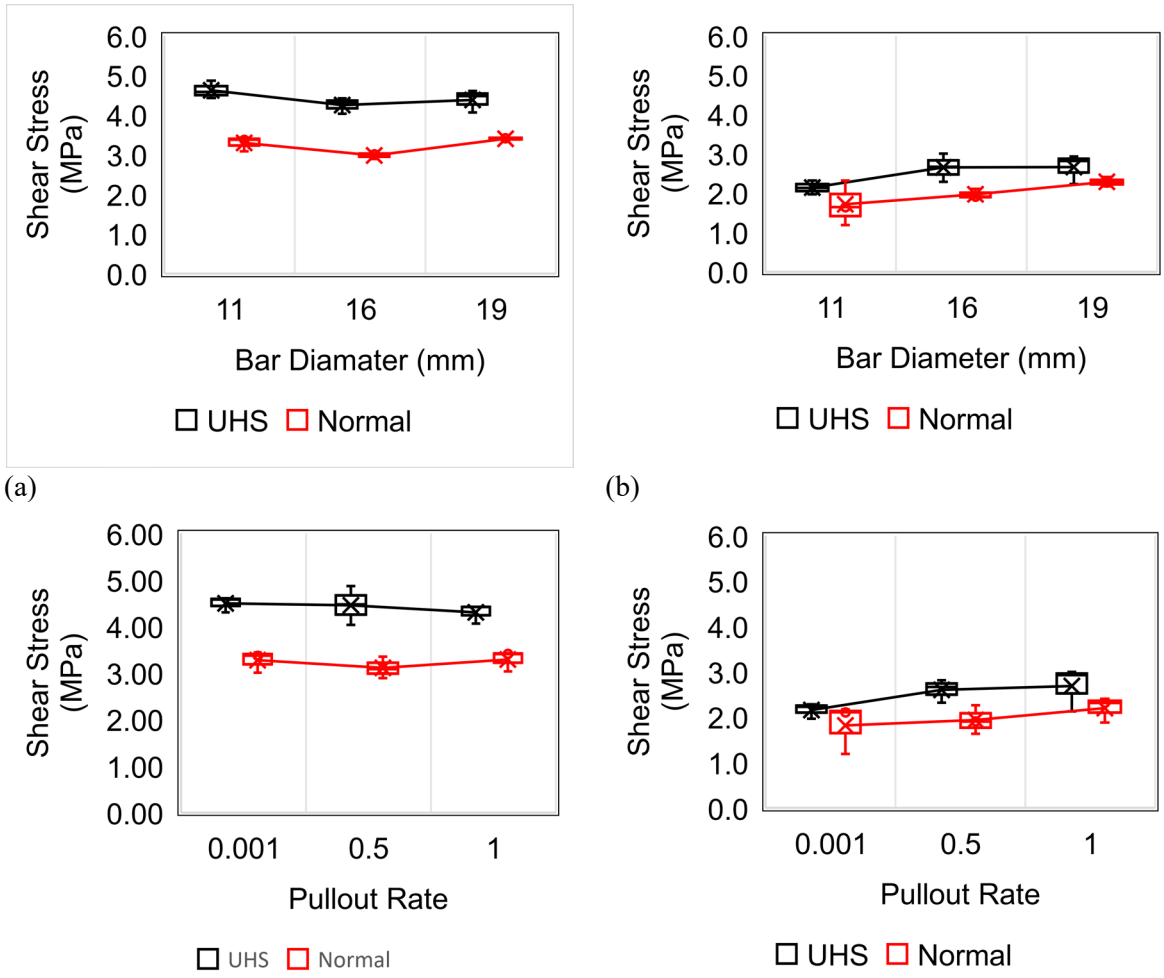

Figure 32 Peak and residual stress for uniaxial pullout experiment with varying bar diameter and pullout rates for peak (left) and residual (right) bond shear stresses.

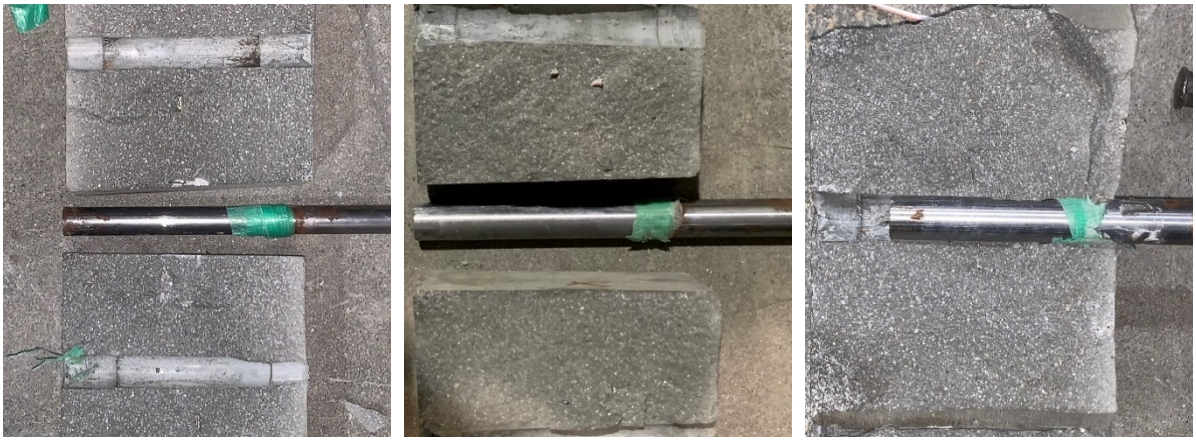

NS11CL0 UHS16D0.5L0 UHS19D1L0

Figure 33 Bonding condition visual inspection for NS11CL0; UHS16D0.5L0 and UHS19D1L0.

4.3. Bond stress constitutive model

The proposed bond constitutive model consists of two parts, one power-type (Equation 25) ascending up to peak shear stress $\boldsymbol{\tau_u}$(Equation 26) at a slip value of $\boldsymbol{s_0}$; and one softening or descending part that follows an exponential softening up (Equation 27) until remaining bond stress $\boldsymbol{\tau_r}$.

$$\tau = \tau_u \left(\frac{s}{s_0}\right)^b \qquad 26$$

In Equation 26, s represents incremental slip during pullout and b is a power-parameter with $b \geq 1$ that governs the shape of the ascending part of the curve. Analytical simulation of experimental results has shown that depending on the experimental data, using $b = 1$ may be appropriate to accurate simulate the ascending part of the curve but for weaker concrete or mortars a higher value may be more appropriate to simulate softer increase of bond stress.

$$\tau_u = \alpha\sqrt{F_{cu}} + \tau_r \qquad 27$$

In the equation above α represents a grouting mortar to plain bar coherence parameter with $0.1 \leq \alpha \leq 0.5$. Although α in the current experimental work was used as a fitting parameter to allow for accurate approximation of the experimental results utilizing a constitutive model, through more extensive and controlled experimental procedure calculation of this parameters through analytical procedure may be possible.

In Equation 27, softening part of the constitutive model is presented. This part represents bond degradation until complete loss of cohesive action and up to a residual bond stress that is the result of friction between grouting mortar particles and the smooth bar at the interface layer. The softening curve assumes an s-curve shape from a maximum initial value of τ_u to a minimum value of τ_r, with the shape of the curve being defined through an exponential parameter which sets slip boundaries between the initial slip value s_0 and slip at complete bond degradation s_f. Additionally, C represents bond degradation parameter and is dependent on the stiffness of the grout mortar or concrete (Equation 28).

$$\tau = \tau_u + (\tau_r - \tau_u) exp\left(C\left(1 - \frac{s_f - s_0}{s - s_0}\right)\right) \quad 28$$

$$C = \frac{E_{0.6\tau_u}}{E_{\tau_u}} \quad 29$$

with E_{τ_u} representing initial grouting mortar stiffness and $E_{0.6\tau_u}$ the stiffness at $0.6\tau_u$. The parameter associated with residual bond strength τ_r (Equation 29) is calculated based on a modified interface radius concept (Qiu & Zhou, 2016). In this approach (Figure 34) when a round solid object is embedded into another round solid object having lower stiffness that is subjected to compressional stresses, the later one will experience elastic deformation and due to the existence of a stiffer material at the center of it said deformation will be concentrated at the interface of the two materials. Such deformation produces normal forces which in return are responsible for frictional stresses at the interface.

$$\tau_r = \frac{\delta_r}{\frac{r}{E_m}(1 + v_m) + \frac{r}{E_b}(1 - v_b)} \quad 30$$

with δ_r being the interference radius which was calculated experimentally as the product of recorder strain near the interface with the length of the utilized strain gauge. r represents the radius of the embedded smooth bar; E_m, E_b the young's modulus of the grouting mortar and smooth bar respectively. In a similar manner, v_m, v_b represent the Poisson ratio for the mortar and bar respectively. To include the effects of pullout rate on the constitutive model τ_r and C can be modified according to Equations 30, 31 respectively. In particular, the dynamic residual shear stress τ_r^d is calculated based on determining the ratio of a reference pullout rate $\dot{\varepsilon}_0$ and

each individual dynamic pullout rate according to the procedure described in Gkolfinopoulos et al. (Gkolfinopoulos & Chijiwa, 2022).

$$\tau_r{}^d = \tau_r \left[A * log\left(\frac{\dot{\varepsilon}}{\dot{\varepsilon_0}}\right)\right] \quad 31$$

$$C^d = C\frac{\tau_r^d}{\tau_r} \quad 32$$

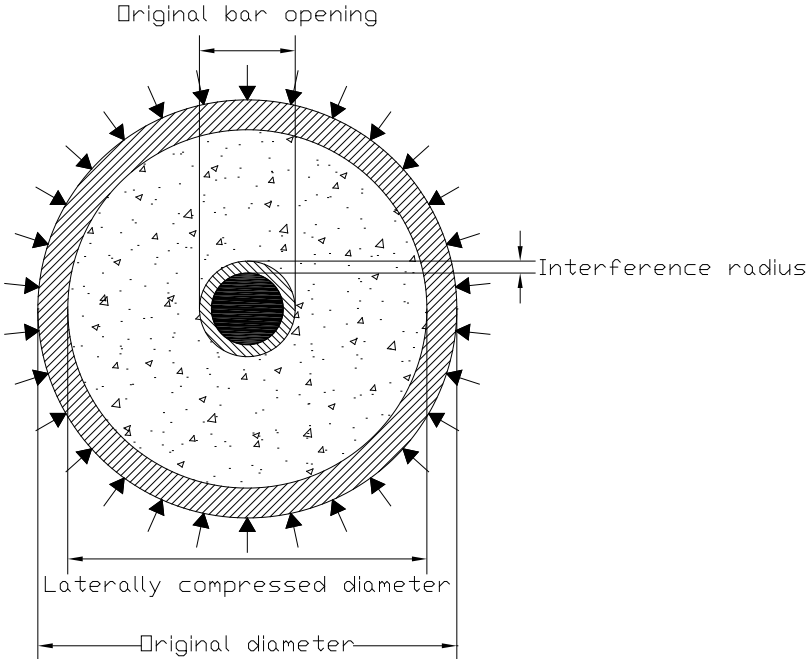

Figure 34 Residual bond stress - Interference model.

In summary, effective use of this model requires values to be known from either experimental procedure of individual material data regarding embedment material compressive strength f_{cm}, Young's modulus and Poisson ratio for embedment and embed material E_m, E_b, v_m, v_b respectively. Additionally embedded bar diameter r is required along with the slip value at which peak bond shear stress is recorded.

Comparing the experimental pullout test results with the analytical obtained from the constitutive model good accuracy was confirmed for both static (Figure 35a), and dynamic pullout rates (Figure 35 10b) along for both NS and UHS grouting mortar (Figure 35 10c, d). In particular, due to the equation used to describe the bond degrading part of the bond stress-slip curve, increase in residual bond stress after 0.5mm slip for the case of NS16CL0 was not

reproduced in the analytical results but such recorder performance might be erratic and does not agree with the general trend seeing in other researcher's work. For the dynamic NS cases, small increase in residual bond stress at large slip values in comparison to the static cases was reproduced in the analytical model.

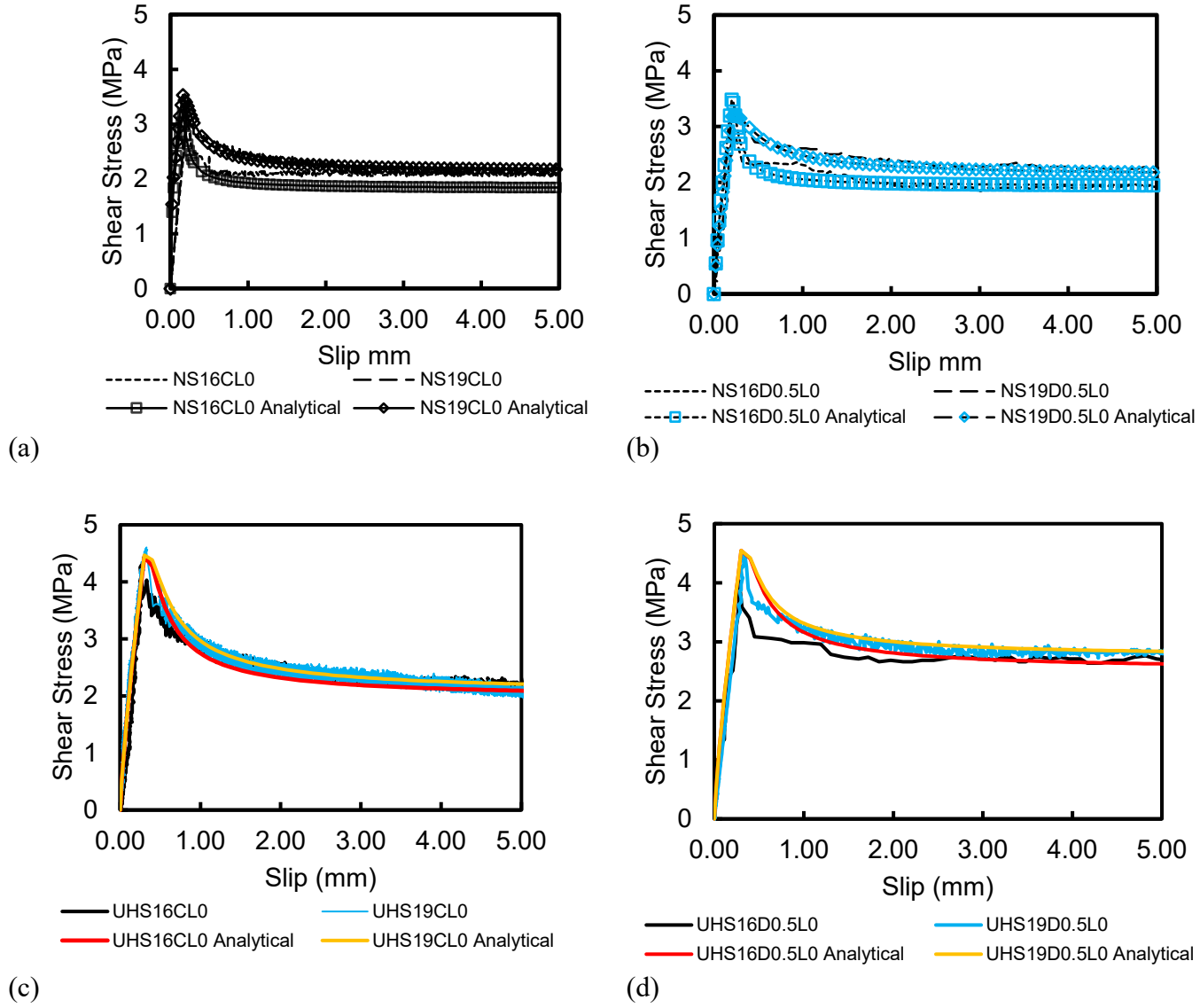

Figure 35 Comparison between experimental pullout test results and constitutive model bond stress-slip analysis results for NS; UHS; static and $0.5s^{-1}$ pullout rates.

For the experimental cases with biaxial lateral compressive stress applied to the mortar specimen using the aforementioned hydraulic jacks good agreement was observed between experimental case results and analytical using the aforementioned constitutive model as can be seen in Figure 36. In particular for the case of analytically simulating the NS16CL35 pullout

result, the constitutive model underestimated the degree of bond stress reduction at small slip values but as the slip increased similar accuracy was noted compared to Figure 35. Additionally, for the case of simulating UHS16CL30, small degree of overestimation of bond stress reduction up to slip of 1.0mm but that can be a result stick-slip effect which the proposed constitutive model cannot replicate.

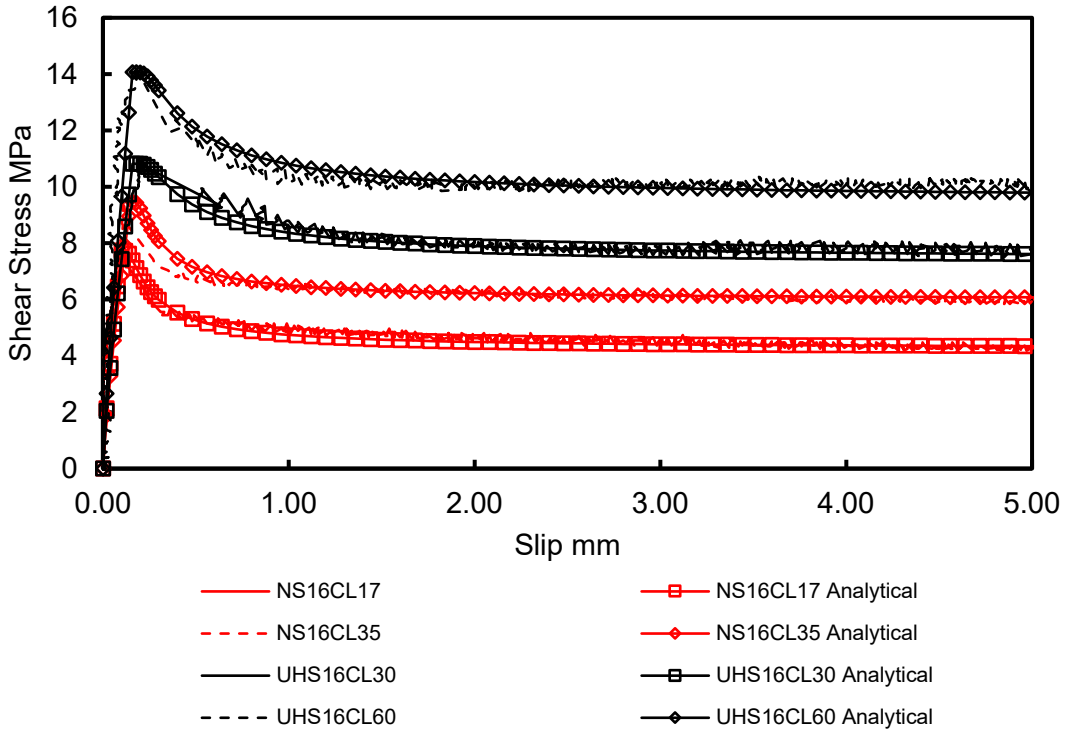

Figure 36 Comparison between experimental pullout test results and constitutive bond model stress-slip analysis results for NS; UHS with varying biaxial lateral stresses

4.4. Proposed constitutive bond model verification

To investigate and verify the applicability of the proposed model, selected experimental data from the work of Li et al. (Li et al., 2021) were chosen for 35; 50 MPa typical concrete strength and bar diameter from 12 – 20mm as well as varying pullout rates as can be seen on Table 9.

Table 9 Experimental data parameters from Li et al. 2021 that were used to validate the applicability of the proposed constitutive model.

	Concrete strength (MPa)	Bar diameter (mm)	Pullout rate (s^{-1})	δ_r
C35d12-1	35	12	10^{-4}	3.12 x 10^{-4}
C35d12-2	35	12	10^{-3}	3.13 x 10^{-4}
C35d12-3	35	12	10^{-2}	3.12 x 10^{-4}
C35d12-4	35	12	10^{-1}	3.14 x 10^{-4}
C35d16-1	35	16	10^{-4}	3.14 x 10^{-4}
C35d20-1	35	20	10^{-4}	3.12 x 10^{-4}
C50d16-1	50	16	10^{-4}	3.20 x 10^{-4}

In their work, no experimental data are provided regarding concrete strain at the interface layer where the embedded bar is located, and for that reason δ_r values listed in Table 9 were chosen as to provide a good fitment between experimental results analytical model as can be seen in Figure 37 Comparison between experimental tests data of Table 9 from (Li et al., 2021) with constitutive model results presented in this work for: (a) varying pullout rates (b) varying bar diameter and concrete strength.. For the C35d12-1 to C35d12-4 (Figure 37a) good agreement is observed and additionally similar trend regarding dynamic pullout rates between Li et al.'s experimental data and the trend observed in this work. Change in the rate between tested dynamic pullout rates, did not result in a monotonic behavior (i.e., increasing pullout rate results in increased bond stress) but rather the observed results were mixed and likely dependent on experimental data spread. Similarly, when investigating the effect of bar diameter between cases C35d12-1; C35d16-1; C35d20-1 (Figure 37b) non monotonic behavior was observed for the residual bond stress at large slip values but overall similar peak bond stress. For the C50d16-1 case as expected both higher peak and residual bond stress was observed due to using higher compressive strength concrete. Overall, the proposed constitutive model was capable of accurately replicating the experimental test results of Li et al, but due to the S-type exponential curve that is utilized for the bond degradation part, experimental result replication accuracy abrupt bond strength reduction after S_0 resulted in higher inaccuracies.

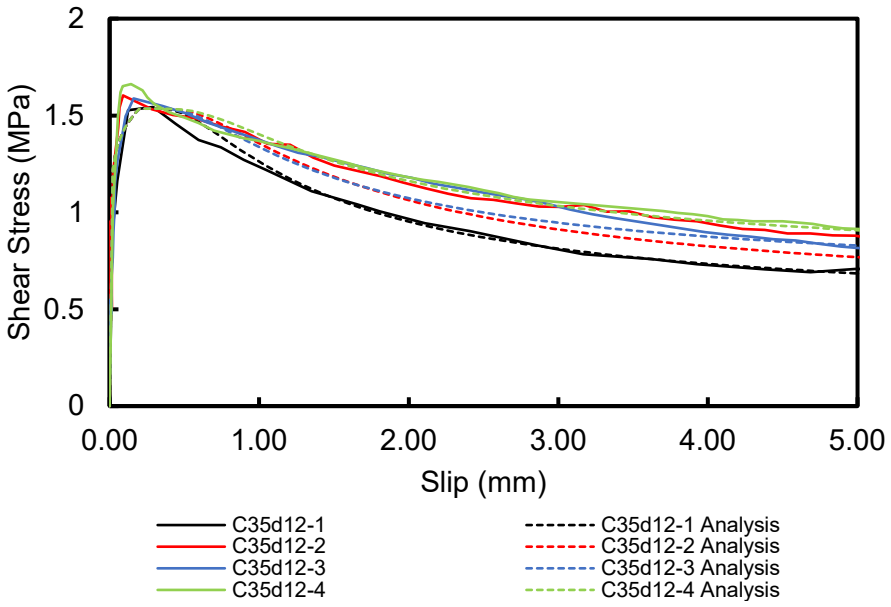

(a)

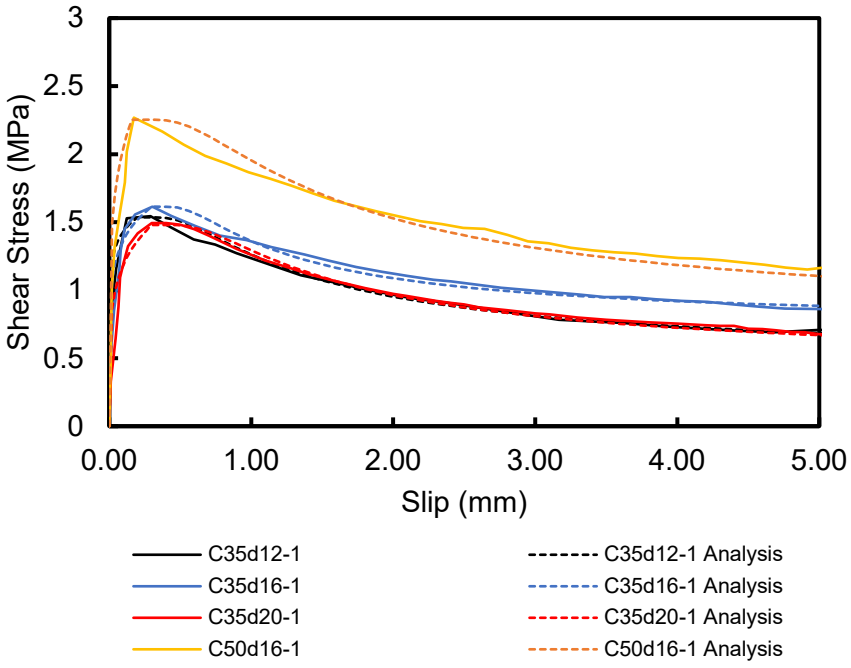

(b)

Figure 37 Comparison between experimental tests data of Table 9 from (Li et al., 2021) with constitutive model results presented in this work for: (a) varying pullout rates (b) varying bar diameter and concrete strength.

4.5. FEM replication of uniaxial pullout

Numerical modeling was used to verify the reproducibility of the experimental results in the commercially available finite element software Abaqus as part of a broader research work aimed at modeling the dynamic fracture behavior of prestressed concrete member. To achieve this goal, it is necessary to accurately simulate the fracture of PC-Tendons as well as the development and loss of bond between tendons and the surrounding grouting mortar. In this work, full-scale three-dimensional models of the tested specimens were created, accurately reproducing their geometrical characteristics and most importantly embedded length. From the experimental analysis results it is clear that not only simple horizontal frictional sliding but also normal directional sticking is occurring at the contact surface. When constructing the model, it is important to consider how to incorporate this effect, depending on the scale of the model.

As a first step towards verifying the accuracy of the proposed constitutive model in FE simulations, a cubical-shaped model consisting of hundred 8-noded C3D8R elements 1x1x1mm in size was modeled being in contact with a thin three-dimensional plate, with appropriate normal forces and boundary conditions applied to model. For this instance, only the Abaqus built-in Coulomb frictional model (ABAQUS Inc., 2005) was applied to investigate interaction and frictional characteristics. Influence of several parameters such as relative material stiffness; boundary condition application methodology; and applied normal forces which in result create a contact pressure at the interface between the two materials. In Figure 38 Effect of relative material stiffness on frictional shear stress under normal load unidirectional displacement-type boundary conditions for planar friction simulation. the effect of relative material stiffness is analyzed. When a uniform displacement-type boundary condition is applied along the height of one of the vertical surfaces of the cubical model, due to the existence of friction at the interface between the two objects, horizontal force and overturning moment will be applied at the interface layer. At lower ratio of relative material stiffness shear stresses at the interface due to friction peak in comparison to middle of the cube. To replicate the analytical results through numerical methods it is essential to introduce a high interface stiffness ratio reduce overturning moments when pure shear friction is of interest. Similar results were observed when modified the displacement-based boundary condition

which is responsible for horizontal displacement. In this simplified case, uniform displacement of nodes along a vertical surface of the cube results in increased frictional shear stressed at the leading and trailing surfaces and the numerical results are reproduced accurately when displacement-based boundary condition is applied at the interface node of the cube. When investigating the results of contact pressure, to avoid artificial overpenetration as a result of the contact algorithm (Dassault, 2012) it is necessary to increase the material stiffness ratio accordingly (material stiffness ratio > 10) to simulate analytical results (Figure 38).

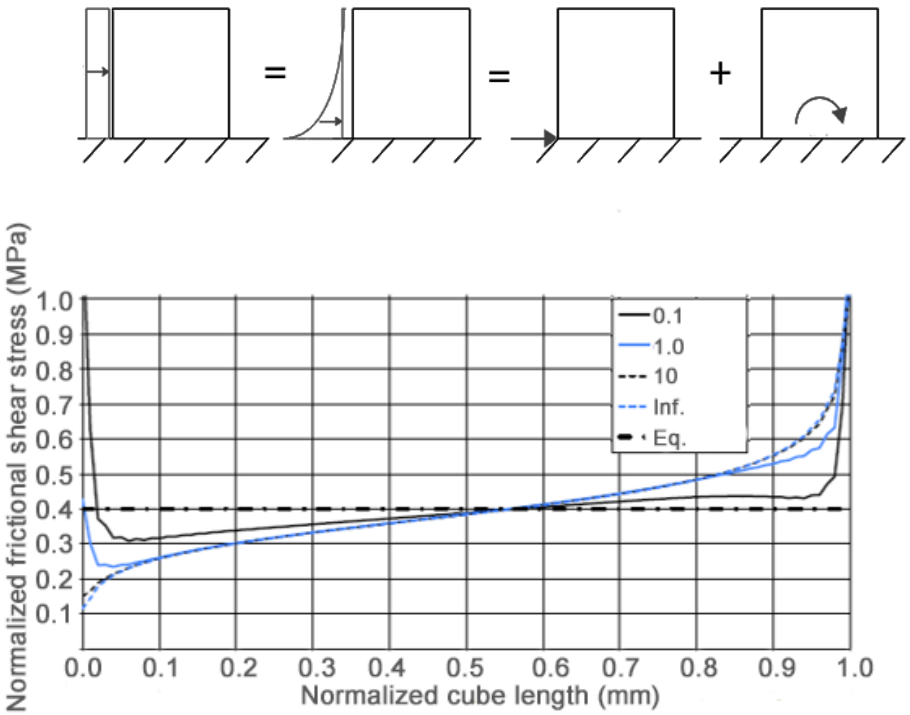

Figure 38 Effect of relative material stiffness on frictional shear stress under normal load unidirectional displacement-type boundary conditions for planar friction simulation.

To numerically simulate the bond development and degradation during pullout experiments apart from model-to-model interaction on a surface level, cohesive characteristics have been modeled though a cohesive zone modelling (CZM) approach. Through this, CZM crack modeling allows for numerical simulation of delamination in general and in this work shear bond degradation with the development and propagation of a damage zone at the interface between bar and grouting mortar. Complex stress and displacement conditions due to geometrical characteristics and material properties as well as mesh-independent modeling, as long as it is adequately refined, can all be simulated though cohesive damage model from both

initiation and propagation perspective (Bažant & Jirásek, 2002; Hutchinson & Suo, 1992; Zhao et al., 2014). Shear stress transfer between bar and grouting mortar does not deteriorate instantaneously at S_0 after which bond damage is initiated but rather it degrades progressively by interfacial stiffness reduction (Davies & Guiamatsia, 2012). Through this modeling approach it is possible to represent bond development and degradation though a zero-thickness CZM approach (cohesive surface interaction (Coelho et al., 2015; Dassault, 2012)) which is formulated by nodes which are coincident located on each of the two sides of the interface layer and can separate when stresses are acting upon them in a tensile or shear manner. Since a zero-thickness approach is used, instead of typical stress-strain model usage for representing deformation, a separation (mode I) or sliding (mode II, III) approach is utilized to quantify deformation of the cohesive surface in terms of traction-separation ($\tau - \delta$) (Saeedifar et al., 2015).

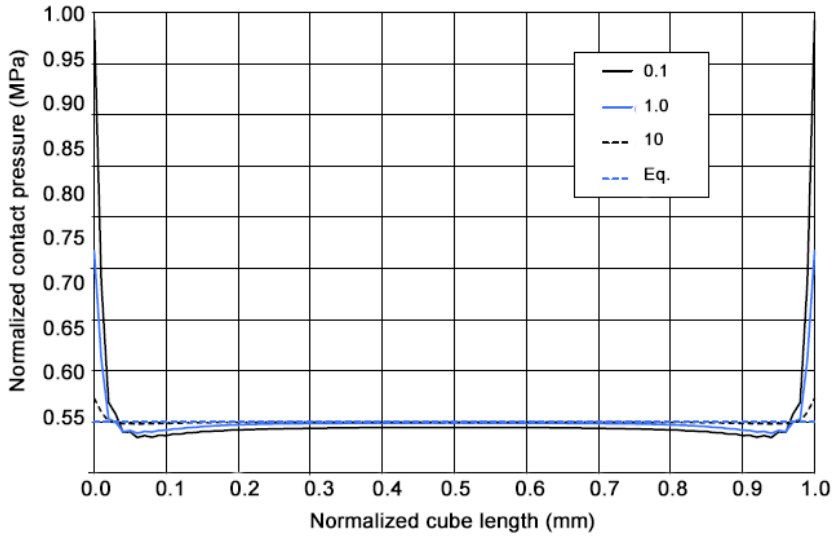

Figure 39 Effect of contact pressure on frictional shear stress under normal load, unidirectional displacement-type boundary conditions for planar friction simulation.

The traction-separation approach used to numerically model the experimental results, utilizes a linear part up to peak traction after which separation (slip) occurs and subsequently the bond degradation part (separation) was calibrated based on data obtained from Equation 27. The coefficient of friction between mortar and smooth bar was chosen as 0.6. According to literature, static coefficient of friction varies between 0.56 – 0.76 depending on the normal force acting on the interface and relative smoothness and manufacturing method of the two

materials (Hieu BUI et al., n.d.; Ikenaga et al., n.d.; Rabbat & Russell, 1985). The elastic uncoupled traction-separation behavior up to peak shear bond stress can be written as:

$$\begin{bmatrix}\sigma_n\\ \tau_s\\ \tau_t\end{bmatrix}=\begin{bmatrix}K_{nn} & 0 & 0\\ 0 & K_{ss} & 0\\ 0 & 0 & K_{tt}\end{bmatrix}\begin{bmatrix}\delta_n\\ \delta_s\\ \delta_t\end{bmatrix} \quad 33$$

where K is the interfacial stiffness $K = {\tau_{lin}}/{d_{lin}}$ and can be calculated by approximating the linear part of the ascending branch of Equation (25); n is the normal direction; s is the direction-1 shear (mode II); and t is the direction-2 shear (mode III). In this work, initiation of bond degradation is defined through a maximum stress criterion according to Equation (33).

$$max\left\{\frac{\langle\sigma_n\rangle}{\sigma_n^0},\frac{\tau_s}{\tau_s^0},\frac{\tau_t}{\tau_t^0}\right\}=1 \quad 34$$

Descending branch modeled with Equation (30) is then used to calibrate the degradation rate of the interface stiffness as defined by the damage evolution law. Bond degradation is characterized by a scalar damage variable D ranging from $0 \leq D \leq 1$. When damage initiation criteria is met, the damage variables changes progressively from zero until it reaches full degradation value according to the defined progression as seen in Figure 40. The damage evolution depending on Damage Variables and Total/Plastic Displacement parameters is defined according to Equation (34).

$$D = 1 - \frac{k}{k_0} \quad 35$$

where k_0 is the initial bond stiffness at the mode of interest; and k is the degraded bond stiffness for different slip values.

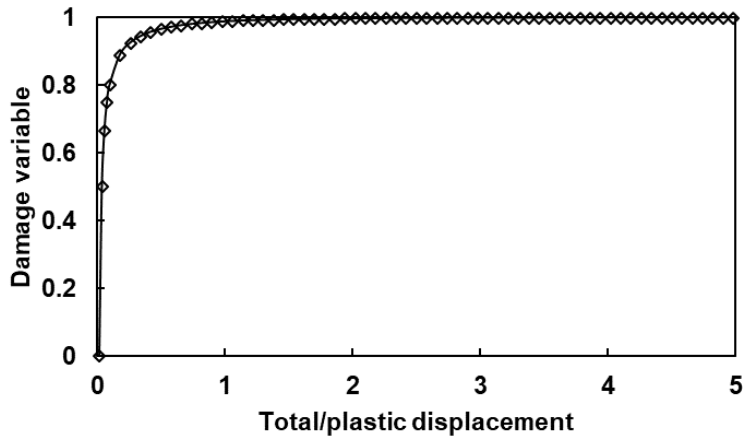

Figure 40 User-defined bond scalar damage variable

To simulate the experimental procedure in a finite element environment, 140x140x140 mm cubical specimens were created. These specimens were modeled with a central opening of suitable size to enable stress-free interaction between smooth bars (represented as cylinders) and the surrounding mortar cube. To prevent element overpenetration stress concentration effects at the interface between the bar and mortar, we employed a fine mesh. The mesh consisted of 64 elements along the perimeter of the bar and the center opening of the grout cube and in total more than 20000 elements were used in this simulation. Additionally, nearby nodes were positioned closely together to avoid stress concentration caused by excessive penetration (Figure 41). Sufficiently fine mesh at the interface is required to accurate estimate the material behavior around peak bond shear stress as well as to ensure smooth degradation at the softening part of a stress-slip graph (Figure 43a). Additionally, to ensure accurate post-peak debonding simulation it is necessary to define the characteristic element length of the grout material at the interface according to Abaqus analysis manual recommendations (Chapter 19.2.3) which states that for continuum elements characteristic element length is equal to element volume divided by largest surface area $l_{c=} = V/A_{MAX}$.

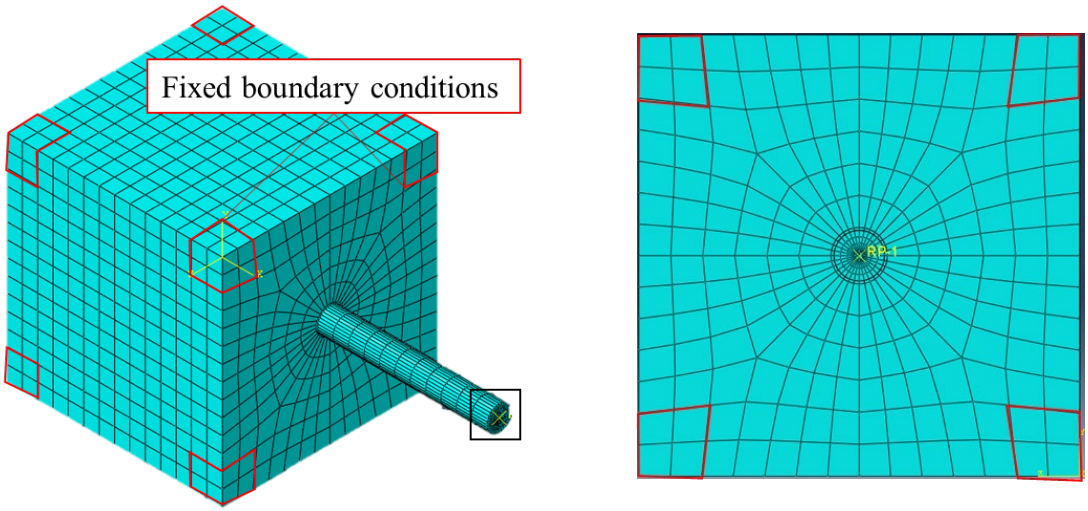

Figure 41 Pullout specimen replication model in ABAQUS: isometric view (left); front view (right).

The free end nodes of the bar were constrained to allow movement only in the pullout direction (x-axis). A displacement-based load application procedure was implemented, following a similar approach to the experimental procedure, with varying pullout rates. Fixed-type boundary conditions were applied at the eight corners of the model cube, as illustrated in Figure 42. To validate the analytical model from the work of Li et al. (Li et al., 2021), simulated

the pullout cases of FEM c35d12-1 and c50d16-1. Figure 42 displays the distribution of axial strain in the smooth bar. The viewing scale in the plane perpendicular to the pullout direction has been magnified by a factor of five thousand to illustrate the cross-sectional deformation of the bar at slip values corresponding to 0.0, 0.3, 1.0, and 7.0mm respectively. Moreover, an increase in axial strain can be observed up to S_0 in the embedded part of the smooth bar. However, minimal axial strain variation is observed in the remaining length of the bar. Even at a slip of 7.0mm, axial strain variation is noticeable in the embedded part, with increasing strain values towards the pullout end of the bar. This confirms the aforementioned cross-section deformation of the bar.

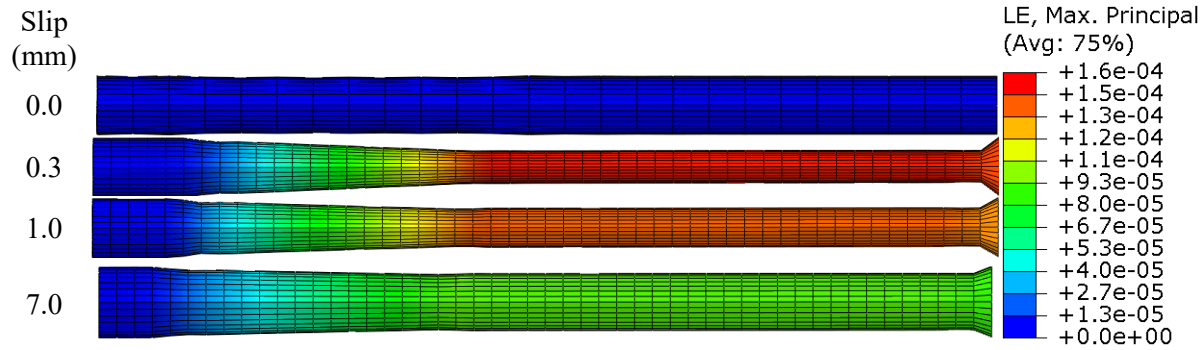

Figure 42 Bar axial strain for 0.0; 0.3; 1.0 and 7.0 mm of slip for c50d16-1 case.

Figure 43a presents a comparison between the FEM and experimental results, showing a good level of accuracy in terms of shear bond stress and slip. Both the c35d12-1 and c50d16-1 cases demonstrate a strong agreement in terms of bond stiffness, peak shear stress, and the remaining shear stress at 5.0mm of slip. Examining the bond stress distribution at different slip values along the bar length (Figure 43b), we observe a 66% reduction in stress value at 0.3mm of slip, which aligns with the cross-sectional deformation observed in Figure 42. As slip values increase, the variation in stress decreases due to bond degradation. However, the side opposite from the pullout end consistently exhibits higher stress values, which can be attributed to the influence of frictional forces at the interface between the two materials.

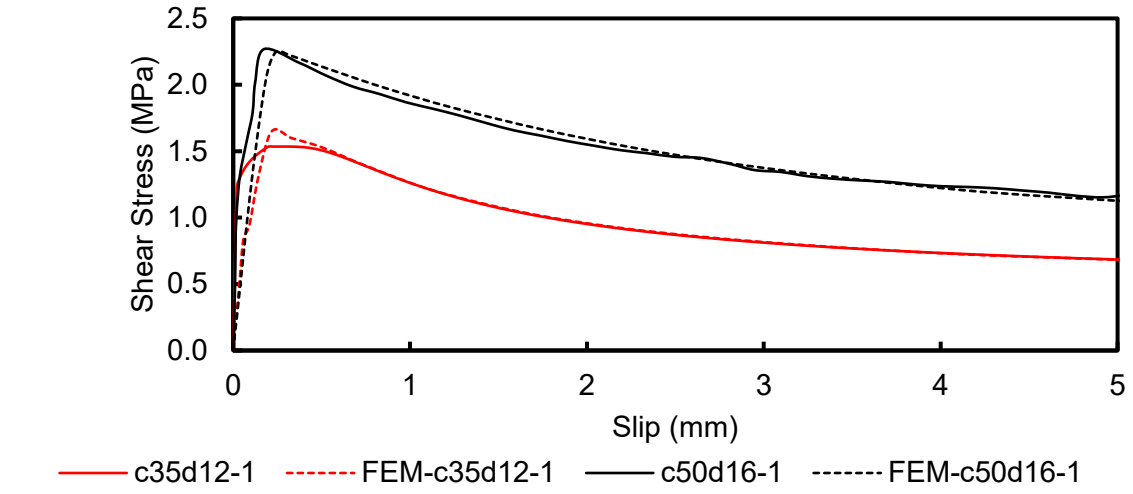

(a)

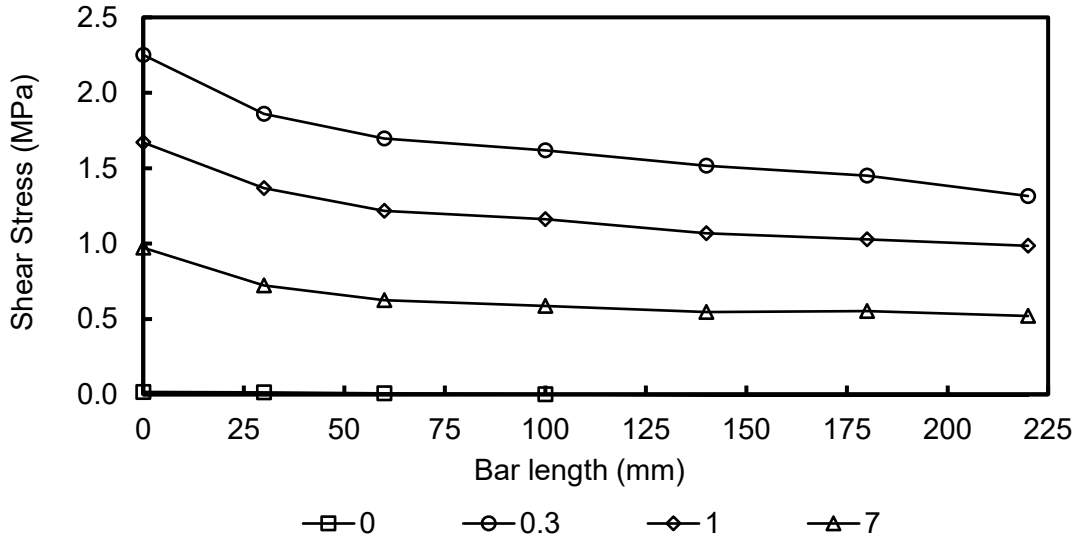

(b)

Figure 43 Numerical simulation results for pullout experiment replication: (a) Comparison between experimental results from Li et al. (2021) and FEM analysis and (b) Shear stress distribution in smooth bar from FEM results for the case of c50d16-1 for pullout slip of 0.0; 0.3; 1.0 and 7.0mm.

Figure 44 illustrates the axial strain distribution in the smooth bar for different pullout slip values. It shows significant variation within the embedded length region, indicating a gradual degradation of the bond. At small slip values, there is a substantial difference in axial strain between the two ends of the embedded region. However, as we compare the axial strain at 1.0 and 7.0mm of slip, the relative difference gradually decreases. This observation suggests a diminishing disparity in axial strain as the slip values increase, indicating a more gradual distribution of strain along the embedded length of the bar.

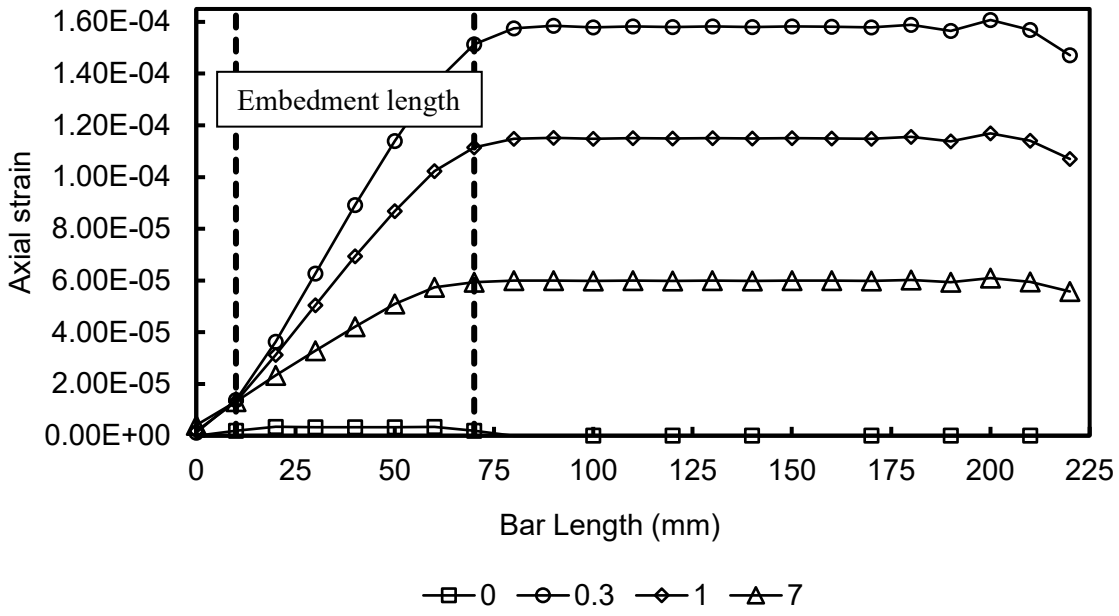

Figure 44 Axial strain distribution for smooth bar embedded in grouting mortar for different slip values.

Chapter 5

Conclusions and Recommendations

5.1. Conclusions

5.1.1. State of the art – Chapter 2

A detailed explanation of the bonding resistance between steel and concrete in reinforced concrete structures is presented. The bonding resistance consists of three components: adhesion, friction, and mechanical anchorage. Adhesion and capillary forces occur due to the hardening of the concrete, but adhesion alone is of minor importance as it fails even at small displacements. Friction, on the other hand, relies on forces in the contact zone and is influenced by external loads, concrete swelling or shrinkage, roughness of the steel surface, and the composition of the concrete. Mechanical anchorage, found in ribbed bars, involves the mechanical interlock between the steel surface and the surrounding concrete, restricting relative displacement. The degree of mechanical anchorage depends on the deformation behavior and shear capacity of the concrete mortar in the bonding joint.

For pre-tensioning bonding, two parameters need to be considered: transferring prestress in the transmission length and anchoring of the tendon tensile force in the flexural bond length. In pre-tensioning, adhesion and friction and Poisson effect or wedge action establish the bond for tendons, while mechanical interlock dominates in strands.

The bond behavior in both the transmission length and flexural bond length affects the anchorage of prestressed tendons in concrete. Anchorage failure, although rare, can result from bending cracks being too close to the end of the element, leading to a loss of equilibrium between the tendon and concrete forces. Design models, such as Eurocode 2; Model Code 2010; ACI 318; AASHTO; Japan road association, provide methods for calculating the bond stress, transmission length, and flexural bond length based on factors like concrete tensile strength, type of tendon, and bond conditions.

5.1.2. Determination of Johnson-Cook Material and Failure Model Constants for High Tensile Strength Tendon Steel in Post-Tensioned Concrete Members - Chapter 3

In Chapter 3, a series of tensile tests were conducted at room temperature with strain rates ranging from 0.001s-1 to 0.5s-1 to determine the Johnson-Cook model and damage parameters for SBPR 930/1080 Type B No. 1 tendon material, focusing on fracture analysis of post-tensioned concrete members. The calculated JC parameters demonstrated good agreement with the experimental data, validating the performance of the damage model. Commercial FEM software was used to verify the agreement between numerical and experimental tensile data. The experimental tests were meticulously replicated to assess the accuracy of the damage model, considering both experimental observations, stress-strain data, and DIC analysis. The JC model proved to be effective in closely predicting the experimental data with minimal effort compared to other analytical models. However, extensive numerical data from various experimental cases are necessary to accurately calibrate the model parameters. Although minor differences between the FE simulation and experimental results were observed, the model exhibited good accuracy in predicting the effects of strain concentration and geometrical deformation, such as necking. Based on the findings of this research, the proposed procedure can be employed to accurately predict the performance of the tested material for fracture analysis of post-tensioned concrete members

5.1.3. Experimental and Numerical Investigation of Bond-Slip Behavior of Round Bars Embedded in Mortar Subjected to Biaxial Lateral Compressive Stresses under Static and Dynamic Pullout Rates - Chapter 4

In Chapter 4, experimental investigation of bond performance and degradation for plain smooth bars being embedded into normal and ultra-high strength grouting mortar was conducted under static; $0.5s^{-1}$ and $1.0s^{-1}$ pullout rates as well as $0.25f_c - 0.5f_c$ lateral compression in order to obtain material parameters to be using in FE modeling as well as propose an analytical bond constitutive model. Overall, the proposed analytical bond model was in good agreement with experimental results and further verification using material data for concrete from other researchers showed good applicability for different material strength, embedded smooth bar diameters and pullout rates. Replication of experimental results in FEM was found to require not only proper material parameters to simulate bond performance but it was also found crucial for accurate simulation to define proper interaction parameters between grouting mortar specimen model as well as the smooth bar. Finally, from the stress and strain

distribution results in the bar it was observed that the proposed model can accurately simulate bond degradation as well as the effects of cross-section bar deformation at different pullout stages and their effects on frictional stress and strain distribution.

By utilizing the proposed bond constitutive model researchers can simulate bond development and degradation of brittle materials such as concrete or grouting mortar when interacting with stiffer material such as steel while accounting for cohesion; friction; confinement stress and debonding rates only utilizing fundamental material parameters and without the need for extensive experimental procedure.

Although the proposed concrete model has been verified for concrete material of typical mixing proportions it is recommended that the findings of this research should be limited to concrete-like materials utilizing natural aggregate as well as adhesives within code recommendations that do not negatively impact the strength or fluidity of concrete. Moreover. it is recommended to keep the concrete strength between the validated range of 35 – 110 MPa of ultimate compressive strength. Furthermore, since the bond model has been calibrated and verified using smooth round bars it is necessary to limit direct application for similarly smooth surfaced round bars and incase of using ribbed bars or strands, effects of mechanical interlocking are expecting to be significant and thus friction and cohesion-related effects might not be clearly visible in any concurring analysis.

5.2. Recommendations

1. To improve the applicability and usability of the proposed Johnson-Cook model in Chapter 3 it is recommended to perform additional tensile tests at higher than room temperature in order to obtain the necessary thermal softening parameters that could be used to model rupture of PC tendons under explosive loading conditions in which thermal load has a significant effect on the overall capacity and behavior of the material.

2. The constitutive shear bond stress-slip model proposed in Chapter 4 follows an analytical approach to calculate bond strength and softening. additional experimental work can be performed in order to propose an analytical calculation methodology for the a, b parameters of Equation (25) and (26).

3. Furthermore, through additional advanced experimental procedure, verification of the proposed bond model can be expanded and applicability limitations can be discovered if strain distribution along with bar axis could be observed visually.

4. Finally, to further confirm and validate the applicability of the proposed analytical bond model, FE analysis combining lateral confinement with dynamic pullout rates is suggested. The combination of the above loading conditions closely simulates the internal stresses experienced in large-scale pretensioned members at large deformation and during failure.

5. From the results obtained in this study, the suggestions presented in Chapter 2.2 cannot be reinforced or discouraged since this study is focusing on material behavior over a small bonded area (limited to 5ϕ). To investigate the effect of grouting material as well as dynamic effects onto the transmission length, there is a need to perform larger scale experiments of beam or slab-type specimens under highly controlled casting and loading conditions to distinguish between different causes and their effects onto bond and transmission length.

6. The proposed bond model in Chapter 4 is applicable for regular, high strength concrete as well as grouting mortar following regularized mixing proportions. In order for the results of this work to be suitable for field applications it is necessary to ensure that proper material pouring, flow and compaction techniques are used so that the paste used in any particular mix will allow for proper contact with the embedded bar without the formation

of air gaps which will decrease the bond strength. It would also be beneficial to perform additional experimental work to investigate the influence of aggregate sizing, as well as water-to-cement ratio have on workability of the mixture and its relationship with bond strength.

References

AASHTO. (2015). Load and Resistance Factor Design for Highway Bridge Superstructures. *Reference Manual*, *18*(3), 74–82.

ABAQUS Inc. (2005). ABAQUS Theory Manual. *ABAQUS Documentation*, 1176.

Abdelatif, A. O., Owen, J. S., & Hussein, M. F. M. (2013). Re-anchorage of a ruptured tendon in bonded post-tensioned concrete beams: Model validation. *Key Engineering Materials*, *569–570*, 302–309. https://doi.org/10.4028/www.scientific.net/KEM.569-570.302

Abrams, D. A. (1913). Tests of bond between concrete and steel. *University of Illinois Bulletin*, *No. 71*, 240.

Akbari, Z., Mirzadeh, H., & Cabrera, J. M. (2015). A simple constitutive model for predicting flow stress of medium carbon microalloyed steel during hot deformation. *Materials & Design*, *77*, 126–131. https://doi.org/10.1016/J.MATDES.2015.04.005

American Concrete Institute ACI. (n.d.). *Building code requirements for structural concrete : (ACI 318-95) ; and commentary (ACI 318R-95)*. Farmington Hills, MI : American Concrete Institute, [1995] ©1995. https://search.library.wisc.edu/catalog/999777001402121

Bai, G., Su, Y., & Liu, H. (2021). Experimental study on the complete stress-strain curve of gangue aggregate concrete. *Journal of Physics: Conference Series*, *1904*(1), 7. https://doi.org/10.1088/1742-6596/1904/1/012004

Bai, Y., & Wierzbicki, T. (2008). A new model of metal plasticity and fracture with pressure and Lode dependence. *International Journal of Plasticity*, *24*(6), 1071–1096. https://doi.org/10.1016/J.IJPLAS.2007.09.004

Baldwin, M. I., & Clark, L. A. (1995). The assessment of reinforcing bars with inadequate anchorage. *Magazine of Concrete Research*, *47*(171), 95–102.

Banerjee, A., Dhar, S., Acharyya, S., Datta, D., & Nayak, N. (2015). Determination of Johnson cook material and failure model constants and numerical modelling of Charpy impact test of armour steel. *Materials Science and Engineering A*, *640*, 200–209. https://doi.org/10.1016/j.msea.2015.05.073

Bao, Y. (2005). Dependence of ductile crack formation in tensile tests on stress triaxiality, stress and strain ratios. *Engineering Fracture Mechanics*, *72*(4), 505–522. https://doi.org/10.1016/J.ENGFRACMECH.2004.04.012

Bao, Y., & Wierzbicki, T. (2004). On fracture locus in the equivalent strain and stress triaxiality space. *International Journal of Mechanical Sciences*, *46*, 81–98. https://doi.org/10.1016/j.ijmecsci.2004.02.006

Bažant, Z. P., & Jirásek, M. (2002). Nonlocal integral formulations of plasticity and damage: survey of progress. *Journal of Engineering Mechanics*, *128*(11), 1119–1149.

Bridgman, P. (1952). *Studies in large plastic flow and fracture with special emphasis on the effects of hydrostatic pressure.* (1st ed.). McGraw-Hill.

Buckner, C. D. (1995). A review of strand development length for pretensioned concrete members. *PCI Journal*, *40*(2), 84–105.

Cairns, J. (2021). Local bond–slip model for plain surface reinforcement. *Structural Concrete*, *22*(2), 666–675. https://doi.org/10.1002/suco.202000114

CEN, E. C. (2004). *EN 1992-1-1 Eurocode 2: Design of concrete structures-Part 1-1: General ruels and rules for buildings. Brussels*. Brussels, Belgium: European Committee for Standardization (CEN).

Coelho, A. M. G., Mottram, J. T., & Harries, K. A. (2015). Finite element guidelines for simulation of fibre-tension dominated failures in composite materials validated by case studies. *Composite Structures*, *126*, 299–313.

Comité Euro-International du Béton. (1993). CEB-FIP Model Code (MC-90). In *Bulletin d'information*. Thomas Telford Ltd.

Coronelli, D., Castel, A., Vu, N. A., & François, R. (2009). Corroded post-tensioned beams with bonded tendons and wire failure. *Engineering Structures*, *31*(8), 1687–1697. https://doi.org/10.1016/j.engstruct.2009.02.043

Cosenza, E., Manfredi, G., & Realfonzo, R. (1997). Behavior and modeling of bond of FRP rebars to concrete. *Journal of Composites for Construction*, *1*(2), 40–51.

Danqing Chen. (1995). *Stress-Strain behavior of high strength concrete cylinders* [New Jersey Institute of Technology]. http://archives.njit.edu/vol01/etd/1990s/1995/njit-etd1995-031/njit-etd1995-031.pdf

Dassault. (2012). ABAQUS User's Manual. *ABAQUS/CAE User's Manual*, *1 and 2*, 1–847.

Dassault Systemes Simulia. (2021a). *Abaqus*.

Dassault Systemes Simulia. (2021b). *Abaqus Analysis User's Manual*.

Davies, G. A. O., & Guiamatsia, I. (2012). The problem of the cohesive zone in numerically simulating delamination/debonding failure modes. *Applied Composite Materials*, *19*, 831–838.

De Larrard, F., Shaller, I., & Fuchs, J. (1993). Effect of the bar diameter on the bond strength of passive reinforcement in high-performance concrete. *Materials Journal*, *90*(4), 333–339.

Den Uijl, J. A. (1992). Background of the CEB-FIP Model Code 90 clauses on anchorage and transverse tensile actions in the anchorage zone of prestressed concrete members. *CEB Bulletin d'Information*, *212*, 72–94.

Du Béton, F. I. (2013). *fib model code for concrete structures 2010*. Wiley-vch Verlag Gmbh.

Edwards, A. D., & Yannopoulos, P. J. (1979). Local bond-stress to slip relationships for hot rolled deformed bars and mild steel plain bars. *Journal Proceedings*, *76*(3), 405–420.

Eligehausen, R., Popov, E. P., & Bertero, V. V. (1982). *Local bond stress-slip relationships of deformed bars under generalized excitations*.

Feldman, L. R., & Bartlett, F. M. (2005). Bond strength variability in pullout specimens with plain reinforcement. *ACI Structural Journal*, *102*(6), 860.

Feldman, L. R., & Bartlett, F. M. (2007). Bond stresses along plain steel reinforcing bars in pullout specimens. *ACI Structural Journal*, *104*(6), 685.

fib Model Code for Concrete Structures 2010. (2013). *Fib Model Code for Concrete Structures 2010*, 1–402. https://doi.org/10.1002/9783433604090

Gkolfinopoulos, I., & Chijiwa, N. (2022). Determination of Johnson-Cook Material and Failure Model Constants for High-Tensile-Strength Tendon Steel in Post-Tensioned Concrete Members. *Applied Sciences*, *12*(15). https://doi.org/10.3390/app12157774

GOM GmbH. (n.d.). *GOM Correlate* (2021). GOM-Precise Industrial 3D Metrology. https://www.gom.com/index.html

GOM GmbH. (2015a). Digital Image Correlation and Strain Computation Basics. In *GOM Testing-Technical Documentataion*.

GOM GmbH. (2015b). Inspection—3D Testing. In *GOM Correlate Professional V8 SR1 Manual Basic*.

Guo, Y. B., Gao, G. F., Jing, L., & Shim, V. P. W. (2017). Response of high-strength concrete to dynamic compressive loading. *International Journal of Impact Engineering*, *108*, 114–135. https://doi.org/10.1016/J.IJIMPENG.2017.04.015

Hanson, N. W., & Kaar, P. H. (1959). Flexural bond tests of pretensioned prestressed beams. *Journal Proceedings*, *55*(1), 783–802.

He, A., Xie, G., Zhang, H., & Wang, X. (2013). A comparative study on Johnson–Cook, modified Johnson–Cook and Arrhenius-type constitutive models to predict the high temperature flow stress in 20CrMo alloy steel. *Materials & Design (1980-2015)*, *52*, 677–685. https://doi.org/10.1016/J.MATDES.2013.06.010

Hieu BUI, Q., Kabeyasawa, T., Kabeyasawa, T., & Hosokawa, Y. (n.d.). *STATIC TEST ON FRICTION COEFFICIENT OF CONCRETE FOUNDATION*.

Hori, T. (2014). *A Fundamental Study on the Breakdown Behavior of Concrete under High Hydraulic Action* [Graduation Thesis (in Japanese)]. Tokyo Institute of Technology.

Hossain, K. M. A. (2008). Bond characteristics of plain and deformed bars in lightweight pumice concrete. *Construction and Building Materials*, *22*(7), 1491–1499.

Hsu, L. S., & Hsu, C. T. T. (1994). Complete stress – strain behaviour of high-strength concrete under compression. *Magazine of Concrete Research*, *46*(169), 301–312. https://doi.org/10.1680/macr.1994.46.169.301

Hutchinson, J. W., & Suo, Z. (1992). Mixed mode cracking in layered ceramics. *Adv Appl Mech*, *29*, 163–191.

Ikenaga, M., Nagae, T., Mccormick, J., Zhang, P., Katsuo, M., & Nakashima, M. (n.d.). *FRICTION COEFFICIENT FOR EXPOSED COLUMN BASE DESIGN*.

Janney, J. R. (1954). Nature of bond in pre-tensioned prestressed concrete. *Journal Proceedings*, *50*(5), 717–736.

Japan Road Association. (1981). Specifications for highway bridges. *Substructures*.

Jeon, C. H., Nguyen, C. D., & Shim, C. S. (2020). Assessment of Mechanical Properties of Corroded Prestressing Strands. *Applied Sciences (Switzerland)*, *10*(12), 4055. https://doi.org/10.3390/APP10124055

Jeon, C. H., & Shim, C. S. (2020). Flexural behavior of post-tensioned concrete beams with multiple internal corroded strands. *Applied Sciences (Switzerland)*, *10*(22), 1–17. https://doi.org/10.3390/app10227994

Johnson, G. R., & Cook, W. H. (1985). Fracture characteristics of three metals subjected to various strains, strain rates, temperatures and pressures. *Engineering Fracture Mechanics*, *21*(1), 31–48. https://doi.org/10.1016/0013-7944(85)90052-9

Khataei, M., Poursina, M., & Kadkhodaei, M. (2010). A study on fracture locus of St12 steel and implementation ductile damage criteria. *AIP Conference Proceedings*, *1252*, 1303–1308. https://doi.org/10.1063/1.3457533

Kurihara, R., Ito, Y., Cai, Q., & Chijiwa, N. (2022). The Influence of Interlock Loss between Rebar and Concrete on Bond Performance of RC Member. *Applied Sciences*, *12*(3), 1079.

Laldji, S., & Young, A. G. (1988). Bond between steel strand and cement grout in ground anchorages. *Magazine of Concrete Research*, *40*(143), 90–98.

Lane, S., & Rekenthaler, J. D. (1998). The ties that bind. *Public Roads*, *61*(5), 27–29.

Le Minh, H., Khatir, S., Abdel Wahab, M., & Cuong-Le, T. (2021). A concrete damage plasticity model for predicting the effects of compressive high-strength concrete under static and dynamic loads. *Journal of Building Engineering*, *44*. https://doi.org/10.1016/J.JOBE.2021.103239

Li, X. R., Wu, Z. M., & Zheng, J. J. (2021). Dynamic bond stress-slip model for smooth bars in concrete under transverse tensile-compressive stresses. *Structural Concrete*, *22*(3), 1633–1651. https://doi.org/10.1002/SUCO.202000579

Logan, D. R. (1997). Acceptance criteria for bond quality of strand for pretensioned prestressed concrete applications. *PCI Journal*, *42*(2).

Maheshwari, A. K. (2013). Prediction of flow stress for hot deformation processing. *Computational Materials Science*, *69*, 350–358. https://doi.org/10.1016/J.COMMATSCI.2012.11.054

Mains, R. M. (1951). Measurement of the distribution of tensile and bond stresses along reinforcing bars. *Journal Proceedings*, *48*(11), 225–252.

Malvar, L. J. (1995). Tensile and bond properties of GFRP reinforcing bars. *Materials Journal*, *92*(3), 276–285.

Malvar, L. J., Cox, J. V, & Cochran, K. B. (2003). Bond between carbon fiber reinforced polymer bars and concrete. I: Experimental study. *Journal of Composites for Construction*, *7*(2), 154–163.

Martin, H., & Noakowski, P. (1981). Verbundverhalten von Betonstählen. Untersuchung auf der Grundlage von Ausziehversuchen. *Deutscher Ausschuß Für Stahlbeton*, *319*.

Marti-Vargas, J. R., Arbeláez, C. A., Serna-Ros, P., Navarro-Gregori, J., & Pallares-Rubio, L. (2007). Analytical model for transfer length prediction of 13 mm prestressing strand. *Structural Engineering and Mechanics: An International Journal*, *26*(2), 211–229.

Mitchell, D., Cook, W. D., Khan, A. A., & Tham, T. (1993). Influence of high strength concrete on transfer and development length of pretensioning strand. *PCI Journal*, *38*(3), 52–66.

Mo, Y. L., & Chan, J. (1996). Bond and slip of plain rebars in concrete. *Journal of Materials in Civil Engineering*, *8*(4), 208–211.

Murugesan, M., & Jung, D. W. (2019). Johnson cook material and failure model parameters estimation of AISI-1045 medium carbon steel for metal forming applications. *Materials*, *12*(4). https://doi.org/10.3390/ma12040609

Murugesan, M., Lee, S., Kim, D., Kang, Y. H., & Kim, N. (2017). A Comparative Study of Ductile Damage Models Approaches for Joint Strength Prediction in Hot Shear Joining Process. *Procedia Engineering*, *207*, 1689–1694. https://doi.org/10.1016/J.PROENG.2017.10.923

Nitsch, A., & Hegger, J. (2001). *Spannbetonfertigteile mit teilweiser Vorspannung aus hochfestem Beton* (Issue RWTH-CONV-118725). Fakultät für Bauingenieurwesen.

Pape, T. M., & Melcher, R. E. (2013). Performance of 45-year-old corroded prestressed concrete beams. *Proceedings of the Institution of Civil Engineers: Structures and Buildings*, *166*(10), 547–559. https://doi.org/10.1680/stbu.11.00016

Qiu, J., & Zhou, M. (2016). Analytical solution for interference fit for multi-layer thick-walled cylinders and the application in crankshaft bearing design. *Applied Sciences*, *6*(6), 167.

Rabbat, B. G., & Russell, H. G. (1985). Friction Coefficient of Steel on Concrete or Grout. *Journal of Structural Engineering*, *111*(3), 505–515. https://doi.org/10.1061/(ASCE)0733-9445(1985)111:3(505)

Rilem, T. C. (1970). Bond test for reinforcing steel: 2. Pull-out test. *Mater. Struct*, *3*(15), 175–178.

Robins, P. J., & Standish, I. G. (1984). The influence of lateral pressure upon anchorage bond. *Magazine of Concrete Research*, *36*(129), 195–202.

Ruhnau, J., & Kupfer, H. (1977). Spaltzug-, Stirnzug-und Schubbewehrung im Eintragungsbereich von Spannbett-Trägern. *Beton-und Stahlbetonbau*, *72*(7), 175–179.

Saeedifar, M., Fotouhi, M., Najafabadi, M. A., & Toudeshky, H. H. (2015). Prediction of delamination growth in laminated composites using acoustic emission and cohesive zone modeling techniques. *Composite Structures*, *124*, 120–127.

Samantaray, D., Mandal, S., & Bhaduri, A. K. (2009). A comparative study on Johnson Cook, modified Zerilli–Armstrong and Arrhenius-type constitutive models to predict elevated temperature flow behaviour in modified 9Cr–1Mo steel. *Computational Materials Science*, *47*(2), 568–576. https://doi.org/10.1016/J.COMMATSCI.2009.09.025

Shah, S. P., Choi, S., & Jansen, D. C. (1994). *STRAIN SOFTENING OF CONCRETE IN COMPRESSION*.

Shahawy, M. A., Issa, M., & Batchelor, B. (1992). Strand transfer lengths in full scale AASHTO prestressed concrete girders. *PCI Journal*, *37*(3), 84–96.

Stroker, M. F., & Sozen, M. A. (1970). Investigation of Prestressed Reinforced Concrete for Highway Bridges. Part V: Bond Characteristics of Prestressing Strand. *University of Illinois Bulletin*, *503*, 116–119.

Tamakoshi, T., Hiraga, K., & Kimura, Y. (2012). A Case Study of Corrosion Damage of PC Steel - Investigation of Grout Unfilling and Steel Corrosion of Myoko Bridge. *Civil Engineering Journal*, *54*(5), 50–51.

Tassios, T. P. (1980). Properties of bond between concrets and steel under load cycles idealizing seismic actions. *Comité Euro-International Du Béton, Bulletin No*, *131*, 67–121.

Taylor, H. P. J., & JL, C. (1976). *Some detailing problems in concrete frame structures*.

Trejo, D., Beth Hueste, M. D., Gardoni, P., Pillai, R. G., Reinschmidt, K., Been Im, S., Kataria, S., Hurlebaus, S., Gamble, M., & Tat Ngo, T. (2009). *EFFECT OF VOIDS IN GROUTED, POST-TENSIONED CONCRETE BRIDGE CONSTRUCTION: VOLUME 1-ELECTROCHEMICAL TESTING AND RELIABILITY ASSESSMENT 5. Report Date 13. Type of Report and Period Covered Unclassified*. https://static.tti.tamu.edu/tti.tamu.edu/documents/0-4588-1-Vol1.pdf

Untrauer, R. E., & Henry, R. L. (1965). Influence of normal pressure on bond strength. *Journal Proceedings*, *62*(5), 577–586.

Vedantam, K., Bajaj, D., Brar, N. S., & Hill, S. (2006). Johnson - Cook strength models for mild and DP 590 steels. *AIP Conference Proceedings*, *845 I*(July 2006), 775–778. https://doi.org/10.1063/1.2263437

Verderame, G. M., De Carlo, G., Ricci, P., & Fabbrocino, G. (2009). Cyclic bond behaviour of plain bars. Part II: Analytical investigation. *Construction and Building Materials*, *23*(12), 3512–3522. https://doi.org/10.1016/j.conbuildmat.2009.07.001

Verderame, G. M., Ricci, P., De Carlo, G., & Manfredi, G. (2009). Cyclic bond behaviour of plain bars. Part I: Experimental investigation. *Construction and Building Materials*, *23*(12), 3499–3511.

Wang, X., & Shi, J. (2013). Validation of Johnson-Cook plasticity and damage model using impact experiment. *International Journal of Impact Engineering*, *60*, 67–75. https://doi.org/10.1016/J.IJIMPENG.2013.04.010

Wu, Z., Zhang, X., Zheng, J., Hu, Y., & Li, Q. (2014). Bond Behavior of Plain Round Bars Embedded in Concrete Subjected to Biaxial Lateral Tensile-Compressive Stresses. *Journal of Structural Engineering*, *140*(4), 1–11. https://doi.org/10.1061/(asce)st.1943-541x.0000872

Wuertemberger, L., & Palazotto, A. N. (2016). Evaluation of Flow and Failure Properties of Treated 4130 Steel. *Journal of Dynamic Behavior of Materials*, *2*(2), 207–222. https://doi.org/10.1007/s40870-016-0059-1

Xiao, J., & Falkner, H. (2007). Bond behaviour between recycled aggregate concrete and steel rebars. *Construction and Building Materials*, *21*(2), 395–401.

Xing, G., Zhou, C., Wu, T., & Liu, B. (2015). Experimental Study on Bond Behavior between Plain Reinforcing Bars and Concrete. *Advances in Materials Science and Engineering*, *2015*. https://doi.org/10.1155/2015/604280

Xu, F., Wu, Z. M., Zheng, J. J., Hu, Y., & Li, Q. Bin. (2014). Bond behavior of plain round bars in concrete under complex lateral pressures. *ACI Structural Journal*, *111*(1), 15–25. https://doi.org/10.14359/51686427

Xu, K., Wong, C., Yan, B., & Zhu, H. (2003). A high strain rate constitutive model for high strength steels. *SAE Technical Papers*, *724*. https://doi.org/10.4271/2003-01-0260

XU, L., ZHU, T., & DING, D. (2001). Experimental Study of Complete Tensile Stress-Strain Curves of High-Strength Concrete and Compact Reinforced Concrete. *Engineering Mechanics*, *18*(5), 36–42. https://doi.org/1000-4750(2001)05-036-08

Zhao, L., Gong, Y., Zhang, J., Chen, Y., & Fei, B. (2014). Simulation of delamination growth in multidirectional laminates under mode I and mixed mode I/II loadings using cohesive elements. *Composite Structures*, *116*, 509–522.

Zia, P., & Mostafa, T. (1977). Development length of prestressing strands. *PCI Journal*, *22*(5), 54–65.

Appendix A

A.1 Johnson-Cook damage parameter calculations

The calculations and parameter estimation carried out in Chapter 3; sections 3 and 4 considered the damage initiation point depicted in Figure 16, along with the subsequent material softening described in Chapter 3 section 4.1 and Figure 21b. By following this procedure, the FEM simulations closely matched the experimental data, both on a singular element basis (Figure 20) and in full model simulations (Figure 23). When using the fracture point as the basis for calculating JC damage parameters, the correlation between fracture strain and stress triaxiality from uniaxial tensile test data is illustrated in Figure A1. The curve, although exponential in shape, exhibits a distinctive pattern due to the D1-D3 parameters. Similarly, when incorporating the newly calculated parameters into Equation (25), the angle of the linear fit equation and the corresponding data points lead to a different D4 parameter, as depicted in Figure 46.

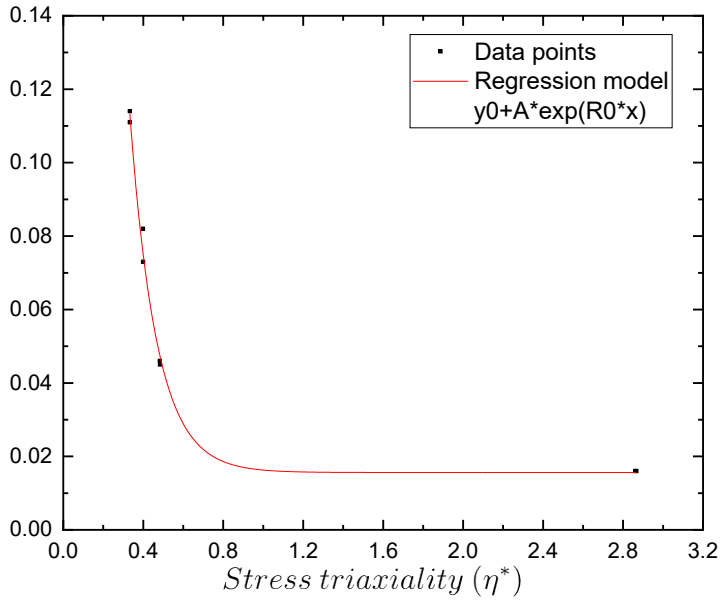

Figure 45 Fracture strain and stress triaxiality relationship from uniaxial tensile test data based on fracture point calculation.

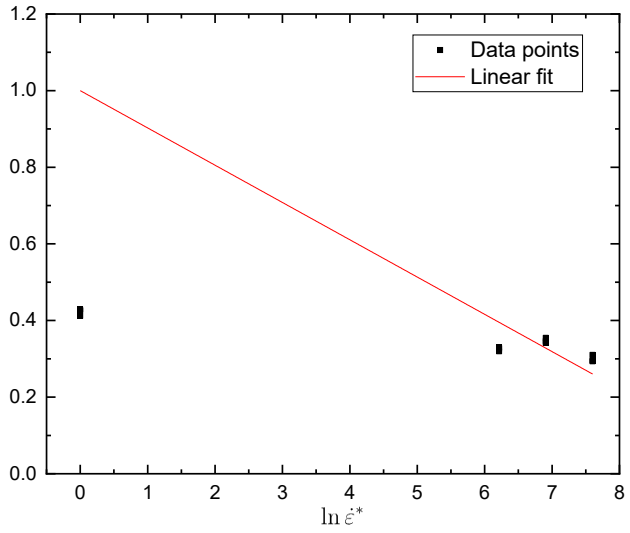

Figure 46 Relationship between $\frac{\varepsilon_f}{D_1 + D_2 \cdot e^{D_3 \eta^*}}$ and $\ln \dot{\varepsilon}^*$ based on fracture point calculation.

The calculated JC damage model parameters for fracture point-based calculation are summarized in Table 10 and similarly to section can be used in FE software to simulate yield and fracture of high strength tendons but with an evident overestimation of their corresponding softening behavior.

Table 10 Johnson-Cook damage model parameters for SBPR 930/1080 Type B No. 1 based on fracture point estimation.

D1	D2	D3	D4	D5
0.0156	1.1733	7.4656	-0.0573	0

With the parameters of Table 10, a comparison similar to Figure 20 can be seen be-tween experimental true stress-strain curves for different strain rates of Table 2 with the results obtain from a singular finite element. It is evident that due to the usage of fracture strain instead of corresponding damage initiation value larger discrepancies are observed between the experimental FE simulation results especially in the case of $0.001s^{-1}$ strain rate case. When performing numerical simulations of full-scale tensile specimens similar to section 4.2, it can be seen that using damage parameters of Table 10 both ultimate stress state and rupture strain are being overestimated in comparison to the experimental results and thus the JC damage parameters of section 3.4.2 are recommended for usage in FE soft-ware applications (Figure 48).

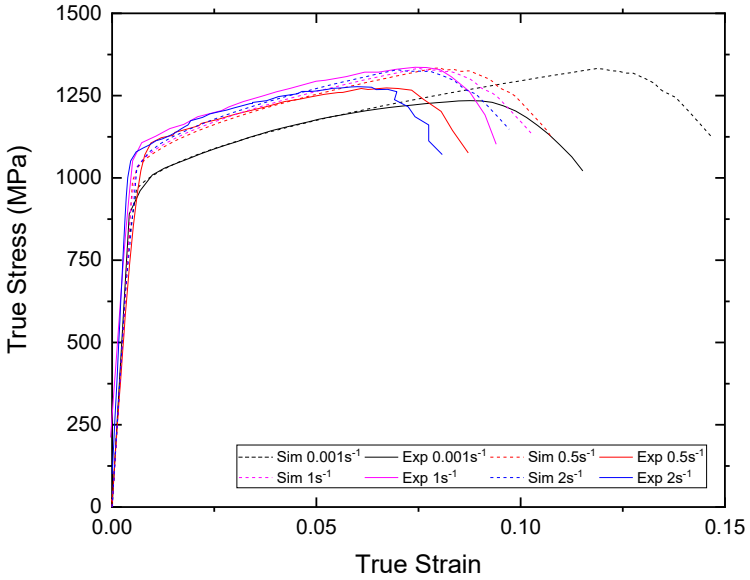

Figure 47 Comparison between experimental (Exp, continuous-lines) and FE simulation (Sim, dotted-lines) results for 0.001s-1 – 2s-1 strain rates using JC damage parameters of Table A1.

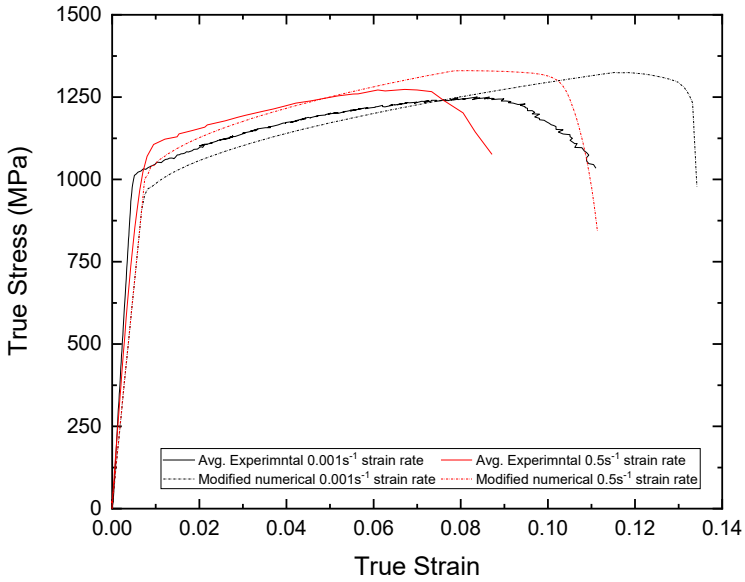

Figure 48 True stress-strain plot comparison for $0.001s^{-1}$ and $0.5s^{-1}$ strain rates for average experimental and numerical simulation using JC damage parameters of Table 10.

A.2 Johnson-Cook C parameter calculation sensitivity analysis

Regarding the calculation procedure for C parameter followed in Figure 15 and Eq. (19), in order to reduce the influence of quasi-static data ($\ln \varepsilon^* = -6.90$) 1/5th of the data was removed and the remaining were plotted again in Figure 49. As it can be seen from the comparison of Figure 15 and Figure 50 the influence of the amount of data used is minimal for the calculation of C parameter since the data accumulation trend remains similar.

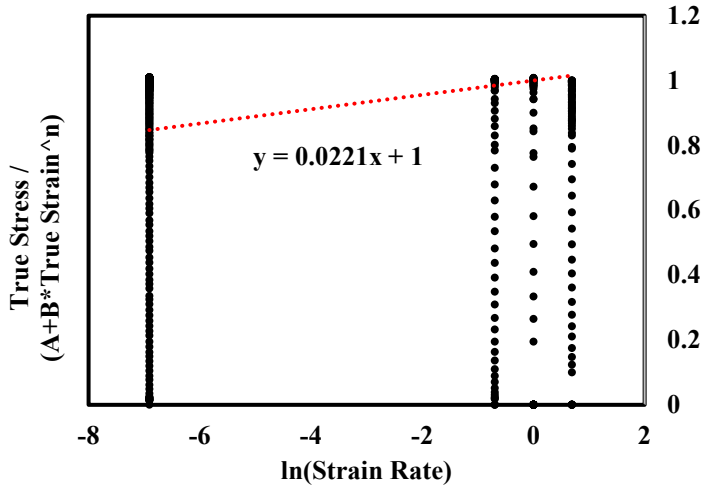

Figure 49 Relationship between $\frac{\sigma}{(A+B\varepsilon^n}$ and $ln\dot{\varepsilon}^*$ for four different strain rates (0.001s^{-1}, 0.5s^{-1}, 1s^{-1}, 2s^{-1}) using original data count.

From the linear regression fitment of the data in both Figure 15 and Figure 49 a C parameter of 0.0221 and 0.241 is calculated respectively.

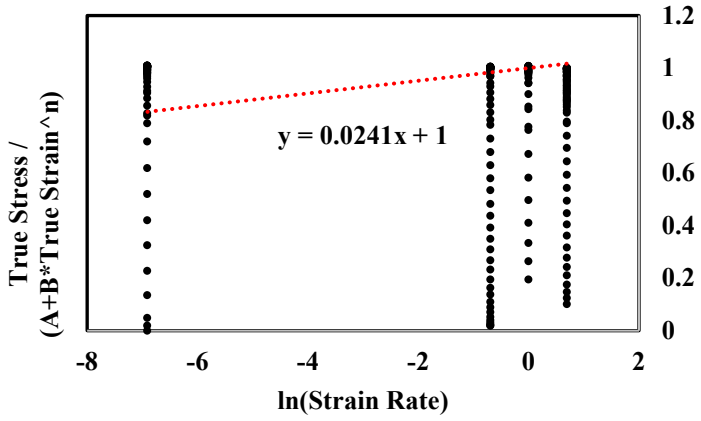

Figure 50 Relationship between $\frac{\sigma}{(A+B\varepsilon^n}$ and $ln\dot{\varepsilon}^*$ for four different strain rates (0.001s^{-1}, 0.5s^{-1}, 1s^{-1}, 2s^{-1}) using reduced data count.

Appendix B

B.1 Mortar specimens compressive and tensile parameter obtaining procedure.

Material properties presented in Table 8 for NS and UHS mortar specimens were obtained through uniaxial compression and split tensile testing procedure using a 100t Amsler testing equipment. To obtain ultimate compression F_{cu} and tension F_t loads load-controlled experimental procedure was performed at rate of 3 kN/sec. For both compression and split-tensile testing specimens were positioned onto metallic alignment plates and no lubrication was used at the interface between the Amsler plates and the specimen. Strain gauges with 60mm gauge length were used to measure strain for all experimental cases. In particular, for the split-tensile testing of cylindrical specimens, the gauges were attached to the middle of the cross section and perpendicular to the loading direction as can be seen in Figure 51. To obtain loading data an appropriate capacity loading cell and data logger were also utilized.

Figure 51 Split-tensile test experimental setup.

In Figure 52 selective experimental test results are presented for NS and UHS respectively for uniaxial compression test results. Overall minimal deviation was recorded for similar

loading cases for the UHS mortar but small deviation was noted for the NS cases. Additionally, in some UHS cases reduced initial stiffness was recorded up to 3000 micro but it is believed to be a result of imperfect bonding between mortar specimen surface and strain gauge. Some deviation was noted for the fracture strain in the case of NS specimens with the most ductile specimen fracturing at approximately 5800 micro.

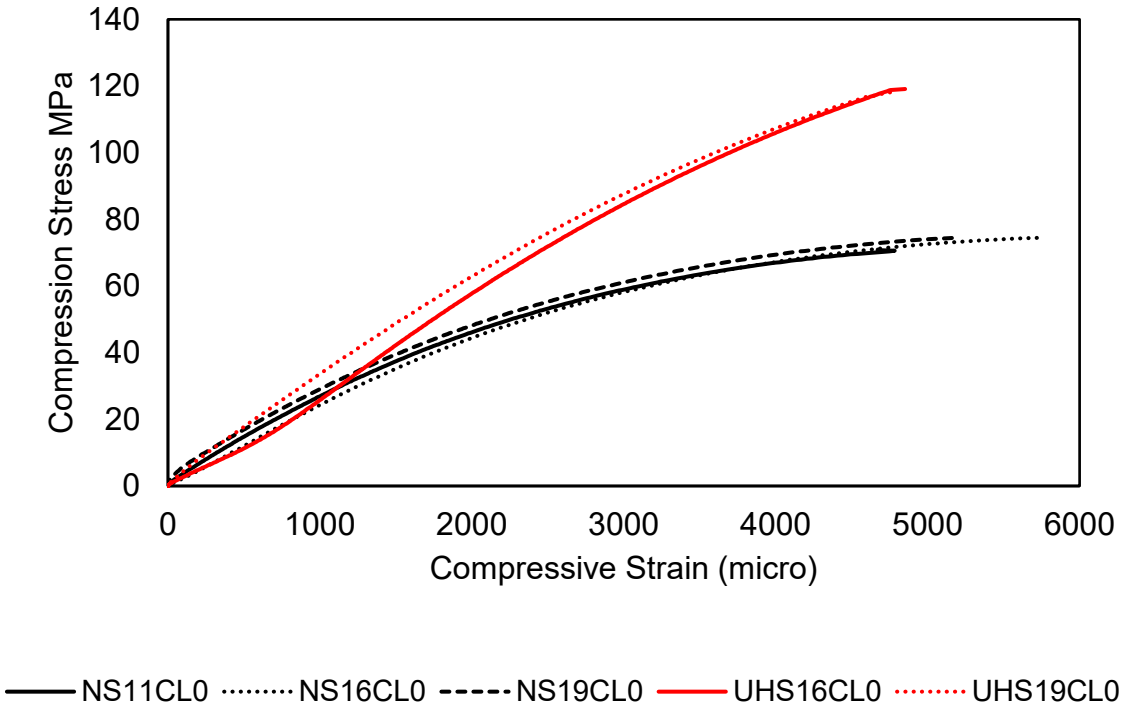

Figure 52 Uniaxial compression test results for NS and UHS mortar.

The results for the split tensile test results presented in Figure 51, show overall good agreement and consistency between repetitive experimental cases. Most significant deviation was recorded for the UHS cases which resulted in uneven stress-strain curve up to the rupture point as can be seen in Figure 53. It is believed that this behavior was to due to micro-deformation occurring at the interface between mortar specimen and metal plate as well as possible micro-rotation of the cylindrical specimen. To convert the force data recorded from the loading cell to tensile stress equation 35 was used (Figure 54)

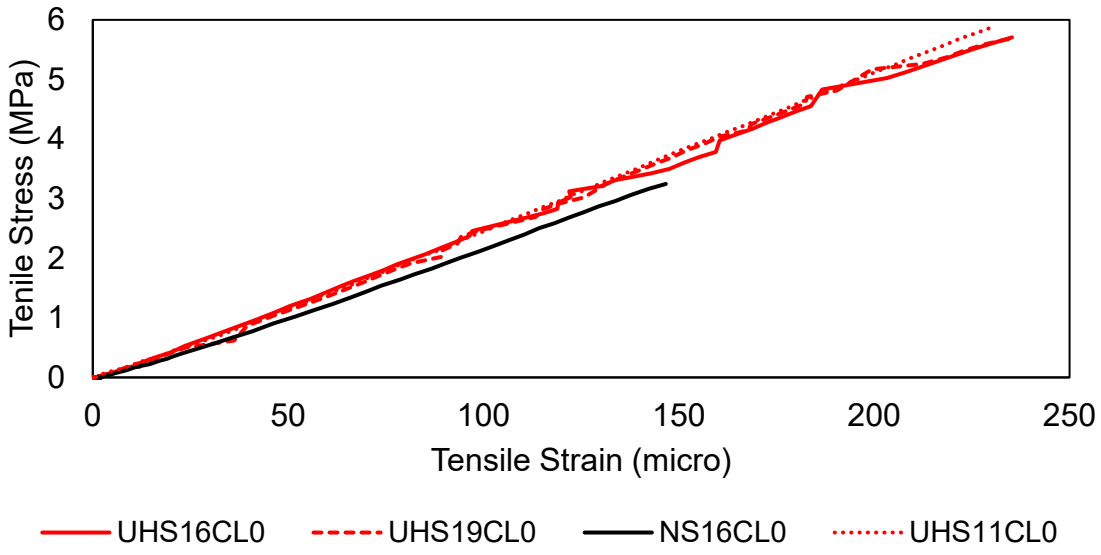

Figure 53 Split-tensile tests results for NS and UHS mortar.

$$f_{ct} = \frac{2P}{\pi DL} \qquad 36$$

where

P Vertical load of testing machine

D Diameter of cylindrical testing specimen

L Length of the cylindrical testing specimen

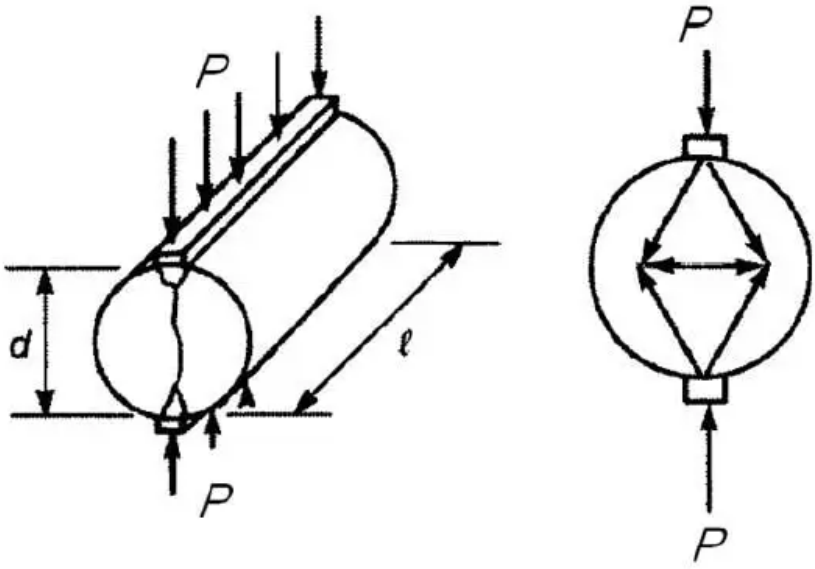

Figure 54 Split-tensile testing procedure according to ASTM C496

B.2 Estimation of softening behavior of concrete and mortar using experimental stress-strain data

Uniaxial compression of concrete specimens following a typical load-controlled experimental procedure results in the specimen fracturing abruptly after reaching its ultimate capacity. To capture the softening behavior of concrete of mortar a displacement-controlled procedure needs to be followed which involves cyclic loading of the specimen resulting in graduation softening until complete degradation.

Hsu et al. (Hsu & Hsu, 1994) performed a series of compression tests on cylindrical specimens and through their experimental results empirical equations are proposed to represent the complete stress strain behavior of confined and unconfined high-concrete (compressive strength exceeding 69 MPa).

$$\eta = \frac{n\beta x}{n\beta - 1 + x^{n\beta}} \quad \text{for} \quad 0 \le x \le x_d \tag{37}$$

where

$\eta = \frac{f_c}{f_c'}$	Normalized stress (ratio of stress to peak stress)
$x = \frac{\epsilon}{\epsilon_0}$	Normalized strain (ratio of strain to strain corresponding to peak stress)
$\beta = \frac{1}{1 - [f_c'/(\epsilon_0 E_{it})]}$	Material parameter correlated to the shape of stress-strain diagram

Le Mihn et al. (Le Minh et al., 2021) proposes three different equations to describe the stress-strain behavior of concrete. The first one estimates the linear behavior of concrete, the second one is nonlinear up to peak compressive stress and the third one estimates the softening behavior of concrete.

$$\sigma_c = f_{cm} + (\sigma_f - f_{cm}) exp\left[\zeta\left(1 - \frac{\varepsilon_f - \varepsilon_{cm}}{\varepsilon - \varepsilon_{cm}}\right)\right] \tag{38}$$

where

σ_f, ε_f	Stress, strain at complete crushing
ζ	Numerical fitting parameter
f_{cm}, ε_{cm}	Peak stress and strain corresponding to peak stress

Both estimation models can produce accurate stress-strain softening if appropriate experimental data are available. Without them accuracy will depend on the proximity of material data with the fitting results obtained through these equations.

In Figure 55 a comparison between a NS grout experimental result along with the stress-strain curves obtained through equations is presented.

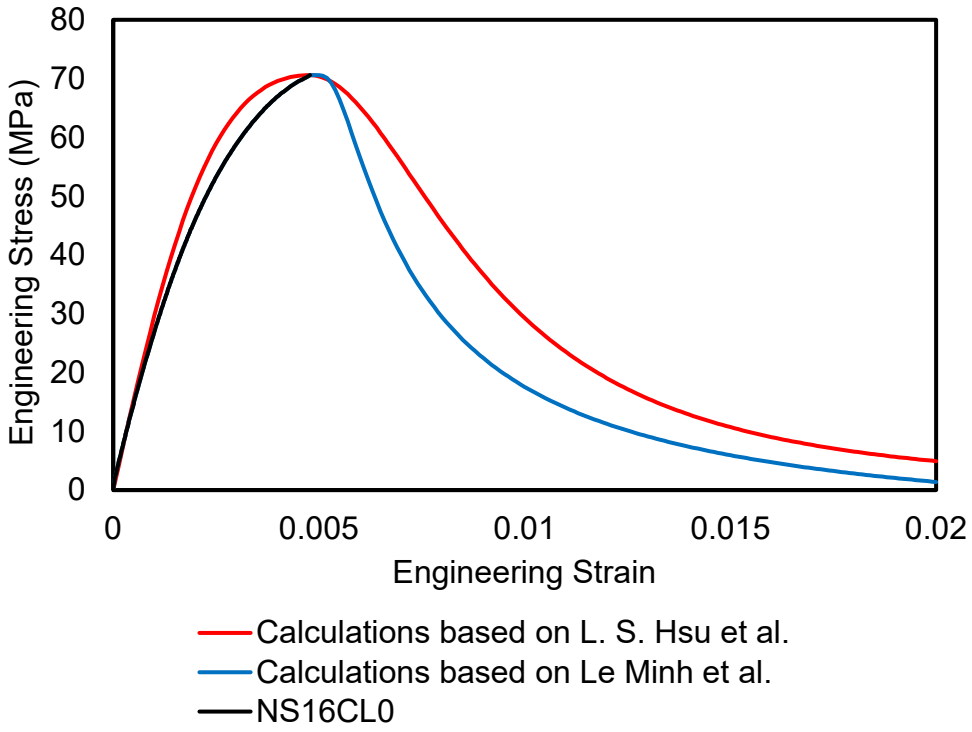

Figure 55 Comparison between concrete softening model of Hsu et al., Le Minh et al. and NS experimental result

To improve on the work of Le Minh et al., Equation 38 as well as ε_f and ζ parameters are modified as follows:

$$\sigma_c = f_{cm} - f_{cm} exp\left[\zeta\left(1 - \frac{\varepsilon_f - \varepsilon_{cm}}{\varepsilon - \varepsilon_{cm}}\right)\right] \quad 39$$

where $\varepsilon_f = 3 * \frac{E_{60}}{E_{80}} \varepsilon_{cm}$ Fracture strain with E_{60}; E_{80} stiffness at $0.6f_{cm}$ and $0.8f_{cm}$ respectively

$$\zeta = \frac{E_{60}}{E_{80}} - 1$$

To verify the accuracy of the proposed equation modification, stress-strain data for various concrete strength mixtures were used from the work of Bai et al., Shah et al., Danqing Chen.,

Guo et al., Xu et al.(G. Bai et al., 2021; Danqing Chen, 1995; Guo et al., 2017; Shah et al., 1994; XU et al., 2001) as seen in Figure 56.

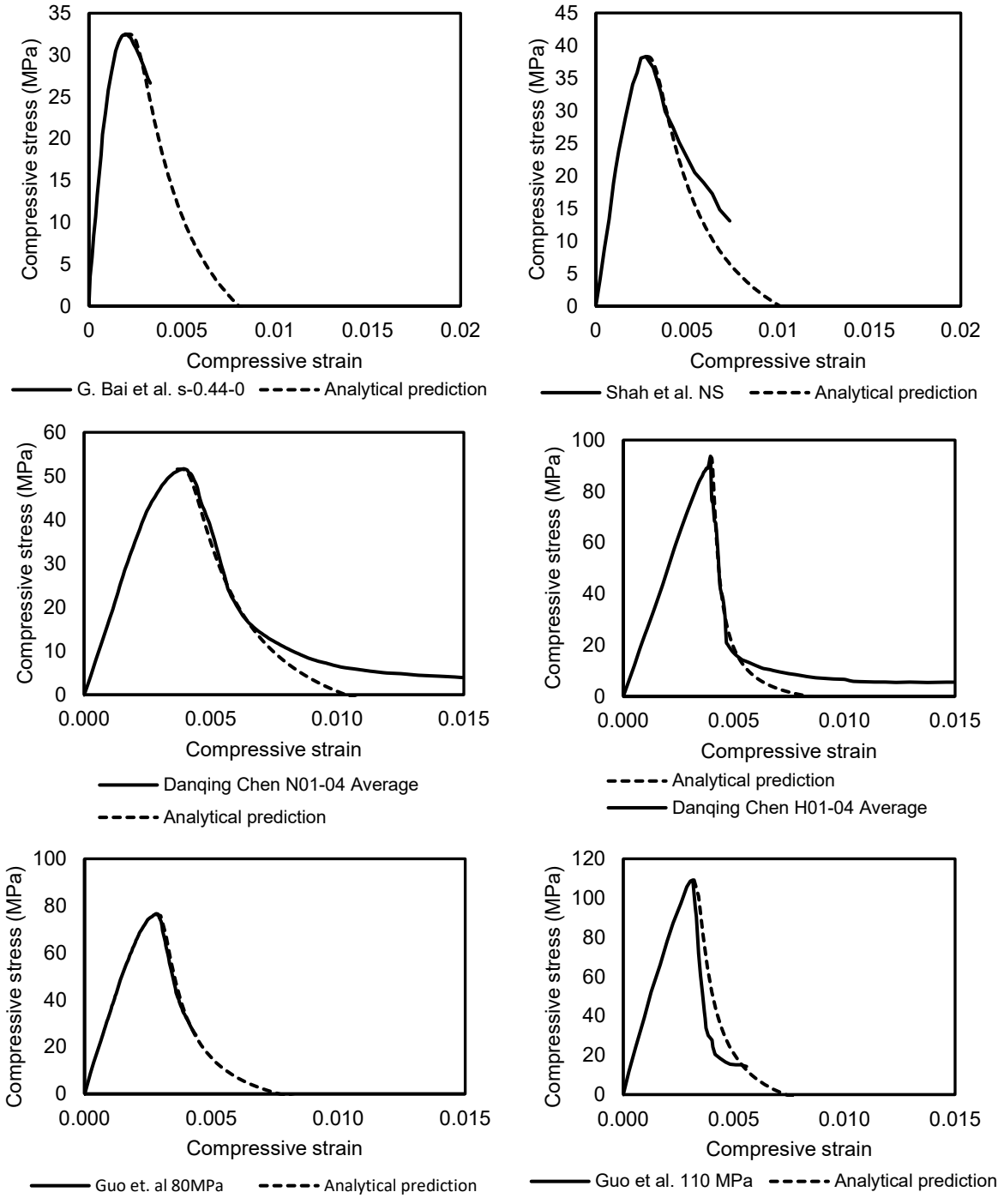

Figure 56 Comparison between experimental stress-strain data from G. Bai et al.; Danqing Chen; Guo et al.; Shah et al. and XU et al. and proposed analytical prediction model of Equation 39.

From the results of Figure 56 it can be seen that the analytical model can closely predict the softening behavior of concrete under uniaxial compression for both low and high strength concrete. A notable deviation occurs at high compressive strain values where the specimens have degraded considerably. Due to the mathematical formulation of the proposed model, it is assumed that at high strain, the specimen will degrade completely in a progressive manner and thus compressive stress values will reach a zero value. This assumption though is not always accurate and its validity is subjected to individual experimental data.

To model the unconfined concrete softening behavior under tensile loading Equation 39 can be also utilized with the modifications listed in Equation 39.

$$\sigma_t = f_t - f_t exp\left[\zeta\left(1 - \frac{\varepsilon_f - \varepsilon_t}{\varepsilon - \varepsilon_t}\right)\right] \quad 40$$

where $\varepsilon_f = 3 * \frac{E_{60}}{E_{80}}\varepsilon_t$ Fracture strain with E_{60}; E_{80} stiffness at $0.6f_t$ and $0.8f_t$ respectively

$$\zeta = \frac{E_{60}}{E_{80}} - 1$$

In principle, Equations 38 and 39 operate in a similar manner. The difference is a direct result of the individual parameters that are utilized. In particular, to calculate the softening behavior of concrete under tensile stress σ_t, maximum tensile stress f_t as well as strain at maximum tensile stress ε_t and strain at tensile failure ε_f are required. Comparing the results of the analytical prediction model with tensile test experimental results from the work of Xu et al. (XU et al., 2001) for concrete with nominal capacity of 50 and 80 MPa in Figure 56, good accuracy is observed.

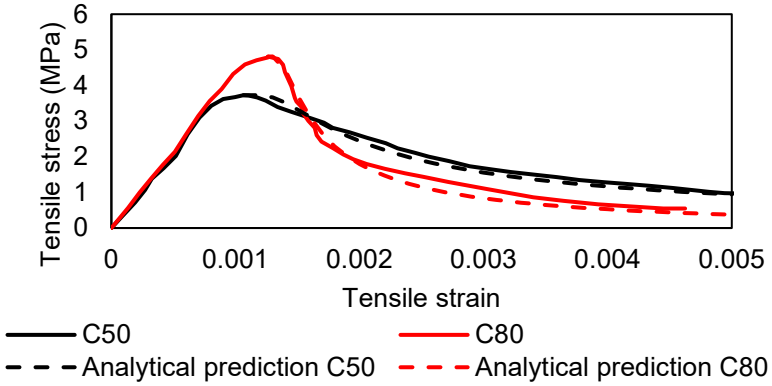

Figure 57 Comparison between experimental stress-strain data from XU et al. and proposed analytical prediction model of Equation 39.